

**FLUIDIC ACTUATORS  
FOR HIGH SPEED FLOW CONTROL**

A Dissertation  
Presented to  
The Academic Faculty

by

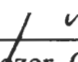
Thomas M. Crittenden

In Partial Fulfillment  
Of the Requirements for the Degree  
Doctor of Philosophy in Mechanical Engineering

Georgia Institute of Technology  
April 2003

**FLUIDIC ACTUATORS  
FOR HIGH SPEED FLOW CONTROL**


Approved: 

  
\_\_\_\_\_  
Ari Glezer, Chair

  
\_\_\_\_\_  
Prateen Desai

\_\_\_\_\_  
Marc Smith

  
\_\_\_\_\_  
Jeff Jagoda

  
\_\_\_\_\_  
Mark Allen

\_\_\_\_\_  
David Parekh

Date Approved May 7, 2003

## ACKNOWLEDGMENTS

I would like to thank my adviser, Ari Glezer, for his guidance and assistance over the course of this work. Both professionally and personally, it has been a learning experience far beyond what I would have expected and his contributions on both counts have been invaluable. I also thank the other members of my committee (David Parekh, Jeff Jagoda, Mark Allen, Prateen Desai, and Marc Smith) for their inputs during the research and comments on this document. Numerous staff members of both Georgia Tech and GTRI have been of great assistance over the years; in particular, I thank Rob Funk for his help with the design and testing of applications of the combustion actuator including the separation control experiments presented herein. Also, the generous funding support of DARPA/AFOSR made this work possible.

My many friends and colleagues in the Fluid Mechanics laboratories (past and present) have all been a blessing and have each contributed in some way to the work presented here. Among these, special thanks go to Bart Smith, Andrew Honohan, Chris Rinehart, and Jason Brown who have each made profound contributions towards making my time here enjoyable.

And I am eternally grateful to my parents for the love and support which they have always provided.

## TABLE OF CONTENTS

APPROVAL PAGE	i
ACKNOWLEDGMENT	ii
LIST OF FIGURES	v
LIST OF TABLES	xi
LIST OF SYMBOLS	xii
SUMMARY	xv
CHAPTER	
I.    Introduction	
I.1    Overview	1
I.2    Synthetic Jets	6
I.3    Small-Scale Combustion	9
II.   Compressible Synthetic Jets	
II.1   Experimental Set-Up and Measurements	12
II.2   Cylinder Pressure	14
II.3   Jet Structure	23
II.4   Numerical Simulation and Results	29
II.5   Duty Cycle Modification Experiment	38
III.  Combustion-Driven Jet Actuators	
III.1  Overview	41
III.2  Experimental Set-Up and Measurements	46
III.3  Parametric Study Results	
III.3.a    Fuel Type and Mixture Ratio	50
III.3.b    Orifice Diameter	56
III.3.c    Chamber Aspect Ratio	61
III.3.d    Chamber Volume	67
III.3.e    Mixture Flow Rate	70
III.3.f    Combustion Frequency	81
III.3.g    Ignition Energy	85



IV.	Low Speed Separation Control with Combustion-Driven Jet Actuators	
IV.1	Experimental Set-Up and Measurements	89
IV.2	Results	93
V.	Conclusions	97
V.1	Compressible Synthetic Jets	98
V.2	Combustion-Driven Jet Actuators	102
APPENDIX: Orifice Geometry Effects		109
FIGURES		114
REFERENCES		170

## LIST OF FIGURES

Figure 1	Conceptual drawing of synthetic jet. (Courtesy of Smith and Glezer, 1998.).	114
Figure 2	Conceptual drawing of combustion-driven jet actuator.	114
Figure 3	Schematic illustration of piston/cylinder actuator.	115
Figure 4	Piston position and velocity over cycle (a) and phase-averaged cylinder pressures for $r = 27.1$ and $L_0/d = 76$ (b), 258 (c), and 2065 (d) for $f = 25$ (●), 50 (□), 75 (◆), 100 (Δ), 125 (▼), 150 (○), 175 (■), and 200 (◇) Hz.	116
Figure 5	Phase-averaged cylinder pressures over cycle in polar coordinates for $r = 27.1$ and $L_0/d = 612$ for $f = 25$ (a), 100 (b), and 200 Hz (c) with reference circle at $P_r = 1.0$ and suction cycle shaded.	117
Figure 6	Maximum (a) and minimum (b) pressures over cycle varying $f$ for $r = 27.1$ and $L_0/d = 2065$ (●), 612 (□), 258 (◆), 132 (Δ), and 76 (▼).	118
Figure 7	Maximum (a) and minimum (b) pressures over cycle varying $f$ (normalized as $St_{L_0}$ ) for $r = 27.1$ and $L_0/d = 2065$ (●), 612 (□), 258 (◆), 132 (Δ), and 76 (▼).	119
Figure 8	Phase-averaged cylinder pressures over cycle for $St_{L_0} = 0.1$ (a), 0.2 (b), and 0.48 (c) for $r = 27.1$ and $L_0/d = 2065$ (●), 612 (□), 258 (◆), 132 (Δ), and 76 (▼).	120
Figure 9	Phase-averaged cylinder pressures over cycle for $f = 100$ Hz and $L_0/d = 76$ (a), 258 (b) and 2065 (c) for $r = 27.1$ (●), 14.6 (□), 6.7 (◆), and 3.2 (Δ).	121
Figure 10	Phase-averaged cylinder pressures over cycle for $r = 3.2$ and $L_0/d = 76$ (a), 258 (b), and 2065 (c) for $f = 25$ (●), 50 (□), 75 (◆), 100 (Δ), 125 (▼), 150 (○), 175 (■), and 200 (◇) Hz.	122
Figure 11	Maximum (a) and minimum (b) pressures over the cycle varying $f$ (normalized as $St_{L_0}$ ) for $L_0/d = 2065$ (●), 612 (□), 258 (◆), 132 (Δ), and 76 (▼), and $r = 27.1$ (black), 14.6 (dark gray), 6.7 (light gray), and 3.2 (open).	123

Figure 12	Schlieren images from conventional synthetic jet (a - driven by piezoelectric membrane, $f \approx 1$ kHz), and compressible synthetic jet (b - $L_0/d = 612$ , $r = 27.1$ , $f = 120$ Hz). (Image a) courtesy of Smith and Glezer, 1998.)	124
Figure 13	Cylinder pressure over cycle and phase-locked Schlieren images of blowing jet for $r = 27.1$ , $L_0/d = 612$ , and $f = 120$ Hz for $t/\tau = 0.18$ (a), $0.28$ (b), $0.34$ (c), $0.40$ (d), $0.46$ (e), $0.50$ (f), and $0.54$ (g).	125
Figure 14	Cylinder pressure over cycle with PIV velocity vectors and vorticity contours for initial blowing for $r = 27.1$ , $L_0/d = 258$ , and $f = 100$ Hz at $t/\tau = 0.12$ (a), $0.14$ (b), $0.16$ (c), and $0.18$ (d).	126
Figure 15	PIV streamwise velocity contours and centerline velocity data for $r = 27.1$ , $L_0/d = 612$ , and $f = 100$ Hz at $t/\tau = 0.30$ (a), $0.34$ (b), $0.38$ (c), $0.42$ (d), $0.46$ (e), and $0.50$ (f).	127
Figure 16	Cylinder pressure over cycle with sample PIV velocity vector fields over suction phase for $r = 27.1$ , $L_0/d = 612$ , and $f = 100$ Hz at $t/\tau = 0.52$ (a), $0.56$ (b), $0.76$ (c), and $0.96$ (d).	128
Figure 17	Simulation results for cylinder pressure (a), temperature (b), mass (c), and mass flux through orifice (d) for $r = 27.1$ and $L_0/d = 258$ for $f = 25$ (●), $50$ (□), $75$ (◆), $100$ (Δ), $125$ (▼), $150$ (○), $175$ (■), and $200$ (◇) Hz.	129
Figure 18	Experimental phase-averaged cylinder pressures (●) compared to numerical simulation pressure (□) over cycle for $f = 100$ Hz and $r = 27.1$ (a) and $6.7$ (b) with $L_0/d = 2065$ (solid line) and $258$ (dashed line).	130
Figure 19	Simulation results for cylinder pressure (a), temperature (b), mass (c), and mass flux through orifice (d) for $r = 27.1$ and $St_{Lo} = 0.25$ for $L_0/d = 76$ (●), $132$ (□), $256$ (v), $612$ (Δ), and $2065$ (▼).	131
Figure 20	Maximum (a) and minimum (b) pressures over cycle varying $f$ (renormalized as $St_{Lo}$ ) for $L_0/d = 2065$ (●), $612$ (□), $258$ (◆), $132$ (Δ), and $76$ (▼), and $r = 27.1$ (black), $14.6$ (dark gray), $6.7$ (light gray), and $3.2$ (open), with lines denoting simulation results.	132
Figure 21	Maximum (a) and minimum (b) pressures over cycle from simulation varying $f$ (normalized as $St_{Lo}$ ) for $r = 27.1$ (●), $14.6$ (□), $6.7$ (◆), and $3.2$ (Δ) (with $r^{1/2}$ and $r^{-1/2}$ denoted with dashed lines in (a) and (b), respectively).	133

Figure 22	Phase-averaged cylinder pressures for $L_0/d = 2065$ and $f = 200$ Hz (●) with isentropic closed system pressure (dashed) over cycle for $r = 27.1$ (a), 14.6 (b), 6.7 (c), and 3.2 (d).	134
Figure 23	Simulation results for mass displacement over cycle varying $f$ (normalized as $St_{L_0}$ ) for $r = 27.1$ (●), 14.6 (□), 6.7 (◆), and 3.2 (Δ).	135
Figure 24	Phase-averaged cylinder pressure over cycle for $r = 27.1$ , $L_0/d = 612$ , and $f = 100$ Hz for unvalved (●) and valved (□) cylinder head in rectangular coordinates (a) and polar coordinates (b and c) with suction cycle shaded.	136
Figure 25	Conceptual pressure-time history for combustion-driven jet actuator.	137
Figure 26	Phase-averaged combustor pressure and a sequence of phase-locked Schlieren images of the exhaust jet ( $V = 1$ cc, $H/D = 1.27$ , hydrogen-air ( $\Phi = 1.0$ ), $d = 1.30$ mm, $Q = 50$ cc/s, and $f = 30$ Hz).	138
Figure 27	Schematic diagram of parametric test chamber for combustion actuator. Baseline values are denoted in parentheses.	139
Figure 28	Phase-averaged combustor pressure for $d = 1.30$ mm for hydrogen (a) and propane (b) with $\Phi = 1.0$ (●), 0.9 (□), 0.8 (◆), 0.7 (Δ), 0.6 (▼), 0.5 (○), and 0.4 (■).	140
Figure 29	Phase-averaged combustor pressures for hydrogen with $\Phi = 1.0$ (a) and 0.5 (b) for $d = 0.79$ (●), 0.89 (□), 1.09 (◆), 1.30 (Δ), 1.50 (▼), 1.63 (○), 1.78 (■), 1.98 (◇), 2.21 (▲), and 2.50 (▽) mm.	141
Figure 30	Surface plots of variation of the phase-averaged peak pressure with $\Phi$ and $d$ for hydrogen (a) and propane (b).	142
Figure 31	Variation of the phase-averaged peak pressures with $\Phi$ for hydrogen for $d = 0.79$ (●), 0.89 (□), 1.09 (◆), 1.30 (Δ), 1.50 (▼), 1.63 (○), 1.78 (■), 1.98 (◇), 2.21 (▲), and 2.50 (▽) mm. The solid line is the idealized constant volume pressure.	143
Figure 32	Comparison of the phase-averaged measured (solid line) and computed (from pressure values - dashed line) thrust with $d = 1.30$ mm for hydrogen with $\Phi = 0.6$ (●) and propane with $\Phi = 1.0$ (□).	143
Figure 33	Surface plots of variation of the calculated peak thrust with $\Phi$ and $d$ for hydrogen (a) and propane (b).	144

Figure 34	Phase averaged-combustor pressure for hydrogen with $d = 1.30$ mm for $H/D = 0.45$ (a), 1.27 (b), and 3.59 (c) for $\Phi = 1.0$ (●), 0.9 (□), 0.8 (◆), 0.7 (Δ), 0.6 (▼), and 0.5 (○).	145
Figure 35	Phase-averaged combustor pressure for hydrogen with $d=1.30$ mm and $\Phi = 1.0$ (a) and 0.7 (b) for $H/D = 0.45$ (●), 0.82 (□), 1.27 (◆), 2.33 (Δ), and 3.59 (▼).	146
Figure 36	Phase-averaged combustor pressure for hydrogen with $d = 1.30$ mm, $f_{ideal} = 10$ Hz, and $\Phi = 1.0$ (a) and 0.7 (b) for $V = 0.25$ (●), 0.50 (□), 1.00 (◆), 1.50 (Δ), and 2.00 (▼) cc.	147
Figure 37	Variation of the phase-averaged peak pressures with $\Phi$ for hydrogen with $d = 1.30$ mm for $V = 0.25$ (●), 0.50 (□), 1.00 (◆), 1.50 (Δ), and 2.00 (▼) cc. The solid line is the idealized constant volume pressure.	148
Figure 38	Phase-averaged combustor pressure for $d = 1.30$ mm for hydrogen with $\Phi = 0.6$ (a) and propane with $\Phi = 1.0$ (b) for $Q = 10$ (●), 30 (□), 50 (◆), 75 (Δ), and 100 (▼) cc/s.	149
Figure 39	Sample flame photography images for stoichiometric propane-air mixture with $d = 1.30$ mm and $Q = 10$ cc/s for 0.5 (a), 1.0 (b), 1.5 (c), 2.0 (d), 2.5 (e), 3.0 (f), 3.5 (g), 4.0 (h), 4.5 (i), 5.0 (j), 5.5 (k), and 6.0 (l) ms after ignition.	150
Figure 40	Sample flame photography images for stoichiometric propane-air mixture with $d = 1.30$ mm and $Q = 30$ cc/s for 0.25 (a), 0.5 (b), 0.75 (c), 1.0 (d), 1.5 (e), 2.0 (f), 2.5 (g), 3.0 (h), 3.5 (i), 4.0 (j), and 4.5 (k) ms after ignition.	151
Figure 41	Sample flame photography images for stoichiometric propane-air mixture with $d = 1.30$ mm and $Q = 50$ cc/s for 0.25 (a), 0.5 (b), 0.75 (c), 1.0 (d), 1.5 (e), 2.0 (f), 2.5 (g), 3.0 (h), 3.5 (i), and 4.0 (j) ms after ignition.	152
Figure 42	Sample flame photography images for stoichiometric propane-air mixture with $d = 1.30$ mm and $Q = 75$ cc/s for 0.25 (a), 0.5 (b), 0.75 (c), 1.0 (d), 1.5 (e), 2.0 (f), 2.5 (g), 3.0 (h), 3.5 (i) ms after ignition.	153
Figure 43	Phase-averaged combustor pressure for $d = 1.09$ mm for hydrogen with $\Phi = 1.0$ (●), 0.9 (□), 0.8 (◆), 0.7 (Δ), 0.6 (▼), 0.5 (○), and 0.4 (■) for $Q = 10$ (a), 30 (b), 50 (c), 75 (d), and 100 (e) cc/s.	154

Figure 44	Contour plots of peak combustor pressure varying $\Phi$ and $d$ for hydrogen with $Q = 10$ (a), 30 (b), 50 (c), 75 (d), and 100 (e) cc/s (data points represented by ■).	155
Figure 45	Contour plots of peak combustor pressure varying $\Phi$ and $d$ for propane with $Q = 10$ (a), 30 (b), 50 (c), and 75 (d) cc/s (data points represented by ■).	156
Figure 46	Phase averaged-combustor pressure for hydrogen with $d = 1.30$ mm for $\Phi = 1.0$ and $Q = 10$ cc/s (a), $\Phi = 0.8$ and $Q = 30$ cc/s (b), and $\Phi = 0.5$ and $Q = 100$ cc/s (c) for $f/f_{ideal} = 0.1$ (●), 0.4 (□), 0.7 (◆), 1.0 (Δ), 1.2 (▼), and 1.5 (○).	157
Figure 47	Peak combustor pressures for hydrogen with $d = 1.09$ mm varying $f/f_{ideal}$ for $Q = 10$ cc/s and $\Phi = 1.0$ (●), $Q = 30$ cc/s and $\Phi = 0.8$ (□), $Q = 50$ cc/s and $\Phi = 0.6$ (◆), $Q = 75$ cc/s and $\Phi = 0.5$ (Δ), and $Q = 100$ cc/s and $\Phi = 0.5$ (▼).	158
Figure 48	Peak combustor pressures for propane with $\Phi = 1.0$ and $d = 1.09$ mm varying $f/f_{ideal}$ for $Q = 10$ cc/s (●), 30 cc/s (□), 50 cc/s (◆), and 75 cc/s (Δ).	158
Figure 49	Phase-averaged combustor pressure for hydrogen ( $d = 1.09$ mm, $F = 1.0$ ) for $E = 2$ (●), 5 (□), 10 (◆), 20 (Δ), 40 (▼) mJ from CDI system and automotive system (○, $50 < E < 100$ mJ) .	159
Figure 50	Isometric view of leading edge of airfoil with integrated bank of 8 combustion-driven jet actuators (a) with cross-sectional view along midline of combustor (b).	160
Figure 51	PIV vector fields and vorticity contours for baseline case ( $\alpha = 24.1^\circ$ , $U_\infty = 12.5$ m/s, $Re_c = 1.80 \times 10^5$ ) with actuator fully off (a) and steady flow with no ignition (b).	161
Figure 52	PIV vector fields and vorticity contours for baseline case ( $\alpha = 24.1^\circ$ , $U_\infty = 25.0$ m/s, $Re_c = 3.60 \times 10^5$ ) with actuator fully off (a) and steady flow with no ignition (b).	161
Figure 53	Smoke flow visualization images for transient case ( $f = 3$ Hz) with $\alpha = 24.1^\circ$ and $U_\infty = 12.5$ m/s for $t = 0$ (a), 1 (b), 2 (c), 3 (d), 5 (e), 8 (f), 12 (g), 15 (h), and 20 ms (i).	162
Figure 54	Smoke flow visualization images for dynamic case ( $f = 45$ Hz) with $\alpha = 24.1^\circ$ and $U_\infty = 12.5$ m/s for $t = 1$ (a), 2 (b), 3 (c), 6 (d), 9 (e), 12 (f), 15 (g), and 20 ms (h).	163

Figure 55	PIV velocity vector fields and vorticity contours for $\alpha = 24.1^\circ$ and $U_\infty = 25.0$ m/s with $f = 15$ Hz ( $St = 0.137$ ) for $t/\tau = 0.045$ (a), 0.090 (b), 0.135 (c), 0.180 (d), 0.225 (e), 0.300 (f), 0.450 (g), and 0.600 (h).	164
Figure 56	PIV velocity vector fields and vorticity contours for $\alpha = 24.1^\circ$ and $U_\infty = 25.0$ m/s with $f = 30$ Hz ( $St = 0.274$ ) for $t/\tau = 0.090$ (a), 0.180 (b), 0.270 (c), 0.360 (d), 0.450 (e), 0.600 (f), and 0.900 (g).	165
Figure 57	PIV velocity vector fields and vorticity contours for $\alpha = 24.1^\circ$ and $U_\infty = 12.5$ m/s with $f = 30$ Hz ( $St = 0.549$ ) for $t/\tau = 0.030$ (a), 0.090 (b), 0.180 (c), 0.270 (d), 0.360 (e), 0.450 (f), 0.600 (g), and 0.900 (h).	166
Figure 58	PIV velocity vector fields and vorticity contours for $\alpha = 24.1^\circ$ and $U_\infty = 12.5$ m/s with $f = 45$ Hz ( $St = 0.823$ ) for $t/\tau = 0.045$ (a), 0.090 (b), 0.135 (c), 0.270 (d), 0.405 (e), 0.540 (f), 0.675 (g), and 0.900 (h).	167
Figure 59	Phase-averaged cylinder pressures over cycle for compressible synthetic jet with $L_\phi/d = 2065$ and $r = 27.1$ varying orifice geometry for $l/d = 0.5$ (●), 2.0 (□), and 2.0 with $45^\circ$ chamfer on both sides of orifice (◆) with $f = 10$ (a), 25 (b), 50 (c), and 100 (d) Hz.	168
Figure 60	Phase-averaged combustor pressures for combustion driven jet actuator for stoichiometric hydrogen (a) and propane (b) mixtures with $Q = 10$ cc/s and $d = 1.30$ mm varying orifice geometry for $l/d = 0.75$ (●), 2.0 (□), and 2.0 with $45^\circ$ chamfer on orifice (◆). Note that pressure scales are different for (a) and (b).	169

## LIST OF TABLES

Table 1	Flammability limits and adiabatic combustion properties for hydrogen and propane.	51
Table 2	Comparison of ratios of time to peak pressure and ratios of flame speeds (from Law, 1993).	55
Table 3	Properties for combustion chambers with varying aspect ratio holding $V = 1$ cc.	64
Table 4	Properties for combustion chambers with varying chamber volume holding $H/D = 1.27$ .	68
Table 5	Mean refill flow properties varying flow rate for a 1 cc, $H/D = 1.27$ chamber.	71
Table 6	Combustion chamber pressure required to maintain desired steady flowrate ( $Q$ ) through given orifice diameter ( $d$ ).	79
Table 7	Calculated dimensionless momentum coefficients for low speed separation control experiments with combustion-driven jet actuators.	92



## LIST OF SYMBOLS

$A$	orifice area
$A_p$	planform area of airfoil
BDC	bottom dead center (piston stroke)
$c$	speed of sound at STP
$C$	chord length of airfoil
$C_\mu$	dimensionless momentum coefficient [ $\equiv (\rho_{jet} A U_{jet}) / (\rho_\infty A_p U_\infty)$ ]
$d$	orifice diameter
$D$	combustion chamber diameter
$E$	ignition energy
$f$	actuation frequency
$f_{ideal}$	frequency at which system is fired once per unit time that it takes to refill the combustion chamber with mixture [ $\equiv Q/V$ ]
$F$	Momentum flux at exhaust orifice
$h$	distance to spark gap from inlet along primary flow axis
$H$	combustion chamber height
$l$	orifice plate thickness
$L_0$	normalized stroke length [ $\equiv V/A$ ]
$L_s$	streamwise spacing of shock cells in an underexpanded supersonic jet
$m$	air mass contained within the cylinder
$m_d$	mass displacement over a single cycle
$m_0$	air mass contained within the cylinder at BDC at STP
$m'$	mass flux at the orifice

$m_c'$	mass flux at the orifice for choked suction flow
$M$	Mach number
$P_r$	normalized pressure [ $\equiv$ pressure/atmospheric pressure]
$Q$	volumetric flow rate of gas into the combustion chamber
$r$	compression ratio [ $\equiv V_{BDC}/V_{TDC}$ ]
$R$	radial distance from orifice center
$Re$	Reynolds number [ $\equiv Ud/\nu$ ]
$S_L$	laminar flame speed
$S_T$	turbulent flame speed
$St$	Strouhal number, typically based on chord length [ $\equiv fC/U_\infty$ ]
$St_{Lo}$	Strouhal number based on $L_o$ [ $\equiv fL_o/c$ ]
STP	standard temperature and pressure (300 °K and 1 atm)
$t$	time (referenced from BDC or ignition for compressible synthetic jet and combustion-driven jet actuator, respectively)
$t_{peak}$	time to peak pressure (referenced from ignition)
$t_{pulse}$	time duration of the high pressure generated by the combustion process
$t_{refill}$	time duration of flow of new reactants into the combustion chamber
$T_r$	normalized temperature [ $\equiv$ temperature/atmospheric temperature]
TDC	top dead center (piston stroke)
TTL	transistor-transistor logic (i.e., 0-5 V square wave digital signal)
$U$	velocity (downstream component)
$U_\infty$	freestream velocity
$V$	volume displacement of piston or volume of combustion chamber (for compressible synthetic jet and combustion-driven jet actuator, respectively)

$V_{BDC}$	cylinder volume at BDC
$V_{TDC}$	cylinder volume at TDC
$X$	downstream distance from orifice
$Y$	cross-stream distance from orifice centerline
$\alpha$	thermal diffusivity or airfoil angle of attack (Chapters 4 and 5, respectively)
$\delta_L$	laminar flame thickness
$\gamma$	specific heat ratio
$\nu$	kinematic viscosity
$\rho$	density
$\tau$	cycle period [ = 1/ $f$ ]
$\Phi$	normalized fuel/air ratio [1.0 = stoichiometric; < 1.0 indicates fuel lean]
$\infty$	freestream properties

## SUMMARY

In order to extend fluid-based flow control techniques that have been demonstrated at low subsonic speeds to high speed flows, it is necessary to develop actuators having sufficient momentum to control and manipulate high speed flows. Two fluidic actuation approaches are developed where the control jet may reach supersonic velocities and their performance is characterized. The first actuator is a compressible synthetic (zero net mass flux) jet. This is an extension of previous work on synthetic jets with an increase in driver power yielding substantial pressurization of the cavity such that the flow is compressible. The jet is generated using a piston/cylinder actuator, and the effects of variation of the orifice diameter, actuation frequency, and compression ratio are investigated. Operation in the compressible regime uniquely affects the time-dependent cylinder pressure in that the duty cycle of the system shifts such that the suction phase is longer than the blowing phase. The structure of the jet in the near-field is documented using particle image velocimetry and Schlieren flow visualization. In the range investigated, the stroke length is sufficiently long that the jet flow is dominated by a starting jet rather than a starting vortex (which is typical of low-speed synthetic jets). A simple, quasi-static numerical model of the cylinder pressure is developed and is in generally good agreement with the experimental results. This model is used to assess system parameters which could not be measured directly (e.g., the dynamic gas temperature and mass within the cylinder) and for predictions of the actuator performance beyond the current experimental range. Finally, an experiment is described with self-

actuated valves mounted into the cylinder head which effectively increase the orifice area in suction and overcome some of the limitations inherent to compressible operation.

The second actuation concept is the combustion-driven jet actuator. This device consists of a small-scale (nominally 1 cc) combustion chamber which is filled with premixed fuel and oxidizer. The mixture is ignited using an integrated spark gap, creating a momentary high pressure burst within the combustor that drives a high-speed jet from an exhaust orifice. At these scales, the entire combustion process is complete within several milliseconds and the cycle resumes when fresh fuel/oxidizer is fed into the chamber and displaces the remaining combustion products. The actuator performance is characterized by using dynamic measurements of the combustor pressure along with Schlieren flow visualization, limited dynamic thrust measurements, and flame photography. The effects of variation in the following system parameters are investigated: fuel type and mixture ratio, exhaust orifice diameter, chamber aspect ratio, chamber volume, fuel/air flow rate, ignition/combustion frequency, and spark ignition energy. The resulting performance trends are documented and the basis for each discussed. Finally, a proof-of-concept experiment demonstrates the utility of the combustion-driven jet actuators at low-speed for transitory reattachment of a separated flow over an airfoil at high angles of attack.

# CHAPTER I

## INTRODUCTION

### I.1. Overview

Controlled reattachment of separated flows over lifting surfaces at moderate and high angles of attack to improve aerodynamic performance and extend the flight envelope has been the focus of a number of investigations since the early eighties. In recent years, active control techniques have focused on introducing small disturbances in the upstream wall boundary layer, exploiting a Coanda-like effect to create unsteady reattachment of the flow. A variety of actuation techniques have been used to achieve these effects, including external acoustic excitation (Zaman, Bar-Sever, and Mangalam, 1987), internal acoustic excitation applied through a small orifice on the surface of the airfoil (Huang, et al, 1987 and Hsiao, et al, 1990), vibrating mechanical flaps on the airfoil surface (Neuberger and Wygnanski, 1987 and Shepshelovich and Koss, 1990), and steady and unsteady blowing from the surface into the cross-flow (Sigurdson and Roshko, 1985, Seifert, et al, 1993, and Johari and McManus, 1997). These techniques have been demonstrated with varying degrees of success, typically by applying excitation at a dimensionless frequency of  $St \sim O(1)$ , such that the excitation period is approximately same as the time of flight over the length of the reattached flow.

Ongoing research at Georgia Tech has led to the development and demonstration of synthetic jet actuators as useful tools for the control of shear flows. These devices consist

of enclosed cavities having a simple orifice where a jet is created by the time-periodic motion of a driver (typically a moving diaphragm within the cavity). The motion of the driver changes the volume of the cavity and induces subsequent blowing and suction phases during each cycle. The suction into the synthetic jet is localized and may be approximated as a sink flow at the orifice. The blowing phase, however, typically creates a discrete vortical structure which (in combination with vortices from previous cycles) breaks down into a turbulent jet in the far field (as shown schematically in Figure 1). Synthetic jets thus allow momentum transfer into the embedding flow even though they operate with zero net mass flux. The formation and evolution of synthetic jets in the absence of cross-flow has been extensively investigated by Smith and Glezer (1998) and in the Ph.D. thesis of Smith (1999). The utility of synthetic jets in modifying aerodynamic characteristics of bluff bodies and airfoils has been demonstrated by Amitay, et al, (1998 and 1999). These investigations differed from earlier flow control experiments in that the dimensionless frequency of excitation was at least an order of magnitude higher than the characteristic frequency of the flow [i.e.,  $St \geq O(10)$ ]. This technique is applicable over a broader range of flow conditions since it does not rely on coupling to global flow instabilities.

The earlier work on separation control techniques utilizing synthetic jets and pulsed blowing schemes has demonstrated success with actuators with a (dimensionless) momentum coefficient ( $C_\mu$ ) on the order of  $10^{-3}$ . While it is relatively simple to develop such actuators either for wind tunnel testing or for small-scale vehicles operating at relatively low speeds (e.g., unmanned aerial vehicles or microUAVs), it is clear that

actuators having similar (or even potentially higher) levels of momentum coefficient will be required for effective flow control at higher flight speeds (e.g., transonic or supersonic), thus necessitating high speed actuator jets and different actuation hardware. This thesis details the development of two novel actuators intended as potential solutions to this problem: the compressible synthetic jet and the combustion-driven jet actuator. The compressible synthetic jet is an extension of previous synthetic jet research with an increase in driver power which allows significant pressurization of the cavity and moves the zero net mass flux system into operation in the compressible regime. This is accomplished using a piston rather than the conventional piezoelectric membranes to drive the system.

The combustion-driven jet actuator is a novel actuation concept which exploits the chemical energy of a gaseous fuel/oxidizer mixture to create a high momentum jet of exhaust products. The basic element of the system may be regarded as, essentially, a fluidic amplifier where premixed fuel/oxidizer having relatively low momentum fills a small ( $\sim 1 \text{ cm}^3$ ) combustion chamber bounded by an orifice plate as shown schematically in Figure 2. A spark (or other ignition source) ignites the mixture, creating a high pressure burst within the combustor and a subsequent jet emanating from one or more exhaust orifices. At the scales envisioned, the entire combustion process is complete within several milliseconds and the cycle resumes with fresh fuel/oxidizer mixture entering the chamber and displacing the remaining combustion products. The cycle frequency is set by the spark/ignition source and is continuously variable, limited only in that the cycle period must be greater than the duration of the high pressure pulse



and the subsequent time required for the chamber to be refilled with new reactants. For a  $1\text{ cm}^3$  combustor, operating frequencies greater than 100 Hz have been achieved using hydrogen/air mixtures.

The remainder of this chapter includes a brief review of the previous research on synthetic jets as well as research into small scale combustion pertinent to the combustion-driven jet actuator. Chapter II focuses on the development and characterization of the compressible synthetic jet. This chapter begins with a review of the experimental set-up and measurement techniques (§II.1), including phase-locked cylinder pressure measurements, Schlieren flow visualization, and particle image velocimetry. Variation in three fundamental system parameters is investigated: orifice diameter, actuation frequency, and compression ratio. The effect of these parameters on cylinder pressure is detailed in §II.2, highlighting the unique effects of compressibility on the pressure curve and how it changes the duty cycle of the system towards longer periods in suction. The near-field jet structure outside the orifice is documented in §II.3 using PIV measurements and Schlieren flow visualization, noting in particular how the jet flow becomes dominated by a starting jet rather than the typical starting vortex structures which characterize low-speed synthetic jets. A simple, quasi-static model of the time-dependent cylinder pressure is presented in §II.4, with generally good agreement with the experimental results. This model is used for the verification of the dimensionless parameters, investigation of the predicted change in system variables which could not be directly measured (specifically the dynamic gas temperature and mass levels within the cylinder), and for making limited predictions about system performance beyond the

current experimental range. Finally, §II.5 details an experiment with self-actuated valves mounted into the cylinder head, effectively increasing the orifice area in suction and overcoming some of the limitations inherent to compressible operation.

Chapter III focuses on the characterization of performance of the combustion-driven jet actuator and begins with a more specific overview of the actuator cycle and operation (§III.1). The experimental set-up for the broad parametric study of the actuator is discussed in §III.2, and it is based primarily on phase-locked combustor pressure measurements, analysis of Schlieren flow visualization, limited dynamic thrust measurements, and flame photography. The variable system parameters include fuel type and mixture ratio, exhaust orifice diameter, chamber aspect ratio, chamber volume, fuel/air flow rate, ignition/combustion frequency, and spark ignition energy (discussed individually in §III.3.a through §III.3.g, respectively). The performance trends resulting from variation in each of these parameters (and how they interact with one another) are documented and the theoretical basis for each proposed and discussed.

Finally, Chapter IV will discuss a proof-of-concept experiment designed to demonstrate the utility of the combustion-driven jet actuators for low-speed flow control (the utility of synthetic jets in low-speed applications having already been amply demonstrated in the literature). The integration of these actuators into the leading edge of an airfoil and the experimental facility and measurements are discussed in §IV.1. The results are discussed in §IV.2, showing how these actuators may be utilized to create transient reattachment of separated flow over an airfoil at high angle of attack. Chapter V presents conclusions for

both actuation schemes (in §V.1 and §V.2, respectively). Following this is an appendix including a brief review of the effects of orifice shape on the steady-flow discharge coefficient of orifices and sample experimental results for the effect of orifice geometry on the time-dependent pressure curves of both actuation schemes.

## I.2 Synthetic Jets

The formation and evolution of synthetic jets in the absence of a cross-flow was first investigated by Smith and Glezer (1998) and in the Ph.D. thesis of Smith (1999). In these experiments, the jets were driven using piezoelectric drivers mounted in a cavity with an elongated (effectively 2-D) slot orifice to create synthetic jets, which consist of a train of counter-rotating vortex pairs which are formed at the edge of the orifice during the blowing phase of each stroke. These vortices apparently break down and coalesce into a turbulent jet in the far field. These drivers were typically operated at or near their resonance frequency (about 1 kHz) in order to maximize the volume displacement and the resultant stroke length. Following the convention of vortex ring literature, the synthetic jet is characterized by a dimensionless stroke length,  $L_0/d$  (or  $L_0/h$  for slot orifices), where  $L_0$  is the length of the incompressible “slug” of fluid that is displaced by the driver through the orifice. In the 2-D experiments of Smith and Glezer, the dimensionless stroke length was varied over the range  $5.3 \leq L_0/h \leq 25$ , and the peak jet speeds did not exceed 40 m/s. Smith, Trautman, and Glezer (1999) report results for synthetic jets with round orifices where  $0.4 \leq L_0/d \leq 2.2$  with jet speeds up to 30 m/s and peak cavity pressures of 1.02 atmospheres. At these conditions, the synthetic jet is

essentially incompressible (where it is assumed that for changes in density that are below 5% compressibility effects may be neglected, with such density change corresponding to jet velocities of roughly 100 m/s and cavity pressures of 1.07 atmospheres). The jet structure in these studies consisted almost entirely of vortex pairs with little if any starting jet behind the vortex. This behavior is largely a function of the dimensionless stroke length. Gharib, Rambod, and Shariff (1998) have shown that for round orifices  $L_0/d = 4$  (referred to as the “formation number” in their work) is the characteristic level at which the transition occurs between single vortex ejection and vortex ejection followed by a trailing jet. Similar surveys for slot orifices have apparently not been performed, and the slot geometry may not be conducive to developing a single  $L_0/h$  transition number regardless of aspect ratio.

The utility of piezoelectric synthetic jets for flow control has been demonstrated in several experiments that encompass a range of applications. Among these are vectoring of adjacent air jets (Smith and Glezer, 2002), modification of aerodynamic characteristics of bluff bodies (Amitay, et al, 1997 and 1998), control of lift and drag on airfoils (Smith, et al, 1998, Seifert and Pack, 1999, and Amitay, et al, 1999 and 2000), reducing skin friction on a flat plate boundary layer (Lorkowski, et al, 1997), mixing control of jets (Davis and Glezer, 1999), control of internal flow separation (Amitay, et al, 2000), and control of cavity oscillations (Fabris and Williams, 1999, and Lamp and Chokani, 1999). Piezoelectric synthetic jets have also been investigated numerically by a number of sources. These studies have focused on the characteristics of the actuator flowfield of an isolated actuator (Rizzetta, et al, 1999, and Kral, et al, 1997) as well as the flowfield of an

actuator in a cross-flow (Mittal, et al, 2001). Additional work on piezoelectric synthetic jets was directed towards the development of synthetic jet actuators for batch fabrication using MEMS technologies (Coe, et al, 1994 and Muller, et al, 2001). Although not all of the above sources characterized their experiments in terms of  $L_0/d$  (or  $L_0/h$ ), their results are consistent with those from Smith and Glezer, showing jets composed of trains of vortices with little or no starting jets and peak jet speeds not exceeding 60 m/s.

Synthetic jets driven by piezoelectric diaphragms have several significant drawbacks. Since their performance in terms of volume displacement can vary significantly with the driving frequency and the driver size and material, these devices are typically driven at resonance and therefore have a fairly limited frequency range to maintain effective operation. Furthermore, limitations on voltage input for driver displacement, driver force, and dimensional tolerances between the cavity and the driver place an upper limit on the cavity pressures (and subsequent jet speeds) that may be generated with piezoelectric diaphragms. Several alternate (non-piezoelectric) synthetic jet drivers have been tested. A membrane driven by an electromechanical shaker to generate a synthetic jet in water was reported by Rediniotis, et al (1999), with  $L_0/d < 2.5$  and jet speeds not exceeding 0.1 m/s. Similar electromechanical shaker experiments were conducted in air by Crook and Wood (2001) with  $1.28 \leq L_0/d \leq 8.9$  and jet speeds up to 6.5 m/s.

Two earlier investigations of piston driven synthetic jets are noteworthy. Ahmed and Bangash (2001) used a piston driven by a linear actuator with a sawtooth waveform in water experiments with jet speeds not exceeding 1 m/s and  $L_0/d \leq 11.5$ . Gillaranz, Traub,

and Rediniotis (2002) have used pistons driven by a rotary crankshaft to generate synthetic jets in flow control experiments with a NACA 0015 airfoil. These actuators had a fixed 2 mm exit slot with  $L_0/h = 114$  (no details of the resulting jet structure were given). However, their primary interest in using pistons as drivers was to have a driver with broad frequency range without the need to match any mechanical or acoustical resonances for improved performance. They did not attempt to exploit the tight tolerances possible with pistons to achieve large chamber pressures and high jet speeds, and their experiments were limited to jet speeds less than 90 m/s. (In fact, they state explicitly that they designed their experiment to avoid compressibility effects.)

### I.3 Small-Scale Combustion

Small-scale combustion is an area of renewed interest with the growth of MEMS technology and schemes for small-scale, distributed power generation referred to as Power MEMS (Epstein, et al, 1997). A number of approaches for MEMS based generators have been developed recently to take advantage of the high energy density of chemical fuels compared to conventional batteries. The most prominent of these is the micro-gas turbine project at MIT. The development of the micro-gas turbine has been reported in a number of papers detailing the combustion properties for a micro-scale steady burner (Waitz, et al, 1998), the material selection and concerns for such a device (Spearing and Chen, 1997), and the detailed MEMS fabrication approach for a silicon wafer based micro-turbine engine (Mehra, et al, 2000). Other types of MEMS based

power generators are also under development, including micro rotary (Wankel) engines (Fu, et al, 2001 and Jiang, et al, 2001) and reciprocating free pistons driven by opposed pairs of small-scale combustion chambers (Lee, et al, 2002).

Small-scale combustion is fundamentally limited by the heat transfer from the hot combustion gases to the walls of the combustion chamber. When the energy loss due to heat transfer to the walls is greater than the energy generated by the combustion process, the flame is not self-sustaining and extinguishes. For a given configuration (typically tube diameter or distance between parallel plates), the critical dimension associated with this extinction process is known as the quenching distance. For stoichiometric, quiescent mixtures of hydrogen/air and propane/air at STP, the quenching distance between parallel plates is 0.64 mm and 2.0 mm, respectively (Turns, 1996). Quenching distance is a function of both initial gas pressure and temperature and decreases as one or both increase (Lewis and Von Elbe, 1987). The effect of mixture ratio quenching distance varies somewhat with fuel type, with hydrogen having minimum values at nearly exactly stoichiometric (Drell and Belles, 1958) while most hydrocarbons (including propane) having minimum values at somewhat fuel rich conditions (Lewis and von Elbe, 1987). Quenching distance is also dependent on flow conditions in non-quiescent mixtures and increases with both flow velocity and turbulence intensity (Ballal and Lefebvre, 1975).

Combustion in small dimensions is typically achieved by raising the initial pressure of the gas prior to ignition, thus reducing the quenching distance and increasing the chemical energy release for a given volume of mixture. A number of applications use

this approach, including small-scale engines used for model aircraft as well as most of the MEMS based generator concepts described earlier. The combustion-driven jet actuator only allows minimal pre-pressurization since the system is open to the atmosphere at the exhaust orifice (see Figure 2 or chapter III for details). Small-scale combustion near atmospheric pressure has not been investigated extensively beyond quenching distance studies (which are typically performed in open-ended channels or tubes). Recently, Faulkner, Scarborough, and Jagoda (2000) investigated ignition and flame propagation in closed rectangular combustors having high surface area-to-volume ratio using propane/air mixtures. Successful combustion was demonstrated in cross sectional dimensions as small as 3.1 mm. The peak chamber pressure and duration of the pressure pulse were found to be directly related to the volume to surface area ratio such that higher volume per unit surface area produced higher pressure peaks (by effectively reducing losses to heat transfer at the walls). Lee, Choi, and Kwon (2001) performed similar tests with hydrogen/air mixtures in closed, high-aspect ratio cylindrical volumes and found similar results for the effect of surface area to volume ratio and a minimum chamber dimension of 2.0 mm for successful hydrogen/air combustion at STP. Both of these studies were performed with quiescent gas mixtures within the combustion chamber, so minimum chamber dimensions can be expected to increase for dynamic cases where flow velocity and turbulence intensity within the chamber will be higher (due to fast refill of the chamber with new reactants).



## CHAPTER II

### COMPRESSIBLE SYNTHETIC JETS

#### II.1 Experimental Set-Up and Measurements

In the present experiments, the synthetic jet is formed by the sinusoidal, time harmonic motion of a 21.2 mm diameter piston within a matching cylinder with a stroke of 18.4 mm such that the volume displacement is 6.49 cc (shown schematically in Figure 3). The top surface of the cylinder is an interchangeable orifice plate, with axisymmetric and sharp-edged orifices of varying diameter,  $d$ , ( $1.6 \leq d \leq 4.8$  mm), and the corresponding variation in the dimensionless stroke length,  $L_0/d$ , is from 2065 to 76. The orifice plate thickness,  $l$ , is varied to maintain dimensional similarity, such that  $l/d = 2.0$  for all orifices. (A limited discussion of results for alternate orifice geometries may be found in the appendix following the text.) The minimum clearance between the piston and the orifice plate at top dead center (TDC) is 0.7 mm, yielding a maximum compression ratio,  $r$  ( $\equiv V_{BDC}/V_{TDC}$ ), of 27.1. Spacer plates are added between the cylinder head and the orifice plate such that the compression ratio is varied between 27.1 and 3.2.

The piston is linked to an AC/DC universal motor by means of a helical beam coupling. The motor has a maximum rated speed of 12,000 rpm (200Hz) and the speed (and the resulting actuation frequency,  $f$ ) is controlled using a variable AC drive which holds the frequency to within  $\pm 0.5$  Hz of the nominal level. The piston position and frequency are monitored using a 500 line-pair rotary encoder that outputs one TTL pulse train at the

rotation frequency and a second at its 500 multiple. The pulse train at the rotation frequency is aligned with TDC to within  $\pm 3^\circ$ . The higher frequency pulse train is used to vary the phase of data acquisition during the actuation cycle.

The dynamic pressure within the cylinder is measured using a series of piezoresistive pressure transducers (Endevco model 8510C) mounted within the cylinder head. Pressure transducers with ranges of 1, 15, 50, and 200 psig are used at the appropriate cylinder pressure levels, each with a frequency response not less than 100 kHz and an error not more than 1% FSO, including the combined effects of non-linearity, repeatability, and hysteresis. The transducer's output is sampled 500 times during the actuation cycle using the encoder signal as a clock, and the resulting pressure curve is phase-averaged over at least 100 cycles. The jet flow is visualized using a small-scale, single-pass Schlieren system, and the images are captured using a 768x484 pixel progressive scan CCD camera (Pulnix model TM 9701) having an asynchronous trigger which is used to phase-lock the image capture to the desired encoder point. Finally, the jet flow field is documented for representative cases using particle image velocimetry (PIV) measurements. These experiments are performed inside of a sealed glass enclosure, with the air inside the enclosure seeded with incense smoke (with seed particles drawn into the cylinder during each suction stroke). The flow is illuminated using a laser sheet from a double pulse ND-YAG laser, phase-locked to the desired encoder point, and image pairs were captured using a 1008x1016 pixel CCD camera and subsequently written to disk. A magnification of 27  $\mu\text{m}/\text{pixel}$  is used, where the nominal

particle dimension is sub-pixel. Velocity vectors are calculated using a standard cross-correlation technique and then phase-averaged over 100 realizations.

## II.2 Cylinder Pressure

The primary measure of the actuator performance is the variation of the time-dependent pressure within the cylinder during the actuation cycle which, for a given actuator configuration, affects the strength and evolution of the jet. The variation of the normalized cylinder pressure  $P_r$  (defined as the pressure ratio between the cylinder and ambient levels,  $P/P_{atm}$ ) over the actuation cycle for a compression ratio  $r = 27.1$  is presented in Figures 4b, c, and d for  $L_0/d = 76$ , 258, and 2065, respectively. At each length scale of the ejected fluid, the actuation frequency  $f$  is varied between 25 and 200 Hz at equal increments of 25 Hz. The sinusoidal piston position and normalized velocity over the cycle are presented for reference in Figure 4a, with the cycle phase-locked to the piston location, beginning and ending at BDC ( $t/\tau = 0$  and 1) with TDC corresponding to  $t/\tau = 0.5$ . At sufficiently low combinations of  $f$  and  $L_0/d$  (e.g.,  $f < 75$  Hz and  $L_0/d = 76$  - Figure 4b), the pressure curve is nearly symmetric about  $t/\tau = 0.5$  and generally follows the sinusoidal shape of the piston velocity curve, with blowing and suction phases corresponding directly to the periods of the upward and downward piston strokes, respectively. This pressure curve shape is typical of conventional low-speed synthetic jets over a broad frequency range (e.g., Smith, Trautman, and Glezer, 1999) indicating that the flow through the orifice is nominally symmetric during the two halves of the actuation cycle. In the current experiments for  $f = 25$  Hz and  $L_0/d = 76$ , the pressure

levels over the cycle are comparatively small ( $0.993 \leq P_r \leq 1.007$ ) and the system is nominally incompressible.

For a given  $L_0/d$ , increasing the frequency yields a monotonic increase in the peak pressure during the blowing stroke (e.g., for  $L_0/d = 76$ , the maximum  $P_r$  increases from 1.007 to 1.78 over the range  $25 \leq f \leq 200$  Hz). Similarly, the minimum pressure values over the cycle decrease substantially at increased frequencies (e.g., for  $L_0/d = 76$ , the minimum  $P_r$  decreases from 0.993 to 0.70 over the range of frequencies) yielding a pressure curve with greater extrema in both the blowing and suction phases of the cycle. Similar trends hold for variation in  $L_0/d$  while holding the frequency constant. At  $f = 25$  Hz, the pressure range over the cycle widens to  $0.65 \leq P_r \leq 1.93$  at  $L_0/d = 2065$  (Figure 4d) compared to the range noted above for  $L_0/d = 76$  ( $0.993 \leq P_r \leq 1.007$ ). These trends hold across any combination of values and, subsequently, the maximum range of cylinder pressures over the cycle ( $0.23 \leq P_r \leq 7.93$ ) was found at the highest combination within the experimental range ( $f = 200$  Hz and  $L_0/d = 2065$ ). From isentropic compressible flow properties, these pressure ratios are more than sufficient to generate sonic gas velocities at the orifice over at least a portion of both the blowing (sonic for  $P_r \geq 1.893$ ) and suction (sonic for  $P_r \leq 0.528$ ) phases of the cycle.

As the pressure magnitudes increase and compressibility effects develop within the cylinder, the pressure curve distorts from its initial sinusoidal shape and ceases to correspond directly to the piston motion. The time at which the maximum pressure over the cycle is reached (hereafter referred to as  $t_{peak}$ ) migrates monotonically towards the

time at which the piston is at TDC ( $t/\tau = 0.5$ ) and the cylinder volume is at a minimum as opposed to when the piston velocity (and the time rate of change of the volume of the cylinder) is highest (i.e., at  $t/\tau = 0.25$ ). For  $L_0/d = 76$ ,  $t_{peak}/\tau$  shifts from 0.26 at  $f = 25$  Hz up to 0.38 at  $f = 200$  Hz. This behavior occurs for all orifice diameters, and, at the maximum pressure level recorded (i.e., for  $L_0/d = 2065$  and  $f = 200$  Hz),  $t_{peak}/\tau = 0.47$ , nearly corresponding to TDC. At the same time, the pressure curve over the blowing phase ( $P_r > 1$ ) becomes distinctly asymmetric with a rise time that is typically longer than the characteristic fall time back to atmospheric pressure. This asymmetry is a combined effect of changes in both the piston velocity and the pressure-driven mass flow through the orifice (with the balance of these two parameters controlling the pressure curve over the cycle). Over the time frame in discussion ( $0.25 \leq t/\tau \leq 0.50$ ), the piston velocity decreases from its maximum value to zero, and correspondingly for  $t_{peak}/\tau > 0.25$ , the piston velocities on either side of the peak location are inherently asymmetric, with substantially reduced velocities for  $t > t_{peak}$  compared to  $t < t_{peak}$ . Also, over the blowing phase, the air mass within the cylinder,  $m$ , continuously decreases as air is ejected from the cylinder. However, the mass flux through the orifice ( $m'$ ) scales directly with  $P_r$  and thus increases until  $t_{peak}$  is reached. The result is that as the peak pressure moves further towards TDC (and subsequently lower  $m$ ), the impact of the mass flux on the rate of change of the pressure is greater (i.e., the mass flow through the orifice represents a greater proportion of the mass contained within the cylinder).

The suction phase of the cycle ( $P_r < 1$ ) also undergoes a change in shape as  $f$  and  $L_0/d$  are increased, resulting in a broader and flatter pressure curve over the suction. There is a

distinct change in the blowing-suction duty cycle, with a shift towards greater periods in suction. This effect can be more readily observed when  $P_r$  is plotted in polar coordinates (i.e., with the angular coordinate corresponding to the crank angle of the piston/cylinder) as shown for  $L_0/d = 612$  in Figures 5a, b, and c and  $f = 25, 100$ , and  $200$  Hz, respectively. The atmospheric pressure level ( $P_r = 1$ ) is denoted with a dashed reference circle and the suction phase of the cycle is shaded. For  $f = 25$  Hz (Figure 5a), the pressure range over the cycle is  $0.91 \leq P_r \leq 1.11$ , and the system spends almost exactly equal periods in blowing and suction, corresponding directly to the piston motion. For this case, the minimum pressure occurs at the middle of the downward stroke of the piston ( $t/\tau = 0.75$ ), when the downward piston velocity is maximum. However, even at this low frequency, the migration of the maximum pressure towards TDC is already apparent, with the highest value attained at  $t/\tau = 0.32$ . For  $f = 100$  Hz (Figure 5b), the cylinder pressures increase ( $0.45 \leq P_r \leq 3.55$  over the cycle), and the duty cycle shows a pronounced shift towards shorter periods in blowing ( $P_r > 1$  for  $0.15 \leq t/\tau \leq 0.51$ , 36% of the cycle period). This tendency is even stronger for  $f = 200$  Hz (Figure 5c) where the pressure range over the cycle is  $0.22 \leq P_r \leq 6.24$ , and the duration of the blowing phase is reduced to 29% of the cycle period ( $P_r > 1$  for  $0.25 \leq t/\tau \leq 0.54$ ).

The shift in duty cycle towards greater periods in suction appears to be a necessary result of increased cylinder pressures and operation in the compressible regime. During the blowing phase, the flow through the orifice is driven by the time-varying cylinder pressure which can reach multiple atmospheres, and the corresponding mass flow rate

continuously increases with the cylinder pressure even after the orifice is choked ( $P_r > 1.89$ ). In contrast, during the suction phase, the flow is driven by the ambient (atmospheric in the present experiments) pressure level which is invariant over the cycle. As a result, the suction flow is inherently driven by a lower pressure, and, in the limit of choked suction flow ( $P_r < 0.528$ ), the mass flow rate into the cylinder does not increase as the cylinder pressure further decreases. Therefore, in order to maintain zero net mass flux, the system must spend a larger fraction of the actuation cycle in suction. The limited pressure recovery over the suction phase is also apparent in Figure 5, where the duty cycle shift is predominantly a result of a delay in when the cycle transitions from suction to blowing. By contrast, the transition from blowing to suction takes place comparatively close to TDC for all cases.

It is also noted that an oscillation in the pressure signal is observed for some experimental cases near TDC (see Figure 4b). The oscillation is typically observed when the cylinder pressure is approximately at the atmospheric level ( $P_r = 1$ ) and is apparently a result of a dynamic “overshoot” in the blowing phase. The frequency of this oscillation corresponds closely to the Helmholtz frequency of the cylinder cavity at TDC (for  $L_0/d = 76$ , the Helmholtz frequency is 5.4 kHz). For higher pressure cases (see Figure 4d), the oscillation is not observed since, at TDC, the cavity pressure is still well above the atmospheric level. In all cases, the amplitude is small in comparison to the magnitude of the pressure peak, and over the experimental range, it may be stated that cavity resonances have an extremely small effect on the cylinder pressure.

The variation of the maximum and minimum cylinder pressures over the cycle with frequency is shown in Figures 6a and b, respectively. These data are measured for a fixed compression ratio ( $r = 27.1$ ) for several orifice diameters, and the pressures corresponding to sonic orifice speeds are denoted by dashed lines. Again as  $L_0/d$  is increased, wider pressure ranges over the cycle are observed with higher maximum and lower minimum pressures. Sonic pressure ratios are reached over a wide range of orifice diameters, but due to the duty cycle shift in the cycle, sonic speed is achieved at lower frequencies during the blowing phase compared to the suction phase. These data may be reduced further by introducing a new dimensionless frequency based upon the normalized stroke length,  $St_{L_0}$  ( $\equiv fL_0/c$  where  $c$  is the speed of sound at STP). When the pressure data of Figures 6a and b are plotted in terms of  $St_{L_0}$  (in Figures 7a and b), there is a remarkable collapse onto a single curve for all values of  $L_0/d$  for both the blowing and suction phases. The physical significance of this parameter is indicated by examination of its individual components:

$$St_{L_0} = \frac{fL_0}{c} = \frac{\left(\frac{1}{\tau}\right)\left(\frac{V}{A}\right)}{c} = \frac{\left(\frac{V}{A\tau}\right)}{c}$$

The displacement volume,  $V$  (not varied in these experiments), scales with the ideal, incompressible mass displacement of the piston. The term  $A\tau$  (the orifice area times the cycle period) essentially scales with the mass flow through the orifice over the cycle (dependent upon the time-varying cylinder pressure). Thus,  $St_{L_0}$  represents a ratio between the ideal mass displacement of the system and the actual mass displacement



which takes place, scaled by a reference velocity. (The speed of sound is used here since no independent velocity scale is available for the actuator characterization; any independent reference velocity may be used in place of  $c$  with the same essential result.) As either the orifice diameter is decreased (i.e., decreasing  $A$ ) or the frequency is increased (i.e., decreasing  $\tau$ ),  $St_{Lo}$  increases, the mass displacement becomes more limited, and thus the pressurization of the cylinder increases.

The cylinder pressures over the cycle for  $St_{Lo} = 0.1, 0.2$ , and  $0.48$  are shown in Figures 8a, b, and c, respectively, for five orifice diameters (only three orifice diameters are presented for  $St_{Lo} = 0.48$  since the remaining two could not reach this value within the frequency limit of 200 Hz). The shapes of the pressure curves at each value of  $St_{Lo}$  are essentially invariant with the peak pressures shifted towards TDC to the same degree and similar duty cycles. There is some disagreement in the pressure magnitudes over the cycle, with cases with lower  $L_o/d$  (i.e., larger orifice diameter) exhibiting typically more extreme pressure curves. (This behavior is also apparent upon close examination of Figure 7.) This effect is likely the result of unsteady losses at the orifice since the frequency must be greater for larger orifice diameters to maintain constant  $St_{Lo}$ . (The increasing unsteady losses through the orifice are documented further in the Appendix following the text.) Nonetheless,  $St_{Lo}$  appears to be a key characterization parameter for the compressible synthetic jet.

The variation of the phase-averaged cylinder pressure with the compression ratio ( $3.2 \leq r \leq 27.1$ ) for  $f = 100$  Hz and  $L_o/d$  ( $St_{Lo}$ ) = 76 (0.15), 258 (0.24), and 2065 (0.96) is shown in

Figures 9a, b, and c, respectively. At low cylinder pressures (e.g.,  $L_0/d = 76$ , Figure 9a), the system operation is still largely incompressible and the effect of the compression ratio on the pressure amplitudes is minimal. As the cylinder pressures increase (e.g.,  $L_0/d = 258$ , Figure 9b), the pressure amplitudes during the blowing phase are substantially more affected by  $r$ , with greater compression ratios yielding higher maximum pressures (although the effect of the compression ratio during the suction phase remains minimal). Finally, at large cylinder pressures (e.g.,  $L_0/d = 2065$ , Figure 9c), the compression ratio has a substantial effect on both the blowing and suction phases, with greater pressure extrema for higher compression ratios. It is noteworthy that the migration of the peak pressure towards TDC is virtually invariant with  $r$  over the experimental range (e.g., for  $L_0/d = 2065$ ,  $0.47 \leq t_{peak}/\tau \leq 0.48$  for all compression ratios) and is thus apparently not a function of the pressure levels within the cylinder.

The variation of the phase-averaged cylinder pressure for a low compression ratio ( $r = 3.2$ ) is shown in Figure 10 for the same  $f$  and  $L_0/d$  presented in Figure 4 ( $r = 27.1$ ). The same general development of the pressure magnitudes is observed with increasing combinations of  $f$  and  $L_0/d$  (and resulting  $St_{L_0}$ ) yielding greater pressure extrema over both the blowing and suction phases. At the highest combination of values within the experimental range ( $f = 200$  Hz and  $L_0/d = 2065$ ), the pressure range over the cycle is  $0.47 \leq P_r \leq 2.31$ . Several distinctions in the development of the pressure curve over the cycle may be drawn in comparison to Figure 4. As noted above, the migration of the peak pressure towards TDC is observed regardless of the compression ratio. However, the shape of the pressure curve is markedly different for  $r = 3.2$ . Due to the lower

pressure magnitudes, the curve retains a more generally sinusoidal shape and the asymmetry between the rise and fall times of the blowing phase is less pronounced. As a result, the transition between the blowing and suction phases occurs later in the cycle for lower compression ratios (see Figure 9c). A shift in the duty cycle towards shorter periods in blowing still occurs but to a smaller degree than for higher compression ratios. For the highest pressure case for  $r = 3.2$  (described above),  $P_r$  is greater than 1 for  $0.28 \leq t/\tau \leq 0.67$  or 39 % of the cycle period (compared to  $P_r > 1$  for  $0.32 \leq t/\tau \leq 0.57$  or 25 % of the cycle period for  $r = 27.1$  at the same  $f$  and  $L_o/d$ ).

At high combinations of  $f$  and  $L_o/d$  for  $r = 3.2$  (Figure 10c), the pressure curve shapes and magnitudes become extremely similar. For  $L_o/d = 2065$ , frequency increase from 125 Hz to 200 Hz yields only a small increase in the maximum pressure ratio over the cycle (2.30 vs. 2.38). This behavior is further shown in Figures 11a and b, which show the maximum and minimum pressures over the cycle, respectively, for variation in  $St_{Lo}$  for four different compression ratios. As in Figures 7a and b (for  $r = 27.1$ ), the data for each compression ratio collapse onto a single curve over the entire range of frequencies and diameters, with larger orifice diameters having slightly greater pressure magnitudes at the same  $St_{Lo}$ . As noted previously, at low  $St_{Lo}$  ( $\leq 0.1$ ), the pressure magnitudes are largely invariant with compression ratio, but at higher  $St_{Lo}$ , larger compression ratios consistently yield greater peak pressures. The trend of the curves is suggestive of a peak maximum and minimum pressure level (and matching pressure curve) over the cycle which is approached asymptotically as  $St_{Lo}$  is increased. The trend appears to be fully developed over the experimental range for  $r = 3.2$ , and is indicated to a lesser degree for higher compression

ratios. This behavior will be discussed further in §II.4, where operation outside the current experimental range is investigated using a simple numerical model of the compressible synthetic jet.

### II.3 Jet Structure

As described in the introduction (Chapter 1), conventional synthetic jets are typically engendered by the formation and interactions of trains of successive vortical structures (e.g., vortex rings or vortex pairs for circular or rectangular orifices, respectively) that are formed at the jet orifice. In earlier work on synthetic jets,  $L_0/d$  was typically quite small (as noted by Gharib, et al, 1997, an isolated vortex is formed when  $L_0/d < 4$ ) and as a result, the volume of displaced fluid that was not rolled into the primary vortex was rather minimal. In the present experiments, the dimensionless stroke length range is  $76 \leq L_0/d \leq 2065$ , and it may be expected that substantial fluid is ejected behind the initial vortex. Sample Schlieren images from the peak blowing of a conventional synthetic jet and the compressible synthetic jet are shown in Figure 12. The conventional synthetic jet (Figure 12a - courtesy of Smith and Glezer, 1998) features a readily visible vortex pair located in the near field of the orifice with a turbulent jet in the far field produced by the breakdown of vortices from previous cycles. By contrast, the compressible synthetic jet (Figure 12b for  $r = 27.1$ ,  $L_0/d = 612$  and  $f = 120$  Hz) at peak blowing is dominated by a high speed starting jet which emanates from the orifice. For these conditions, the cylinder pressure ratio is above the sonic level (i.e.,  $P_r > 1.89$ ), and the jet structure includes shock cells characteristic of underexpanded supersonic jets.

Figure 13 shows a sequence of Schlieren images over the blowing phase of the compressible synthetic jet for  $f = 120$  Hz,  $r = 27.1$ ,  $L_0/d = 612$ ). The streamwise field of view extends between the orifice plane and  $X/d = 16.5$ . The images are obtained phase locked to the cylinder pressure (also shown in Figure 13) at  $t/\tau = 0.18, 0.28, 0.34, 0.40, 0.46, 0.50$ , and  $0.54$ . A starting vortex forms when the cylinder pressure exceeds the atmospheric pressure ( $P_r > 1$ ) at the beginning of the blowing phase and is visible at  $t/\tau = 0.18$  (Figure 13a). Previous experiments on impulsively started high-speed jets have typically employed shock tubes to create essentially instantaneous high velocity orifice flows (e.g., Elder and De Haas, 1952, Golub, 1994, and Ishii, 1999), where the vortex formation is driven by the high speed flow and affected by strong interactions with the initial shock waves. By contrast, the compressible synthetic jet features a gradual increase in the jet speed as the cylinder pressure increases, and thus the formation of the starting vortex is typically decoupled from the high-speed flow generated at the peak pressure levels. Owing to this gradual increase in jet speed, the starting vortex is relatively weak (as may be measured by the circulation of its core). While the starting vortex begins to move away from the orifice under its self induced velocity, it is clear that since the speed of the jet behind it continuously increases with the increasing cylinder pressure, the resulting advection is influenced by the development of the jet following the vortex. At  $t/\tau = 0.28$  (Figure 13b), the cylinder pressure is  $P_r = 1.51$ , which corresponds to a jet velocity at the orifice of approximately 270 m/s (assuming isentropic flow through the orifice and atmospheric temperature gas within the cylinder). A strong

starting jet is seen at the orifice at this point, and the initial starting vortex is no longer discernable as a discrete structure.

At  $t/\tau = 0.34$  (Figure 13c), the jet strength further increases, and the leading edge of the jet has penetrated beyond the streamwise field of view of the image. It is noteworthy that at this point in time,  $P_r = 2.22$  (greater than the ratio of 1.89 required for sonic jet velocities) but no shocks are yet observed in the jet. For  $t/\tau = 0.40$  (Figure 13d), the cylinder pressure (and resultant jet speed) continue to increase and faint oblique shocks are visible in the jet near the orifice. At roughly the peak pressure ( $t/\tau = 0.46$  - Figure 13e),  $P_r = 4.14$  (corresponding to an ideally expanded Mach number of 1.58 for  $\gamma = 1.4$ ) and a clear system of shock cells are visible, as expected for an underexpanded supersonic jet. The jet velocity begins to decrease beyond the pressure peak and by  $t/\tau = 0.50$  (Figure 13f),  $P_r = 1.97$  and the shock cells are again only faintly discernable. Finally, the suction phase begins at  $t/\tau = 0.52$  and the flow in the orifice reverses its direction. At  $t/\tau = 0.54$ , no jet is observed in the near field of the orifice, although the jet fluid that is ejected during the blowing phase continues to move downstream and PIV measurements suggest that similar to the observations of Smith and Glezer (1997), the makeup fluid pulled into the cylinder during the suction phase is primarily drawn from a localized region near the jet exit plane.

Particle image velocimetry is used to measure the phase-locked velocity and vorticity distributions of the flow field outside the orifice. The images are taken in a plane that contains the axis of symmetry of the orifice (i.e., the R-Z plane). Figures 14a through d

present PIV data focusing on the formation and advection of the starting vortex at the beginning of the blowing cycle for  $t/\tau = 0.12, 0.14, 0.16$ , and  $0.18$ , respectively, for a sample case of  $f = 100$  Hz,  $r = 27.1$ , and  $L_0/d = 258$  (larger orifice diameter than the Schlieren images of Figure 13 to allow more resolution on the vortex) along with the corresponding pressure curve. The rollup of the starting vortex is initially indicated by both the velocity vectors and the vorticity contours near the edge of the orifice at  $t/\tau = 0.12$  (Figure 14a), just after the pressure has risen above the atmospheric level. Over the range of Figure 14, the vortex appears to be advected away from the orifice with a nominally constant celerity of 30 m/s. It is remarkable that the celerity is virtually invariant with time even though the speed of the jet continuously increases over this period (the centerline jet velocity at the orifice is 79.1 m/s at  $t/\tau = 0.12$  and increases to 143.9 m/s at  $t/\tau = 0.18$ ). However, the downstream location of the vortex centerline consistently corresponds to the location at which the centerline streamwise jet velocity,  $U$ , is approximately 70 m/s. It may be noted from the vorticity contours that the starting vortex continuously weakens as it progresses downstream, and it apparently merges with the turbulent structure of the starting jet as the blowing cycle progresses. Even over this initial blowing period, the vortex clearly induces far smaller changes in the velocity field than the core of the jet, making the starting jet by far the dominant structure in the flow.

The high-speed blowing phase of the cycle (for  $f = 100$  Hz,  $r = 27.1$ , and  $L_0/d = 612$ ) is shown in Figure 15 with contours of the streamwise velocity and of the flow field and centerline velocity data. Although the high velocities over this period require that the spatial resolution of the PIV data is somewhat limited (there are only 7 data points

across the orifice diameter), these distributions are sufficient to mark the presence of shock cells within the jet. Weak cells first appear at  $t/\tau = 0.34$  (Figure 15b) when the core jet velocity at the orifice exceeds 425 m/s, and these cells grow in strength (and size) through  $t/\tau = 0.42$  (Figure 15d) after which they begin to decay. The streamwise spacing between the shock cells,  $L_s$ , is approximately  $1.3d$  at  $t/\tau = 0.42$ . Tam and Tanna (1982) found that the shock cell spacing for steady underexpanded supersonic jets may be approximated as

$$L_s = \frac{\pi d (M^2 - 1)^{0.5}}{2.405}$$

where  $M$  is the ideally expanded jet Mach number. This correlation yields good general agreement with the observed shock cell spacing ( $1.36d$ ) despite the unsteady nature of the jets in the experiment.

The streamwise distributions of the centerline velocity for these cases show a characteristic “sawtooth” pattern that is typical of velocity profiles of underexpanded supersonic jets before the velocity begins to diminish with increasing distance from the orifice. It is noted that the maximum speed over all of the blowing cases (nearly 600 m/s – Figure 15d) is greater than the expected speed for the measured peak cylinder pressure for these conditions (the maximum pressure ratio is 3.40 which with isentropic flow and assuming that the temperature of the flow is 300°K, yields an ideally expanded velocity of 491 m/s). This is likely attributable to an underestimate of the actual gas temperature. The strong compression of the gas within the cylinder raises both the pressure and the



temperature and in turn results in higher sonic gas velocity and higher velocities than would be predicted using the ambient temperature. (Substantially increased cylinder gas temperatures are confirmed by the numerical simulation presented in §II.4.)

Finally, Figure 16 shows velocity vector fields (from the PIV data) for  $f = 100$  Hz,  $r = 27.1$  and  $L_0/d = 612$  at several instances during the suction phase of the actuation cycle. The beginning of the suction phase is shown in Figures 16a and b (corresponding to  $t/\tau = 0.52$  and  $0.56$ , respectively) and the flow at the orifice resembles a sink flow with the velocity magnitude increasing as the distance from the orifice decreases. The remnants of the fluid from the end of the blowing phase (which slows as the ejection velocity decreases before the suction begins) are still visible but with diminished velocity within the field of view (to  $X/d = 11$ ) as the suction cycle progresses. Two sample records during the high strength suction cycle are shown in Figures 16c and d ( $t/\tau = 0.76$  and  $0.96$ , respectively), and the characteristic sink flow is consistent over the entire suction phase. The maximum velocity magnitude measured over the suction cycle for this case is roughly 125 m/s into the orifice, which is substantially less than the predicted (ideal) orifice velocity under isentropic conditions for the measured pressure (the minimum pressure ratio over the cycle is 0.477 which should be sufficient to yield sonic suction velocities at the orifice). This discrepancy is likely the result of the optical access constraints of the PIV measurements, which can only follow the flow outside of the orifice. The highest suction velocities should be attained at the edge of (or slightly within) the orifice, but flow in this location can not be measured since seed particles move out of the field of view of the camera over the time delay between image pairs.

## II.4 Numerical Simulation and Results

The variation of the pressure and other properties within the cylinder over the actuation cycle is computed using a quasi-static simulation. The simulation steps through time, beginning with a given piston position, cylinder pressure and temperature, and specified values for  $r$ ,  $f$ , and  $L_0/d$ . For a given time step, the new piston position and cylinder volume are computed and the resulting pressure and temperature are calculated for isentropic compression or expansion of an ideal gas. At each time step, the thermodynamic conditions within the cylinder are taken to be spatially uniform and it is assumed that the time to reach equilibrium during each step is negligible. Owing to the large ratio between the cylinder and orifice diameters, it is assumed that the dynamic pressure that is associated with the piston motion within the cylinder is negligible compared to the static pressure. (The validity of this assumption will vary with the stroke length and frequency of the actuator. For the current piston/cylinder, the maximum piston velocity over the experimental range –  $f \leq 200$  Hz – is 11.6 m/s, and the corresponding dynamic pressure for air taken at atmospheric conditions is 0.08 kPa).

The temperature and pressure for the given time step are taken to be the average of the “initial” and “final” values and are used in the one-dimensional isentropic (compressible) flow equations to calculate the mass flow rate in or out of the orifice (neglecting viscous losses at the orifice). The mass flow rate is assumed constant over the time step and is used to update the mass within the cylinder. From the updated mass, the cylinder

pressure and temperature are again computed (treating the mass flow as another isentropic compression or expansion) and the program is ready for the next time step. The specific heat of the gas inside the cylinder is corrected for the gas temperature, using a 3<sup>rd</sup> order polynomial fit to tabulated data (Cengel and Boles, 1989). The system is treated as adiabatic (heat transfer to or from the cylinder surfaces is neglected) with the exception of heat transfer by mass addition during the suction phase (which is treated as well mixed with the gas inside the cylinder such that the conditions remain spatially uniform at each time step).

The program is run with at least 5,000 time steps per cycle with the actual number of time steps increased at reduced frequencies and larger orifice sizes in order to mitigate oscillation in the solution about the atmospheric pressure level. The simulation continues to run until the flow over the actuation cycle becomes effectively zero net mass flux, with the convergence criteria that the mass flow through the orifice over the blowing and suction phases must be equivalent to within 0.05%. Convergence time depends on the accuracy of the initial cylinder pressure estimate and on the system parameters, but typically is not greater than 50 cycles.

One benefit of a numerical simulation of the actuator is that it allows an examination of trends for properties which can not be directly measured in the present experiments. Results for a sample case of  $r = 27.1$  and  $L_0/d = 258$  (varying  $f$ ) are presented in Figures 17a, b, c, and d for the variation over the cycle of pressure, temperature, air mass, and mass flux through the orifice, respectively. The pressure traces from the simulation

(Figure 17a) reflect all of the behavioral trends noted for the experimental data, including the increase in pressure magnitudes as the frequency is increased, the migration in the peak pressure towards TDC, and the corresponding changes in the duty cycle with increased periods in suction (all described in §II.2). The cavity resonances (and resultant pressure oscillations) sometimes observed in the experimental data near atmospheric pressure are not seen in the simulation results and, due to their characteristically small amplitudes, no effort was made to include this phenomenon in the modeling.

The corresponding temperature distributions (Figure 17b, normalized as  $T_r$ , the ratio between the cylinder and ambient temperature, taken as 300°K) generally follow the trends for the cylinder pressure with temperature increase and decrease corresponding to the pressure rise and fall and temperature peaks coincide with the pressure peaks. Significant variation of the gas temperature is observed over the cycle (e.g., for  $f = 200$  Hz, the temperature range is  $0.92 \leq T_r \leq 1.66$  or between 276 and 498°K). It is noteworthy that as the actuation frequency increases, the increased compression of gas within the cylinder causes the cycle-averaged temperature to increase monotonically above the ambient temperature. For the data in Figure 17b, the cycle-averaged temperatures are  $T_r = 1.01$  and  $1.66$  at  $f = 25$  and  $200$  Hz, respectively. This behavior is also reflected in that when the cylinder pressure becomes atmospheric at the end of the blowing phase (corresponding approximately to  $t/\tau = 0.5$  for all frequencies of the sample case), the gas temperature is consistently higher than ambient and the temperature traces exhibit a visible inflection point in the slope as cooler atmospheric air is drawn into the cavity. As noted above, the present model does not take into account heat transfer at the

cylinder walls due to compressive heating of the gas as the frequency and/or the compression ratio are increased, or orifice diameter is decreased. The simulation indicates that for high cylinder pressure cases the gas temperatures can vary widely (e.g., for  $r = 27.1$ ,  $L_0/d = 2065$ , and  $f = 200$  Hz, the predicted temperature variation over the cycle is between 258 and 801°K), and it is reasonable to assume that the adiabatic assumption of the model breaks down in these cases. Therefore, heat transfer effects will likely contribute to some disagreement between the experimental and simulated pressures.

The air mass contained within the cylinder is presented in Figure 17c, normalized by the mass contained within the cylinder at BDC at atmospheric conditions,  $m_0$  (thus, for  $r = 27.1$ , the value of  $m/m_0$  can vary at most between 0.037 and 1.0). As expected, the maximum and minimum mass levels over the cycle correspond directly to the transitions between the blowing and suction phases (i.e, where  $P_r = 1$ ). It is noteworthy that as the actuation frequency is increased, the maximum air mass over the cycle (i.e., following the suction phase) decreases, but the minimum mass over the cycle (i.e., following the blowing phase) is virtually invariant, indicating that the pressure rise during the blowing phase is sufficient to eject most of the air out of the cavity. This again confirms the pressure recovery over the suction phase as a fundamental limitation on system performance. As a result of the decreasing maximum mass, the cycle-averaged mass and the total mass displacement decrease as the cylinder pressure magnitudes increase. Finally, the mass flux through the orifice during the actuation cycle,  $m'$ , is shown in Figure 17d (normalized by the choked mass flux in suction,  $m'_c$ ) and clearly corresponds

directly to the cylinder pressure (with high pressure generating negative mass flux). Perhaps the most prominent feature of these traces is the plateau in the mass flux at  $m'/m'_c = 1$  at high actuation frequencies (e.g.,  $f = 200$  Hz at  $0.70 \leq t/\tau \leq 0.97$ ) which indicates choked suction flow. In contrast (as discussed in §II.2), the flow out of the cylinder during the blowing phase increases continuously with increasing pressure, and its absolute magnitude can reach multiples of the choked suction level. It is notable that due to the reduced cycle period at higher actuation frequencies, the mass displacement over the cycle is reduced (as noted above) even though the mass flux per unit time is increasing.

The simulated pressure data of Figure 17a is for the same conditions ( $r = 27.1$  and  $L_o/d = 258$ ) as the experimental data presented in Figure 4c. A comparison between these plots reveals that although the simulation accurately matches the experimental trends it systematically underestimates the cylinder pressure magnitudes for these conditions. A direct comparison between the measured and simulated pressure time traces for  $f = 100$  Hz and  $L_o/d = 258$  and 2065 is made in Figures 18a and b for  $r = 27.1$  and 6.7, respectively. It is noteworthy that the agreement is typically better (in terms of percentage deviation) at higher  $L_o/d$  and therefore higher cylinder peak pressure levels than at low pressures where the simulation consistently predicts lower pressures. It is noteworthy that the simulation results in these cases are quite similar to the experimental results for larger orifice diameter (i.e., lower peak pressures and less pronounced shift of the peak pressure towards TDC). This suggests that the discrepancy between the

simulation and the measurement is due to the simulation's unrealistic assumption of inviscid, lossless flow through the orifice. For the experimental measurements, it is likely that a vena contracta forms within the orifice, causing the effective flow area to be smaller than the physical size of the orifice. Thus, the measurement might be expected to yield larger cylinder pressure magnitudes for the same frequency and compression ratio as the simulation. In principle, this effect can be accounted for by including an orifice discharge coefficient in the simulation; however, such a coefficient would likely need to vary over the actuation cycle to accurately model the unsteady orifice flow.

The cycle variations of the simulation data for five different combinations of  $f$  and  $L_0/d$  (such that  $St_{Lo} = 0.25$  for all cases) are shown in Figures 19a through d. For the idealized simulation model, the curves over the cycle for pressure, temperature, and mass (Figure 19a-c) are essentially identical for any combination of  $f$  and  $L_0/d$  with the same  $St_{Lo}$ , providing additional confirmation of the utility of this parameter in characterizing the compressible synthetic jet. The mass flux over the cycle (presented in Figure 19d normalized by the mass flux for choked suction flow for  $L_0/d = 76$ ) does vary between cases and scales directly with the orifice area,  $A$ . (This is a necessary result of the identical pressure curves in spite of the changing orifice diameter.) The air mass within the cylinder however remains the same since the total mass flow through the orifice scales with  $A \cdot \tau$ , and, to hold  $St_{Lo}$  constant at larger orifice diameters, the frequency is increased (and the cycle period  $\tau$  decreased). This result conforms to the essential balance of parameters within the  $St_{Lo}$  term (as presented in §II.2), where (for a fixed displacement volume)  $A \cdot \tau$  must be held constant for  $St_{Lo}$  to remain constant. The precise

agreement in the pressure curves is in some contrast to the experimental data of Figure 8, where there is slight disagreement in the pressure magnitudes for the same value of  $St_{Lo}$ . This again likely reflects the idealized orifice flow of the simulation, which does not attempt to account for orifice losses.

The variation with  $St_{Lo}$  of the normalized maximum and minimum pressures over the cycle is shown in Figures 20a and b, respectively. The experimental data (previously presented in Figure 11) and the results from the simulation are both shown, and the general agreement between the measured and predicted pressures at each compression ratio is quite good. The tendency of the simulation to under-predict the pressures at low  $St_{Lo}$  (possibly due to flow losses at the orifice) is observed here for each of the compression ratios. However, there is a slight tendency to over-predict at higher  $St_{Lo}$ , particularly at high compression ratios for which the pressure and temperature peaks are higher. As noted above, the assumption of adiabatic cylinder surfaces is probably inadequate in these cases, and the gas temperature fluctuations may be affected by the thermal mass of the cylinder wall, which may reduce the temperature variation and hence the pressure peaks.

With the aid of the numerical simulation, the system performance can be investigated outside of the range of the current operating parameters of the experimental setup. The variation of the predicted normalized maximum and minimum pressure peaks with  $St_{Lo}$  is extended to  $St_{Lo} = 10$  and is shown in Figures 21a and b, respectively. Over this range, the simulations show that the peak pressures asymptotically approach maximum and



minimum limits and become essentially invariant as  $St_{Lo}$  increases. In the limit, these peak pressure values may be approximated as

$$P_{r,\max} = (r)^{\gamma/2}$$

$$P_{r,\min} = (r)^{-\gamma/2}$$

which are included as dashed lines in Figure 21 for  $\gamma = 1.4$ . (Since simulation accounts for the decrease in specific heat with increasing temperature, at the higher compression ratios, the limit may be approached with  $\gamma$  somewhat less than 1.4). Thus, the ratio of the pressure peaks in terms of the corresponding cylinder volume is

$$\left( \frac{P_{r,\max}}{P_{r,\min}} \right) = \left( \frac{V_{BDC}}{V_{TDC}} \right)^\gamma$$

If the orifice is sealed, the minimum and maximum pressures are measured at BDC and TDC, respectively, and this expression is identical to the isentropic pressure-volume relation for an ideal gas in a closed system with constant specific heat. This closed system approximation is apparently reached in the limit of large  $St_{Lo}$  which (for a fixed displacement volume) can be increased by either decreasing the orifice area or increasing the actuation frequency. In either limit (i.e., increasingly smaller orifice area or increasingly smaller cycle period), the mass flow in or out of the cylinder approaches zero and the cylinder becomes essentially sealed.

Figure 22 shows the highest pressure traces recorded over the experimental range (i.e., for  $L_0/d = 2065$  and  $f = 200$  Hz) for each of the four compression ratios of the present investigation. These traces are compared with the isentropic pressure for an equivalent closed system (starting with the minimum pressure value at BDC from the above equation). The trends noted previously for the pressure curve (specifically the shift of the maximum pressure towards TDC) is consistent with development approaching the closed system limit, and for  $r = 3.2$  (Figure 22d), the curve shapes are nearly identical. For higher compression ratios, the match is increasingly less consistent, indicating that (as shown in Figure 21)  $St_{Lo}$  values well outside the experimental range are required to approach this limit. It is interesting to note for  $r = 6.7$  and  $3.2$  (Figures 22c and d) the measured peak pressure slightly surpasses the corresponding level for isentropic compression. This discrepancy may be attributed to deviations from true isentropic compression and expansion processes or flow losses at the orifice that may not be equivalent between the blowing and suction phases. Nonetheless, these peak values can provide a useful guideline for the design of compressible synthetic jets (e.g., the closed-system approximation suggests that in order to achieve sonic jet velocities,  $r \geq 2.49$  is required regardless of the value of  $St_{Lo}$ ).

Both the measurements and simulations suggest that the nearly-asymptotic peak pressure levels can be achieved at relatively low  $St_{Lo}$ , and that this value decreases as the compression ratio is decreased (see Figures 20 and 21). The effectively closed system is reached when the mass displacement over the cycle,  $m_d$ , is substantially smaller than the amount of mass that remains within the cylinder. The mass displacements from the

simulation are shown in Figure 23 over the extended range of  $St_{Lo}$ . The mass displacement is normalized by the maximum mass over the cycle,  $m_{max}$ , such that the value plotted is effectively the percentage of the mass within the cylinder that is ejected over each blowing cycle. In the low frequency limit (i.e., no pressurization of the cylinder)  $m_d/m_{max}$  is equal to  $(1 - r^{-1})$ , and thus, not unexpectedly, lower compression ratios inherently have lower percentage mass displacements. This value decreases as  $St_{Lo}$  is increased, with fast declines at lower compression ratio (e.g.,  $r = 3.2$ ) and much more gradual decline for higher compression ratios (e.g.,  $r = 27.1$ ). This is in part attributable to the higher pressures generated at high compression ratios which allow greater mass displacement at the same  $St_{Lo}$  relative to lower compression ratios. The closed system approximation indicates  $m_d/m_{max}$  will asymptotically approach zero as  $St_{Lo}$  is increased, and this behavior is suggested but not fully developed in Figure 23. It is noteworthy that the simulation predicts that the pressure levels (and curve over the cycle) become virtually invariant well before  $m_d/m_{max} = 0$  (see Figure 21 in comparison to Figure 23).

## II.5 Duty Cycle Modification

As noted previously, the performance of the compressible synthetic jet actuator is essentially limited by the pressure recovery (i.e., the mass of air that is drawn into the cavity) during the suction cycle. This variation in performance is manifested by a shift in the duty cycle towards greater periods in suction as depicted in Figure 5. In order to increase the cylinder pressure levels (and the mass flux and resultant jet momentum), it may be desirable to modify the actuator such that more air is allowed into the system

during suction. An experiment with a modified cylinder head is performed to indicate how this may be accomplished by placing secondary orifices in the cylinder head with check-valve devices that regulate the flow through these orifices (reed or flapper type valves are suitable to this application). A standard ( $l/d = 2.0$ ) orifice plate with  $d = 1.6$  mm is modified to include two additional orifices with diameters of 1.6 mm. A brass shim (0.08 mm thick) is placed between the orifice plate and the cylinder head. This shim is laser-cut such that the primary orifice is uncovered, but the secondary orifices are covered by rectangular, cantilevered flaps which are 2.5 mm wide by 3.8 mm long. The flaps are aligned such that the centerlines of the secondary orifices are 2.5 mm from the base of the cantilever. Although it is not currently possible to record the time-varying position of these flaps over the cycle, it is noted that minimal force is required to bend these thin flaps and thus their motion is expected to closely follow the pressure curve over the cycle.

The performance of the compressible synthetic jet with and without the presence of the two additional valved orifices is shown in Figure 24 for  $r = 27.1$  and  $f = 100$  Hz (the  $L_0/d$  for the primary orifice is 2065). For the unvalved head, the cylinder pressure range over the cycle is  $0.23 \leq P_r \leq 6.25$ , with  $P_r > 1$  for  $0.27 \leq t/\tau \leq 0.56$  (i.e., blowing over 29 % of the cycle). The addition of the valved orifices yields substantially higher maximum and minimum pressures over the cycle, with  $0.58 \leq P_r \leq 10.35$ . The greater minimum pressure indicates that pressure recovery is substantially aided by the valved cylinder head, with subsequently higher peak cylinder pressures (and resultant jet velocities) over the blowing phase. This also corresponds to a shift in the duty cycle back to nearly equal

periods in blowing and suction ( $P_r > 1$  for  $0.11 \leq t/\tau \leq 0.58$  or blowing over 47 % of the cycle), although there is still a phase shift between the piston motion and the cylinder pressure of approximately 25 degrees. Similar results are observed over a broad range of system parameters (provided that the cylinder pressures during the blowing and suction cycles are sufficient to open and close the valves). The use of valved heads allows the cylinder pressures generated by the compressible synthetic jet to exceed those indicated as the absolute upper limit by the numerical simulation (see §II.4) and thus could prove useful in flow control applications.

## CHAPTER III

### COMBUSTION-DRIVEN JET ACTUATORS

#### III.1 Overview

The concept behind the combustion-driven jet actuator was described briefly in Chapter I with schematic illustration in Figure 2. To reiterate, the device consists of a small-scale, low-volume ( $O \sim 1$  cc) combustion chamber that is bounded by an exhaust orifice and an inlet element which controls the flow of premixed fuel/oxidizer into the chamber. The mixture is ignited by an integrated spark gap, and the ensuing combustion process produces a high pressure within the chamber which generates a high velocity jet from the exhaust orifice and (for passive inlet elements) simultaneously stops the flow of fuel and oxidizer into the chamber. A conceptual diagram of the pressure-time history of the actuator is presented in Figure 25. The high pressure burst is essentially governed by a balance between the heat release and the subsequent pressure rise from the combustion process (which are affected by the fuel type, mixture ratio, and flame propagation properties) and the pressure reduction due to the flow through the exhaust orifice and heat transfer to the combustor walls. After the high pressure pulse within the chamber drops below the supply pressure (typically within several milliseconds) and following the characteristic dynamic response time of the inlet element, the flow of fresh reactants into the chamber resumes, displacing the remaining exhaust gases and filling the chamber for the next cycle. The repetition frequency of the combustion actuator is set entirely by the spark ignition rate and the refill flow rate and is limited by the characteristic times of the high pressure pulse within the chamber ( $t_{pulse}$ ) and the refill of reactants to the chamber

( $t_{refill}$ ). The actuator devices could also be operated in a non-premixed mode, requiring an additional characteristic mixing time of gases within the chamber ( $t_{mix}$ ) to be included in the cycle period. In the present work, attention is restricted to premixed operation of the actuator which allows operation at higher repetition frequency.

The overall cycle can be seen in Figure 26 which includes the pressure-time history within a 1 cc combustor and a sequence of corresponding phase-locked Schlieren flow images of the ejected jet at the exhaust orifice. The images are recorded at  $t = 0.44, 0.70, 1.2, 2, 3,$  and  $4.8$  ms following the spark trigger (using a  $125 \mu s$  shutter speed) and the streamwise field of view is approximately 25 orifice diameters ( $d = 1.30$  mm). Following the spark ignition ( $t = 0$ ), there is a sharp rise in the chamber pressure with a peak normalized pressure ( $P_r$ , defined as the ratio of the chamber pressure to atmospheric pressure) of approximately 2.8 at  $t = 0.7$  ms. A jet emanates from the exhaust orifice as soon as the pressure in the chamber begins to rise, with flow in the far field appearing to be turbulent as is evidenced by the presence of small-scale motions. The strength of the jet increases with the chamber pressure and, near the peak pressure level, shock cells are detected in the flow within 5 orifice diameters (6 mm) of the exhaust ( $P_r \geq 1.89$  required to generate sonic orifice velocities). The pressure subsequently decays and, at  $t = 2.7$  ms, reduces to atmospheric levels, at which point a jet no longer emanates from the exhaust orifice although its earlier flow field is visible in the far field. After a delay of 1.7 milliseconds, a small vortex ring appears at the orifice which is followed by a low-velocity steady jet, indicating the resumption of flow of fuel and oxidizer into the chamber and the displacement of remnant exhaust gases. The broad range of speed

variation from nearly zero velocity to supersonic speeds and then back to nearly zero is similar in principle to the development of a compressible synthetic jet during its blowing cycle (see § II.3).

The flow of fuel and oxidizer into the chamber for the small scale combustion device may be regulated through one of two approaches. The first option is active regulation of the flow through the use of small-scale electromechanical valves (potentially MEMS based). Such valves have the advantage of precise timing of the flow of reactants into the chamber, as well as tight closure of the upstream flow paths, ensuring that all flow (during the high pressure pulse) is forced out of the exhaust orifice. However, in this mode of operation, individual electronic valves would be required for each combustion actuator, along with the ancillary electronic hardware that is necessary for their operation. The second option is the use of passive valving elements which exploit the pressure rise within the chamber to shut off the inlet flow. These elements can be either mechanical (e.g., reed or flapper valves) or fluidic. Reed or flapper valves generally may be designed to close with minimal chamber overpressure and therefore prevent back flow of gas from the chamber into the feed line. Such valves can also be prestressed such that they do not open until the combustion process is completed. (This may be important since weak combustion near the chamber walls may continue briefly after the pressure in the chamber has dropped below the supply pressure level, and flow of fuel and oxidizer into the chamber during this period may reignite and create a standing flame within the combustor). However, such valves would still have to be integrated into arrays of combustion actuators and may require maintenance over time.



Fluidic elements typically obviate the need for moving mechanical hardware. While these elements typically can not provide tight closure of the inlets to the chamber during the combustion process, they can be designed to have a lower pressure drop in the downstream direction (i.e., into the combustion chamber) and therefore minimize backflow. Furthermore it appears that the integration of fluidic elements into the actuators during the manufacture process can be accomplished with relative ease. Within the context of the combustion actuator, these elements may be considered analogous to “aerovalves” in pulsed combustors which have numerous designs (as described in the review article of Putnam, Belles, and Kentfield, 1986). More elaborate designs based on classic fluidic vortex diodes were recently demonstrated by Lin, Hariharan, and Brogan (2002) for the control of gas flow into combustion chambers while minimizing the back flow of products. It is noteworthy that fluidic elements are particularly compatible with flow control applications, which typically emphasize simplicity and weight considerations as important design criteria.

The fluidic element in the present experiments utilizes a sheet of sintered stainless steel with 20  $\mu\text{m}$  porosity (1.6 mm thick), positioned immediately upstream of an array of orifices (nominally 350  $\mu\text{m}$  in diameter) that are laser cut in 0.1 mm thick brass sheet. These orifices are open to the combustion chamber and limit the area of the sintered surface that is exposed to the combustion chamber, effectively controlling the pressure drop across the fluidic element. The combined effect of these components is two-fold. First, both the orifice diameter and the porosity of the sintered metal porosity are

substantially smaller than the quenching distances for both hydrogen and propane, thereby preventing flame propagation into the premixed fuel/oxidizer delivery system. Second, the pressure drop and small passageways of the sintered metal allow a small amount of exhaust products from the combustion process to enter the sintered metal during the high pressure pulse of the combustion. After the high pressure dissipates (and allowing a dynamic time lag for the pressure drop), these exhaust products begin to re-enter the combustion chamber. During this time, weak burning may persist at chamber walls, and this arrangement prevents reignition and the formation of a steady flame by insuring that the first gases entering the chamber are not flammable. While more sophisticated and better optimized fluidic elements may certainly be utilized, the present set-up provides simplicity and repeatability for the purpose of the baseline tests that are described here. In the present experiments, the orifice grid includes an array of 29 orifices consisting of a central orifice on the chamber centerline and three concentric rings of 4, 8, and 16 orifices (with orifices spaced at equal angles for a given ring) located at 25%, 50%, and 75% of the chamber diameter, respectively. This orifice grid is used throughout the experiments except for variation in the chamber volume (see § III.3.c and Table 3 for further details of the orifice grids for those tests).

The present work focuses on a broad characterization of the actuator performance for changes in a number of system parameters that include: fuel type and mixture ratio ( $\Phi$ ), exhaust orifice diameter ( $d$ ), chamber volume ( $V$ ), chamber aspect ratio ( $H/D$ ), flowrate of reactants into the combustion chamber ( $Q$ ), ignition/combustion frequency ( $f$ ), and spark ignition energy ( $E$ ). The primary purpose here is to investigate performance trends

and sensitivity to changes in these variables and to provide reasonable guidelines for future systems that may have different characteristics from the range investigated here (e.g., combustion chambers of non-cylindrical cross-section, slot rather than round exhaust orifices, etc.).

### III.2 Experimental Set-Up and Measurements

A series of interchangeable aluminum combustion chambers were designed and fabricated to attach to a common base that includes the fluidic flow regulation element (see Figure 27 for schematic). Each of these chambers is cylindrical with circular cross-section and has chamber volume,  $V$ , diameter,  $D$ , and height,  $H$  (where  $H/D$  is the aspect ratio). In the baseline configuration, the chamber volume is 1 cubic centimeter with  $D = 1$  cm and  $H/D = 1.27$  (this configuration was used throughout the experiments except for specific tests for variation in volume and aspect ratio detailed in § III.3.c and III.3.d, respectively). The exhaust orifice plates were fabricated from stainless steel sheets of stock thicknesses with round, straight-walled orifices of diameter,  $d$ . The orifice plate thickness ( $l$ ) was chosen in relation to the diameter, such that  $1.9 < l/d < 2.1$ . (See Appendix A for further information on the effects of orifice geometry for both actuation schemes.) In all cases, the chambers were designed such that the flow through the exhaust orifice and fuel/oxidizer inlets is oriented along the same axis with the exhaust orifice located on the centerline of the chamber.

Hydrogen and propane are tested as viable fuels with both supplied from commercial high purity cylinders, while shop air from a locally available compressor is used as

oxidizer in all experiments. (Although pure oxygen may theoretically be used with the combustion actuator, it is not likely to be readily available in most flow control environments and is excluded from consideration here as a practical matter.) Fuel and air flow rates were measured separately using Aalborg thermal mass flowmeters calibrated for the appropriate gas and flow range (with a typical accuracy of 1% FSO). The gas flow rates were controlled through metering orifices or needle valves to set the mixture ratio,  $\Phi$ , and overall mixture flow rate,  $Q$ , with source pressures sufficiently high to ensure sonic flow through the orifice/valve and prevent changes in flow rate owing to downstream pressure fluctuations in the combustion chamber. The two streams are subsequently mixed through a bed of glass beads and injected into the combustion chamber through the integral fluidic element described above. Although the mixture ratio accuracy varies with the flowrate of each component gas over the ranges tested, the mixture ratios are correct to at least  $\pm 0.3$  for hydrogen and  $\pm 0.5$  for propane mixtures, with an overall flow rate accurate to within 5% of the nominal level.

The gas mixture is ignited by an integrated small-scale spark gap with a gap distance of 2 mm. In all cases, the spark orientation is normal to the axis of the chamber (and the direction of the bulk gas flow), with the midpoint of the gap at the chamber centerline. The spark elevation is at the midpoint of the chamber height (i.e.,  $h/H = 0.5$ ). For most experiments, the spark was produced with a standard automotive ignition system (Bosch ignition coil and 12V power supply) with a commercial electronic ignition control circuit triggered by a TTL signal at the desired frequency. (Intense electromagnetic interference associated with the ionization of gas at the spark gap is consistently observed

approximately 20  $\mu\text{s}$  after the rising edge of the trigger signal, so within the temporal resolution of most measurements the trigger signal and the actual spark ignition are taken to be simultaneous.) Although the ignition energy,  $E$ , of the automotive system is not measured directly, Adler (1995) gives the nominal value of automotive ignition systems as between 50 and 100 mJ. During tests of the ignition energy (§ III.3.g), a capacitive discharge ignition (CDI) system is used with a 25 kV pulse transformer to step-up the voltage in the capacitors (stored at 280 V). Although the efficiency of the pulse transformer is not assessed, it is assumed that the actual spark energy is not less than 75% of the stored energy of the capacitors. For both the automotive and CDI systems, the spark duration is between 0.5 and 2 ms (with the actual value depending upon the ignition energy and flow conditions within the combustion chamber.)

For most test cases, an ignition frequency of  $f = 1$  Hz was used. This low frequency (which is well below the idealized actuation frequency for the tested flow rates,  $f_{ideal} \equiv Q/V$ ) was selected so that mixing with exhaust from previous cycles as well as residual heating of the chamber walls from cycle to cycle could be considered negligible. (Results for increased frequencies are discussed in § III.3.f.) The chamber wall temperature is not considered as a variable in the present experiments since the flame temperature (over 2400 °K for stoichiometric mixtures of both fuels) is much higher than any desirable material wall temperature, making the temperature difference (and resultant heat transfer) between the burned gas and the wall substantial in any case. The baseline case of chamber walls at room temperature (with minimal residual heating from the

combustion process) is thus an effective worst case scenario for heat losses although not necessarily an unrealistic one.

The pressure within the combustion chamber is the primary measure of system performance. Dynamic pressure measurements are obtained with a high-temperature, piezoresistive pressure transducer (Endevco model 8544), with a frequency response of 192 kHz and an error of 0.5% FSO (including non-linearity, repeatability, and hysteresis). The transducer output is sampled at 100 kHz (with a National Instruments data acquisition board) using the TTL spark ignition signal as a timing reference, and the data are phase-averaged for each case over 100 realizations. Details of the flame propagation within the chamber itself are investigated using a cubical combustion chamber (1 cm on the sides) with a single pyrex wall for optical access. A standard CCD camera (768 by 464 pixels) is then used with a shutter speed of 125  $\mu$ s to capture sample images of the flame. A sequence of images at different instances during the combustion cycle is created using the vertical sync signal from the camera and a desired time delay to trigger the spark. Finally, limited dynamic thrust measurements are taken using a piezoresistive force sensor (PCB Piezotronics model 209C01), with the actuator mounted directly above the force transducer. However, the force sensor has a resonance frequency near 2 kHz, which results in substantial ringing in the signal on the same time scale as the combustion pulse. As a result only limited measurements at low combustor pressures are taken and these primarily used to confirm the validity of thrust values calculated directly from the dynamic pressure data.

### III.3 Parametric Study Results

#### III.3.a Fuel Type and Mixture Ratio

The fuel type and stoichiometry are arguably the most important system parameters since they set properties of the combustion process and the amount of chemical energy that can be released within the chamber. Table 1 (on the following page) includes the combustion properties of hydrogen and propane. The flammability limit data is found in Turns (1996) and is for initial conditions at STP, and the laminar flame speed data is from Law (1993). The adiabatic flame temperature and pressure are calculated (using the Thermochemical Calculator Program - available at <http://blue.caltech.edu/tcc/> as of December 2002), using only the major species for each reaction in the chemical kinetics equations (i.e.,  $H_2$ ,  $H_2O$ ,  $O_2$ ,  $N_2$ ,  $C_3H_8$ , and  $CO_2$  where appropriate), using the lower heating value for the relevant fuel, and beginning all processes at STP. It is noteworthy that hydrogen exhibits a substantially lower lean flammability limit as compared to propane ( $\Phi = 0.14$  vs.  $0.51$ ) but both have similar rich flammability limits (slightly greater than  $\Phi = 2.5$ ). The experiments presented here (and the calculations in Table 1) are limited to the fuel-lean regime within these flammability limits since it is ultimately desirable to minimize the fuel consumption for a given flow control system (particularly in flight systems where payload dedicated to flow control must be limited).

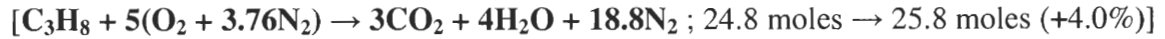
**Table 1.** Flammability limits and adiabatic combustion properties for hydrogen and propane.

Fuel Type	Flammability Limits ( $\Phi$ , 1 atm)	Mixture Ratio ( $\Phi$ )	Adiabatic Combustion Properties			
			$P=\text{constant}$ (1 atm)		$V=\text{constant}$	
			Flame Temperature (°K)	Flame Speed ( $S_L$ , cm/s)	Flame Temperature (°K)	Final Pressure (atm)
Hydrogen	0.14 – 2.54	1.0	2432.4	210	2861.3	8.24
		0.9	2340.4	190	2773.5	8.03
		0.8	2201.5	150	2637.5	7.71
		0.7	2034.9	125	2460.0	7.28
		0.6	1849.8	90	2249.0	6.74
		0.5	1648.0	60	2010.6	6.12
		0.4	1428.7	35	1746.5	5.40
Propane	0.51 – 2.83	1.0	2395.5	44	2909.0	10.09
		0.9	2235.6	39	2720.4	9.40
		0.8	2068.2	32	2521.8	8.68
		0.7	1892.4	23	2312.0	7.93
		0.6	1707.4	15	2089.7	7.14

Idealized combustion processes are generally treated as constant pressure or constant volume. The combustion-driven jet actuator however operates between these two limits because gas is vented as soon as the combustion process begins but the exhaust orifice is restrictive enough to ensure that pressure rise within the chamber. Of particular note is the final pressure for constant volume combustion (8.24 and 10.09 atm for stoichiometric hydrogen and propane, respectively), which is useful as an absolute upper bound on the pressure level that may be reached within the actuator (with initial mixture at STP). Actual values are expected to be substantially lower since the actuator combustion process is neither adiabatic nor constant volume. It is noteworthy that propane typically has higher chamber pressures than hydrogen for adiabatic, constant volume combustion, even though the constant volume flame temperature of hydrogen is



greater than that of propane (except at  $\Phi = 1.0$ , where it is slightly lower). This result reflects the mole change due to the combustion process, in which propane undergoes a positive mole change:



and hydrogen undergoes a negative mole change:



As the stoichiometry becomes leaner, this mole change plays a proportionally smaller role in determining the final pressure, and this (combined with the changing flame temperatures) causes the pressure difference between propane and hydrogen to narrow.

Also of importance to the combustion-driven jet actuator is the speed at which the flame propagates through the chamber, which controls the rate of heat release. The constant pressure laminar flame speeds,  $S_L$ , in Table 1, show that at stoichiometric mixture ratios hydrogen has substantially higher flame speeds than propane (210 vs. 44 cm/s). Both fuels exhibit reductions in  $S_L$  with leaner mixtures, with hydrogen decreasing faster on a percentage basis than propane. These values provide a good relative measure of the anticipated flame speed between the two fuels even though flame propagation in the combustion actuator is substantially more complicated than the idealized constant pressure case. In a closed chamber (or, in the case of the combustion actuator, a

chamber with restricted exhaust flow), flame speed decreases with increasing pressure, although the net velocity of the flame front may increase as the pocket of hot, burned gas behind the flame expands, creating a mean flow to which the flame propagation speed is added. Also, as discussed in §III.3.e, increases in the mixture flow rate can increase the turbulence within the chamber and change the overall flame propagation speed.

Traces of the phase-averaged combustor pressures during a single burst for the baseline combustor configuration are shown in Figures 28a and b for hydrogen and propane, respectively, for different mixture ratios in the chamber with  $Q = 10$  cc/s and  $d = 1.3$  mm. The pressures are normalized as the ratio between the chamber pressure and the ambient pressure,  $P_r$  (for all results here, this is effectively the same as reporting the pressure in atmospheres). (The slight oscillation in the pressure traces approximately 1.2 ms after ignition is a characteristic ringing noise that is generated by the ignition system at the end of the spark and may be observed to some extent in most of the results presented.) The results for decreasing (i.e., leaner) mixture ratios are generally as expected in that the peak pressure decreases and pulse duration increases. For hydrogen, the peak pressure varies from 4.41 to 1.23 over  $0.4 \leq \Phi \leq 1.0$  with corresponding  $t_{pulse}$  values ranging from 2.1 to 4.5 ms. Similarly, for propane, the peak pressure varies from 1.68 to 1.26 over  $0.8 \leq \Phi \leq 1.0$  with corresponding  $t_{pulse}$  ranging from 5.1 to 7.3 ms. This is a result of the combined effects of lower flame speeds and lower constant volume (CV) pressures. However, the large decrease in peak pressure with mixture ratio for hydrogen follows more closely the behavioral trend for its flame speed rather than the CV pressure. Comparison between hydrogen and propane also suggests that flame speed is an essential

parameter here, given that at stoichiometric mixtures (where the CV pressure for propane is substantially higher than that of hydrogen), hydrogen still shows a substantially greater pressure peak and shorter pulse duration than propane. The elapsed time from ignition to the peak pressure level,  $t_{peak}$ , is also informative, because it is expected to be inversely related to the flame propagation speed. Values for  $t_{peak}$  are listed in Table 2 (following page), as well as the comparative change in both  $t_{peak}$  and  $S_L$  with mixture ratio, using the stoichiometric hydrogen case as a baseline. The data shows an excellent agreement between these parameters for hydrogen with  $\Phi > 0.6$ , with lower hydrogen mixture ratios show marginally faster times to peak. By comparison, all propane mixtures exhibit slightly slower times to peak compared to the flame speed data. The peak pressure corresponds approximately to when the flame front reaches the walls of the chamber, with subsequent decreases in the heat release rate, allowing losses by venting and heat transfer to dominate. It should be noted that in all cases  $t_{peak}$  is substantially shorter than what would be expected for the flame to reach the chamber walls based on the laminar flame speed. For hydrogen at  $\Phi = 1.0$ ,  $t_{peak} = 0.66$  ms, yielding a net flame speed of 7.6 m/s to traverse the 5 mm radius of the chamber (compared to  $S_L = 2.1$  m/s). This net increase in the flame propagation speed is the result of the hot gas expansion behind the flame front (as demonstrated by flame photography in § III.3.e and specifically in Figure 39) and may account for some of the disagreement between cases. However, the overall agreement is still noteworthy and the trends confirm that flame propagation speed is a key parameter.

**Table 2.** Comparison of ratios of time to peak pressure and ratios of flame speeds (from Law, 1993).

Fuel Type	Mixture Ratio ( $\Phi$ )	Time to peak pressure ( $t_{peak,ms}$ )	$(t_{peak}/t_{peak,H2,\Phi=1.0})^{-1}$	$S_L/S_{L,H2,\Phi=1.0}$ (Table 1)
Hydrogen	1.0	0.66	1.00	1.00
	0.9	0.73	0.90	0.90
	0.8	0.91	0.73	0.71
	0.7	1.11	0.59	0.59
	0.6	1.44	0.46	0.42
	0.5	2.00	0.33	0.29
	0.4	3.10	0.21	0.17
Propane	1.0	3.47	0.19	0.21
	0.9	4.01	0.16	0.19
	0.8	5.51	0.12	0.15

As shown in Figures 28a and b, the actuator operates effectively with distinct combustion pulses and a significant pressure rise for  $\Phi \geq 0.4$  for hydrogen and  $\Phi \geq 0.8$  for propane. Below these values, the operation of the actuator is irregular and is characterized by either an incomplete combustion process or the formation of a standing flame within the chamber (which circumvents the refill and reignition cycle). This standing flame occurs when the chamber pressure is insufficient to stop the flow of reactants into the chamber during the combustion process. (In these cases, the flow of fuel or fuel/air mixture must be temporarily shut off to eliminate the standing flame and allow the cycle to begin again.) This performance is tied to the characteristics of the fluidic element that regulates reactant flow into the chamber and may be altered by using other regulation devices (passive or active).

### III.3.b Orifice Diameter

The diameter of the exhaust orifice effectively controls the rate at which exhaust gases are vented from the chamber. This is a crucial parameter which, in balance with the rate at which fuel is burned inside the chamber (effectively, the rate at which pressure is generated), controls both the peak pressure achieved and characteristic fall time of the pressure curve. Figures 29a and b show the phase-averaged pressure traces for a range of orifice diameters ( $0.79 \text{ mm} \leq d \leq 2.50 \text{ mm}$ ) where the fuel is hydrogen with  $\Phi = 1.0$  and  $0.5$ , respectively. Larger orifice diameters yield lower pressure peaks and shorter overall pulse durations as the exhaust products are vented more rapidly. It is noteworthy that for a given  $\Phi$ ,  $t_{peak}$  is nearly invariant with  $d$ , with only slightly shorter  $t_{peak}$  at larger orifice diameters (e.g.,  $0.63 \leq t_{peak} \leq 0.67 \text{ ms}$  for  $\Phi = 1.0$  and  $1.99 \leq t_{peak} \leq 2.13 \text{ ms}$  for  $\Phi = 0.5$ ). Similar results are obtained at all  $\Phi$  for both hydrogen and propane, indicating that the orifice diameter has minimal effect on the combustion process and the flame propagation within the chamber. However, similar to excessively lean mixture ratios, orifice diameters that are too large result in chamber pressures that are too low to stop the flow of reactants into the chamber, consequently resulting in a standing flame in the combustor. The present system does not operate at  $d > 2.50 \text{ mm}$  for hydrogen mixtures (within the set of parametric orifices available, the next size tested was  $d = 3.18 \text{ mm}$ ) and at  $d > 1.78 \text{ mm}$  for propane mixtures.

The variation of the peak pressure with both orifice diameter and mixture ratio is plotted in a 3-D map to outline the actuator operating space for  $Q = 10 \text{ cc/s}$  (Figures 30a and b

for hydrogen and propane, respectively). These maps show that the trends for peak pressure shown in association with Figures 28 and 29 hold across a broad range of values, with both lower  $\Phi$  and larger  $d$  values yielding smaller peak pressures. It is noteworthy that for propane the peak pressure values are more sensitive to increasing orifice diameter than for hydrogen (e.g., for  $\Phi = 1.0$  with  $d$  increasing from 0.79 to 1.78 mm, peak pressure decreases from 5.09 to 3.73 for hydrogen and from 2.95 to 1.13 for propane). This is likely the result of the lower flame speeds (i.e., longer  $t_{peak}$ ) for propane which allow longer periods for the gas to vent as the pressure rise takes place. Sufficient combinations of low mixture ratio and large orifice diameter are prone to the same formation of standing flame in the chamber observed previously. For example, for hydrogen and  $d = 2.21$  mm, the actuator does not function well with  $\Phi < 0.7$ , although with  $d = 1.78$  mm, operation with  $\Phi$  as low as 0.5 can be achieved.

The trend of the peak pressure for hydrogen is specifically noteworthy because the variation with  $\Phi$  is very consistent for all values of  $d$  and is similar to the corresponding curve for the ideal constant volume pressure, as shown in Figure 31. Each value for  $d$  has an offset relative to the CV pressure values, which increases slightly as the mixture ratio is decreased (presumably because at lower flame speeds there is more venting through the orifice before the  $t_{peak}$  is reached). For the lowest diameter tested ( $d = 0.79$  mm), the difference between ideal and measured peaks grows from 3.15 (at  $\Phi = 1.0$ ) to 3.59 (at  $\Phi = 0.4$ ), and at the largest diameter ( $d = 2.50$  mm), this difference increases from 5.42 (at  $\Phi = 1.0$ ) to 5.59 (at  $\Phi = 0.6$ , which is the lowest mixture at which a detectible pressure rise is measured for this orifice diameter). The difference between the measured

and ideal pressure levels is generally linear with the diameter for each mixture ratio tested, and, if extrapolated along the same line, yields a peak pressure of 6.17 at  $\Phi=1.0$  for a closed chamber, or a difference of 2.07 relative to the ideal CV value. This difference may be accounted for by losses owing to heat transfer to the walls, flow into the upstream inlet passages, or loss of reactants through the exhaust orifice before they are burned. Similar trends are observed for propane as compared to its CV combustion properties, but with substantially larger differences in pressure owing to the lower flame speeds and consequently higher losses due to flow through the orifice.

As alluded to earlier, chamber pressure is a significant measure of the utility of the actuator for flow control applications because it is directly related to the instantaneous velocity (and momentum flux) of the control jet emanating from the orifice. A simple control volume analysis of the combustor can be used to calculate the idealized, instantaneous jet momentum flux (or thrust,  $F$ ) from the pressure curve. Assuming a quasi-steady and constant-density flow at a given instant, uniform flow at the orifice, that the mass of the combustor itself is substantially greater than the mass of gas within the combustor (i.e., the rate of change of momentum inside the control volume is negligible), and neglecting the momentum of any flow to or from the inlet, the momentum equation reduces to

$$F = \rho_e V_e^2 A_e + (P_e - P_{atm}) A_e$$

where the subscript  $e$  denotes conditions at the orifice. Substituting in the ideal gas equation and equations for isentropic flow at the orifice, this expression yields:

$$F = \left( \frac{P_e}{RT_e} \right) \left( M_e \sqrt{\gamma RT_e} \right)^2 A_e + (P_e - P_{atm}) A_e$$

$$F = \left[ P_e M_e^2 \gamma + (P_e - P_{atm}) \right] A_e$$

In the above equation above, the orifice area is fixed for a given combustor configuration and the pressure and Mach number at the exit plane are both functions of the combustor pressure (which can be calculated using the appropriate equations depending upon whether the orifice flow is choked). Only the specific heat ratio,  $\gamma$ , remains as an explicit function of temperature, however the variation of  $\gamma$  with temperature is comparatively small (e.g., for air with  $300 \leq T \leq 1000$  K,  $\gamma$  ranges from 1.40 to 1.34 – Cengel and Boles, 1989). Therefore, a reasonable approximation of the jet momentum during the cycle may be calculated directly from the pressure data without specific knowledge of the dynamic temperature of the jet (which is difficult to measure as the flow is high velocity, preventing the practical use of cold-wire temperature sensors, and the chemical composition of the jet may vary, making optical scattering temperature measurements problematic as well). Thus, the resulting thrust curve has basically the same shape as the pressure during the cycle. Because the flow in the orifice is assumed to be isentropic and inviscid, the calculated thrust will be an overestimate, but it is nonetheless useful for comparison between cases. This estimate for thrust is compared to measured force from the force sensor (with simultaneous data acquisition of both the pressure and force



signals) in Figure 32 with  $d = 1.30$  mm for two cases (hydrogen,  $\Phi = 0.7$  and propane,  $\Phi = 1.0$ ). (As noted above, substantial ringing occurs in the force sensor signal at roughly 2-3 kHz with the amplitude increasing as the thrust from the actuator increases. The two selected cases are the highest values for  $\Phi$  at which the thrust curve is largely discernable from the ringing.) The shape of the measured and calculated curves for  $F$  is very similar in shape over the combustion cycles and the peak values occur nearly simultaneously. However, the measured thrust is approximately 60-65% of the calculated value. This difference is not unexpected or unreasonable given that the flow through the orifice in the experiments is not optimized and is probably not isentropic. (There is some disagreement between the curves after the pulse is over and the refill process begins, with the measured thrust becomes slightly negative before returning to zero which may be a result of a dynamic overshoot in the force sensor) Overall, the idealized calculation of  $F$  appears to provide a reasonable order-of-magnitude estimate of thrust values, particularly for comparison between different actuator test cases.

With  $F$  calculated from the pressure curve, the actuator performance may be assessed on the basis of jet thrust (which is of direct interest in flow control applications). While the combustor pressure can be increased continually by decreasing the orifice diameter (to the limit where there no jet flow and the pressure in the chamber decreases by heat transfer to the walls only), the thrust calculation scales directly with the orifice area and therefore represents a trade-off between increasing the pressure and decreasing the area. The calculated peak thrust over the cycle based upon the peak pressure data of Figure 30 are shown as 3-D surface plots in Figure 33. In similar fashion to pressure,  $F$  increases

continuously with  $\Phi$  for all values of  $d$  over the range tested. However, the variation of thrust with orifice diameter runs is opposite to the variation of pressure (at least for small orifice sizes.) Here, while a decrease in orifice size yields an increase in peak pressure, there is a substantial decrease in peak thrust. As  $d$  is increased, two regimes are apparent. Where the peak combustor pressure is generally low (i.e., less than 2 atmospheres, as is the case for the entire operating regime with propane and for  $\Phi \leq 0.7$  with hydrogen), an optimum  $F$  value is found at intermediate values of  $d$  (typically around 1.30 mm). For  $d > 1.30$  mm,  $F$  again decreases and even drops below the values for the smallest orifice diameter tested. As the mixture ratio and subsequent pressure levels are increased (particularly for hydrogen), this optimum shifts towards larger orifice diameters. For higher pressure cases (hydrogen with  $\Phi \geq 0.8$ ), no optimum value is found within the operating range and the peak thrust increases monotonically with  $d$ . It is likely that an optimum does exist in these cases as well for larger orifice sizes if the actuator can be operated in these conditions without degrading to the standing flame behavior noted earlier. Over the entire range of  $\Phi$  and  $d$ , peak thrust levels as high as 1036 mN for hydrogen and 152 mN for propane are calculated for  $Q = 10$  cc/s.

### III.3.c Chamber Aspect Ratio

Changes in combustor aspect ratio yield two major changes in the actuator performance. First, changes to the surface area of the combustor relative to its volume affect the heat transfer losses to the chamber walls. (The surface area of a cylindrical chamber of a fixed volume reaches a minimum at  $H/D = 1$ , and increases with changes in aspect ratio in

either direction.) Second, alteration of the chamber shape affects the flame propagation pattern and therefore the rate of heat release. For aspect ratios near unity, the flame propagation through the bulk of the chamber is primarily spherical with a heat release rate that scales with the time rate of change of the spherically expanding volume. For  $H/D$  substantially less than 1, the chamber has the appearance of a flat disc and the flame propagation is primarily radial (2-D) towards the outer walls (the flame reaches the upper and lower surfaces shortly after ignition). With  $H/D$  substantially greater than 1, the chamber becomes a long tube and the flame fronts propagate axially (1-D) towards the upper and lower ends of the chamber. The time rate of change these of idealized burned volumes may be easily calculated (assuming the flame front at any given time is a distance  $S_L \cdot t$  from the spark gap) and the heat release rate should scale with these values:

Spherical flame front ( $H/D \approx 1$ )	$\frac{\partial V}{\partial t} = \frac{4}{3} \pi (S_L)^3 t^2$
Radial flame front ( $H/D \ll 1$ )	$\frac{\partial V}{\partial t} = \pi H (S_L)^2 t$
Dual linear flame fronts ( $H/D \gg 1$ )	$\frac{\partial V}{\partial t} = \frac{\pi}{2} D^2 S_L$

The actual flame propagation within a given chamber is of course necessarily more complex (propagating spherically from the spark gap and then transitioning as necessary) and the actual propagation speed of the flame front may be time-dependent. However, these simplifications provide a useful hierarchy of anticipated results, with faster burn times for chambers with unity aspect ratios, followed by chambers in which  $H/D < 1$ , and finally chambers in which  $H/D > 1$ .

Aspect ratio effects are investigated in four chambers having  $H/D = 0.45, 0.83, 2.33$ , and  $3.59$  (in addition to the baseline configuration,  $H/D = 1.27$ ) with chamber volume held at  $1 \text{ cc}$  (the chamber properties are detailed in Table 3 on the following page). The variation of surface area between chambers is rather small with a maximum of  $6.48 \text{ cm}^2$  and a minimum of  $5.49 \text{ cm}^2$  (18% difference) over the range tested. While the heat transfer is expected to scale with the surface area of the chamber, the difference in surface potentially leads to an underestimate of the change in heat transfer losses between chambers. In chambers with high and low  $H/D$ , the flame impacts one or more of the chamber walls earlier in the combustion process than in a unity aspect ratio chamber, thus exposing hot combustion gases to the chamber walls for a longer time and further increasing the heat transfer. Also, the mean refill flow velocities listed in the Table 3 are solely for the fluid motion downstream within the chamber (i.e., along the inlet/exhaust axis). While this value increases continuously as the aspect ratio increases (and cross-sectional area decreases), chambers with very low aspect ratios may also develop considerable motions in the radial direction as inlet gas at the periphery of the chamber moves towards the single exhaust point on the centerline. This initial flow is counter to the direction of the flame propagation and may affect the time it takes for the flame to reach the outer walls.

**Table 3.** Properties for combustion chambers with varying aspect ratio holding  $V = 1$  cc.

Aspect Ratio ( $H/D$ )	Diameter ( $D$ , mm)	Height ( $H$ , mm)	Surface Area ( $\text{cm}^2$ )	Mean downstream velocity @ cross-section (m/s); $Q = 10\text{cc/s}$
0.45	14.2	6.4	6.02	0.063
0.82	11.5	9.4	5.49	0.096
1.27	10.0	12.7	5.57	0.127
2.33	8.2	19.1	5.98	0.189
3.59	7.1	25.4	6.48	0.253

Several pressure traces for  $H/D = 0.45$ , 1.27, and 3.59 are shown in Figures 34a, b, and c, respectively for variation in mixture ratio at  $d = 1.30$  mm. The data for  $H/D = 1.27$  is the same as that in Figure 28a and is presented here on an enlarged scale comparable to the other data sets. Perhaps the most dramatic difference compared to previous results is the performance of the combustor for which  $H/D = 3.59$  case (Figure 34c), with substantially reduced peak pressures across the full range of mixture ratios (e.g., 3.05 at  $\Phi = 1.0$  versus 4.41 at  $H/D = 1.27$ ). There is also a change in the shape of the pressure curve with a distinct decrease in the rate of pressure rise for  $\Phi \geq 0.7$  before the beginning of the pressure decay. Similar results were observed by Faulkner, et al (2000) for rectangular high-aspect ratio combustion chambers, with inflection points in the pressure curve corresponding directly to the time at which the flame front extinguishes against one or more of the chamber walls. In the case of the combustion actuator with  $H/D > 1$ , this inflection results from the transition from spherical to linear flame propagation with corresponding reductions in rate of heat release as outline above. The reduced rate of pressure rise is still greater than the losses (due to flow through the orifice and heat transfer) for  $\Phi \geq 0.8$  with an additional time delay between the inflection point and  $t_{peak}$

before the pressure decay as in previous results. For  $\Phi = 0.7$ , the pressure level in the chamber is nominally invariant after the inflection point (approximately 2.1 over roughly  $0.9 < t < 1.4$  ms) before decaying to atmospheric, suggesting the rates of heat release rate and pressure loss are essentially in equilibrium until the flame fronts reach the upper and lower ends of the chamber. With mixture ratios of 0.6 and 0.5,  $t_{peak}$  corresponds to the initial inflection point in the curve, with an almost linear decay to atmospheric pressure in contrast to the typically exponential decay seen after  $t_{peak}$  in most cases. This is due to substantial heat release from ongoing combustion after  $t_{peak}$  in these cases but at a rate less than the combined loss rate.

The results for  $H/D = 0.45$  (Figure 34a) are reasonably similar to the baseline ( $H/D = 1.27$ ) combustor, with comparable peak pressures. Although an inflection point similar to that of the high aspect ratio combustor may be expected, the decrease in heat release rate during transition from spherical to radial propagation is substantially smaller than for transition from spherical to linear propagation and the resultant change in the pressure curve is only observed to a small degree at high mixture ratios and not at all for low ratios ( $\Phi \leq 0.7$ ). The disagreement between the baseline and the low aspect ratio combustor becomes more apparent at lower mixture ratios, with notably lower peak pressures and higher  $t_{peak}$ . For low mixture ratios, the pressure curve features a slow rise followed by a quick decay to nominally atmospheric levels (at  $\Phi = 0.6$ ,  $t_{peak} = 2.15$  ms with the pulse duration of roughly 3.25 ms) whereas the opposite pattern (i.e., peak pressure reached quickly with a long decay) is observed for the aspect ratio  $H/D = 3.59$  chamber (at  $\Phi = 0.6$ ,  $t_{peak} = 1.22$  ms with the pulse completed in roughly 3.5 ms).

The differences between cases at the same mixture ratio are seen Figures 35a and b ( $\Phi = 1.0$  and  $0.7$ , respectively) which includes data for  $H/D = 0.45, 0.82, 1.27, 2.33$ , and  $3.59$ . The results for  $H/D = 0.82$  and  $1.27$  are very similar for all mixture ratios, with pressure traces that have nearly identical shapes (both aspect ratios allow primarily spherical flame propagation). Also as expected,  $H/D = 2.33$  and  $3.59$  yield consistently lower peak pressures and a pressure curve with an inflection point (which is less pronounced but still apparent for  $H/D = 2.33$ ). Perhaps the most unexpected result here is for  $H/D=0.45$ . At  $\Phi = 1.0$ , in spite of its low aspect ratio and notably longer pressure rise time ( $t_{peak} = 0.73$  ms compared with  $t_{peak} = 0.66$  ms for  $H/D = 1.27$ ), this aspect ratio has the highest peak pressure among those tested ( $4.60$ ). This is almost certainly the result of more complete burning of the reactants in the very low aspect ratio combustor. The pressure rise within the chamber begins immediately at spark ignition with the gas that is in proximity to the orifice (either products or reactants) ejected as a result. In low aspect ratios, the distance of the spark gap from the exhaust orifice (i.e., one half of the chamber height) is greatly reduced and the flame front reaches the exhaust orifice early in the cycle effectively ensuring that no additional unburned gas is ejected. In contrast, at high aspect ratios, the flame front takes substantially more time to reach the exhaust orifice and substantial quantities of unburned gas may be lost. This is probably also part of the reason that the pressure levels are significantly lower for all mixture ratios with  $H/D = 2.33$  and  $3.59$  than for other aspect ratios. For  $\Phi = 0.7$ , the slower flame propagation speed apparently eliminates part of this advantage for  $H/D = 0.45$ , and the peak pressure is again below the peak at  $H/D = 1.27$  ( $3.01$  with  $t_{peak} = 1.44$  ms compared to  $3.21$  at  $t_{peak}$

= 1.11 ms), but the shorter time to reach this value for low aspect ratios still suggests an advantage in terms of the quantity of burned reactant.

### III.3.d Chamber Volume

The volume of the combustion chamber is another key system parameter. As the chamber volume is decreased,  $t_{pulse}$  is expected to decrease (holding other factors which effect the flame speed constant), and  $t_{refill}$  is also likely to decrease as less mixture is required to refill the chamber. The result is an increase in the potential range of actuator operating frequencies coupled with increased packing density of individual actuators over a given surface area for flow control. However, as chamber volume decreases the volume to surface area ratio also decreases substantially, and heat transfer and other wall quenching effects are expected to increase (down to the quenching limits which are 0.64 mm for hydrogen and 2.0 mm for propane below which the actuator should not be able to function). Five chambers having the baseline aspect ratio ( $H/D = 1.27$ ) and volumes of 0.25, 0.50, 1.00, 1.50, and 2.00 cc are tested to investigate the primary effects of volume change on the system, with each configuration detailed in Table 4 (on the following page). At this point, it is useful to refer to an idealized frequency at which the actuator would be operated, assuming perfect exhaust gas displacement and igniting the mixture each time that the chamber is completely refilled. This parameter may then be calculated from the chamber volume and mixture flow rate ( $f_{ideal} \equiv Q/V$ ). The tests are performed for  $f_{ideal} = 10$  Hz with a different inlet orifice array for each volume where the diameter of



the each inlet orifice is 350  $\mu\text{m}$ , but the number of orifices is chosen to scale the total inlet orifice area with the chamber volume. Thus the velocity (and  $Re$ ) of the flow at the inlet is held nominally invariant and the mixture flow conditions at the inlet are approximately the same for all volumes. (Table 4 shows that there is an unavoidable disparity in flow velocities at other regions that is discussed further in the §III.3.e. However, for the baseline  $f_{ideal} = 10$  Hz case, these values are all comparatively low and should have minimal impact on the flow quality and flame propagation within the chamber.)

**Table 4.** Properties for combustion chambers with varying chamber volume holding  $H/D = 1.27$ .

$V$ (cc)	Geometric Properties				Mixture Flow Properties ( $f_{ideal} = 10$ Hz; $d = 1.30$ mm)	
	$D$ (cm)	Surface Area ( $\text{cm}^2$ )	Volume/ Surface Area (cm)	Inlet Orifices (#; respective diameter as % of $D$ )	Mean velocity @ cross- section (m/s)	Mean velocity @ exhaust (m/s)
0.25	0.63	2.21	0.11	(1,6; 0,50)	0.080	1.88
0.50	0.79	3.51	0.14	(1,5,8; 0,33,67)	0.101	3.77
1.00	1.00	5.57	0.18	(1,4,8,16; 0,25,50,75)	0.127	7.53
1.50	1.15	7.29	0.21	(1,4,8,12,19; 0,20,40,60,80)	0.146	11.30
2.00	1.26	8.84	0.23	(1,6,10,16,25; 0,20,40,60,80)	0.160	15.07

Some results for various combustor volume are shown in Figures 36a and b for hydrogen mixture ratios of 1.0 and 0.7, respectively (with  $d = 1.30$  mm). The peak pressure during the cycle increases with the volume (for  $\Phi = 1.0$ , from 2.68 at  $V = 0.25$  cc up to 4.97 at  $V$

= 2.00 cc) as the chemical energy released increases while the opening for exhaust venting remains unchanged. There is a large percentage increase in the peak pressure between 0.25 cc and 0.50 cc (for  $\Phi = 1.0$ , 2.68 and 3.51, respectively), with somewhat smaller increases for progressively higher volumes. The rate at which the pressure initially increases is noticeably faster for smaller volumes. This is expected because the initial flame propagation speed should be invariant with volume, and the volume of the initially burned region within the chamber is a larger percentage of the total for small volume chambers (thus yielding higher mean pressure within the chamber). Furthermore,  $t_{peak}$  is smaller for lower volumes since it takes less time for the flame front to propagate to the chamber walls and it scales nearly perfectly with  $D$  for  $\Phi = 1.0$  (e.g., from  $V = 0.25$  to 2.00 cc, the chamber diameter doubles and  $t_{peak} = 0.41$  ms at 0.25 cc and 0.82 ms at 2.00 cc). The scaling between  $t_{peak}$  and  $D$  does not hold as well at lower mixture ratios (e.g., for  $\Phi = 0.7$ ,  $t_{peak} = 0.57$  and 1.28 ms at  $V = 0.25$  and 2.00 cc, respectively), with relatively faster flame speeds at lower chamber volumes, possibly indicating that the flame propagation speed is time-dependent.

For a given chamber volume, changes in mixture ratio alter the chamber pressure in similar fashion to what is shown in §III.3.a. The peak pressures varying  $\Phi$  are summarized in Figure 37 for all values of  $V$  for  $d = 1.30$  mm. These results are analogous to those displayed for variation in  $d$  in Figure 31, with a characteristic differential between the peak pressure and ideal CV pressure observed for each volume, and the difference increasing slightly as  $\Phi$  is decreased. The dimensions of the present test hardware prevent tests of chambers that are larger than 2 cc, however, in the high

volume limit for a fixed exhaust orifice diameter, the results are expected to approach the CV pressure levels (assuming that a transition from deflagration to detonation does not occur). This is because the exhaust flow through the orifice represents a smaller and smaller fraction of the total mass of gas within the chamber and wall losses become less important at high volume. However, the results show generally diminishing returns in the increase in the peak pressure when the volume is above 1 cc, and the use of excessively large combustion chambers (likely required to approach the CV limits) would mandate substantial reduction in the operating frequency to accommodate the increased pulse and refill times. Therefore, for flow control applications, it appears that there is little practical advantage to an increase in chamber volume beyond the current range.

### III.3.e Mixture Flow Rate

The operation of the combustion actuator at higher frequencies requires more frequent refill of the combustion chamber and higher overall mixture flow rates,  $Q$ . As the flow rate is increased, the refill gas speed within the chamber also increases along with secondary flow that may support turbulent fluctuations in part or all of the combustion chamber. For low actuation frequency (i.e.,  $t_{pulse}/\tau \approx 0$ ), the mean refill gas velocities for several mixture flow rates are calculated from conservation of mass at the inlet orifice grid, at the cross-section of the chamber, and at the exhaust orifice (for  $d = 1.3$  mm) and listed in Table 5 (on the following page). (These calculations assume that the flow is uniform at each cross-section and that the chamber pressure during refill is atmospheric.)

At these flow conditions, the typical velocities at the chamber inlet and exhaust are one to two orders of magnitude higher than the laminar flame speeds (2.10 m/s and 0.44 m/s for stoichiometric hydrogen and propane respectively; see Table 1 for other mixture ratios), and the speed of the bulk flow inside the chamber is of the same order as the laminar flame speeds. Although the flow speed at each combustor section changes substantially during the combustion process (increasing at the exhaust orifice and within the combustor and decreasing and changing direction at the inlet orifices), these values indicate that the mixture flow rate can have a substantial effect on the initial flame propagation in terms of its direction and net velocity.

**Table 5.** Mean refill flow properties varying flow rate for a 1 cc,  $H/D = 1.27$  chamber.

$Q$ (cc/s)	Inlet orifice grid		Chamber cross-section		Exhaust orifice ( $d=1.30\text{mm}$ )	
	Velocity (m/s)	$Re$	Velocity (m/s)	$Re$	Velocity (m/s)	$Re$
10	3.58	87	0.13	88	7.59	677
30	10.75	260	0.38	263	22.76	2033
50	17.92	432	0.64	439	37.93	3389
75	26.88	649	0.95	659	56.90	5083
100	35.84	865	1.27	878	75.88	6778

Table 5 also includes the Reynolds number of the flow at each of the sections, using properties for pure air. (Given the small volume fraction of propane in stoichiometric to lean mixtures (which is less than 4%), the calculated values provide a good estimate for all propane mixtures. The actual Reynolds numbers for stoichiometric to lean hydrogen mixtures (where the volume fraction of hydrogen is up to 29.6%) are somewhat lower

since the kinematic viscosity of hydrogen is roughly 7 times greater than that of air at STP.) Even though the characteristic Reynolds number of the flow in the chamber cross-section is relatively low ( $< 1000$  for all flow rates), the array of inlet orifices act as axisymmetric free jets which vent into the chamber, and it is anticipated that these jets can form small-scale secondary motions that promote turbulence within the chamber. Also, the ceramic insulators that comprise the spark gap act as an obstruction in the flow which may further increase turbulence. Although the Reynolds number at the exhaust orifice is relatively high, the velocity and local Reynolds number decrease inside the chamber with increasing distance from the orifice. This region near the exhaust orifice is expected to be of minimal importance to the overall flame propagation because the flame front in close proximity to the orifice follows the high velocity flow out of the chamber (and is potentially quenched as it passes through the orifice).

An increase in the overall burning rate (whether as a result of increased small scale turbulence or larger scale secondary flow patterns within the chamber) should yield faster pressure rise within the combustion chamber, higher peak pressure, and pulses of shorter duration. Two sample cases are illustrated in Figure 38 varying  $Q$  with  $d = 1.30$  mm for hydrogen ( $\Phi = 0.6$ ) and propane ( $\Phi = 1.0$ ). As  $Q$  increases, both fuels exhibit the expected behavior with trends that are similar to the results for variation in stoichiometry at low flow rates (where the pressure curve also changes as a result of changes in the flame speed). For hydrogen, with  $Q$  increasing from 10 to 100 cc/s, the peak pressure rises from  $P_r = 2.61$  to 4.11, with  $t_{peak}$  decreasing from 1.45 to 0.71 ms. Similarly for propane, the peak pressure rises from  $P_r = 1.68$  to 2.79, with  $t_{peak}$  decreasing from 3.46 to

2.26 ms over the range of  $Q$  from 10 to 75 cc/s. (Note that limitations on the air flowmeter ranges available prevented testing of hydrogen mixture flow rates greater than 100 cc/s and propane mixtures flow rates greater than 75 cc/s, although the trends reported are expected to continue for further increases in  $Q$ .)

The specific effects of the flow rate on the flame propagation are shown in Figures 39 through 42, which are sequences of flame photography images that are captured using a cubical 1 cc combustion chamber ( $d = 1.30$  mm) with stoichiometric propane/air mixture at  $Q = 10, 30, 50$ , and  $75$  cc/s, respectively. (Flame photography for hydrogen is not included here because light emission from hydrogen flames is almost entirely in the UV ( $\sim 310$  nm) and therefore can not be visualized with the available CCD camera and optics.) All of the images are normalized to the same light intensity levels so that the brightness of the flame may be taken as a qualitative measure of the amount of reactants burning at a given time. The images are oriented such that the inlets and exhaust are at the bottom and top of each image, respectively. In Figure 39 ( $Q = 10$  cc/s), the flame front is laminar throughout the cycle and the flame propagation is nearly uniform in all directions. There is a slight bias in the flame propagation towards the exhaust orifice, which is consistent with the relative flow and flame speeds (mean flow speed of 10 cm/s in the cross-section of the cubical chamber compared to the laminar flame speed of 44 cm/s or  $U/S_L = 0.23$ ). The flame front reaches all four walls of the chamber by  $t = 3.5$  ms (Figure 39g) and, as noted in §III.3.b, this corresponds to a net flame propagation speed which exceeds  $S_L$  (143 versus 44 cm/s) as a result of expansion of the hot gas pocket behind the flame front. Weak flames at the corners of the chamber are visible until  $t =$

6.0 ms (Figure 39l). Thus, the point at which the flame front reaches the chamber walls and the total flame duration correspond closely to  $t_{peak}$  and  $t_{pulse}$  measured in the baseline cylindrical test chamber with equivalent  $\Phi$ ,  $d$ , and  $Q$  (see Figure 38b).

For  $Q = 30$  cc/s (Figure 40), the calculated time-averaged velocity is 30 cm/s which approaches the laminar flame speed (i.e.,  $U/S_L = 0.68$ ). This is evident in images 40a through 40d ( $t = 0.25$  to 1.0 ms), as the upstream travel of the flame front (i.e., towards the inlets) is far smaller than the downstream travel which, by  $t = 1.0$  ms, reaches the upper surface of the chamber. (The upstream distance of the flame propagation is actually less than what might be expected from the ratio  $U/S_L$  indicating that either the flame speeds in these experiments are somewhat lower than the standard tabulated values in the literature or that the local flow velocity at the spark gap is larger than the calculated average value – possibly due to blockage of the flow by the spark plug.) Over this period, the flame front which propagates towards the side walls of the chamber is wrinkled but mostly continuous. For  $t > 1.0$  ms (Figures 40e-k), the flame front that previously stalled at the spark location begins to move upstream, indicating that chamber pressure is sufficiently high to stop the flow of reactants at the inlet. By  $t = 2.5$  ms (Figure 40g), the flame fills the chamber with substantial flame wrinkling and, by  $t = 3.0$  ms (Figure 40h), the flame in the upper region of the chamber begins to extinguish, while an active reaction region continues in the lower part of the chamber (that was reached later by the flame front). Finally, the combustion process ends with weak burning that is visible at the walls and corners of the chamber and is effectively complete by  $t = 4.5$  ms (Figure 40k).

For flow rates of  $Q = 50$  cc/s and  $75$  cc/s (Figures 41 and 42, respectively), the flame propagation patterns are similar to that which is observed for  $30$  cc/s. The flame is initially driven downstream by the gas velocities within the chamber, which for these flow rates are above the laminar flame speed ( $U/S_L = 1.14$  and  $1.70$ , respectively). Large gas speeds are also indicated for both cases by the substantial bowing of the spark upward (see Figures 41b and 42b) as the initially ionized gas which forms the discharge path follows the bulk flow. In both cases, the flame front is substantially wrinkled, and the flame initially moves towards the upper corners of the chamber and then turns and propagate towards the bottom of the chamber as the pressure rises and flow at the inlet stops (and reverses). The combustion process in both cases completes with weak burning along the lower boundary of the chamber and is effectively over by  $t = 4.0$  ms and  $3.5$  ms, respectively. The peak light intensity of the flame increases noticeably with  $Q$  (see Figures 41f and 42f for comparison), indicating that the rate at which the reactants are burning increases as the flame front is stretched by the gas flow which is carrying it. Note that the pressure traces of Figure 38b roughly match the flame photography for all flow rates, comparing the duration of the pressure pulses to the time period over which flames are observed. While images for hydrogen are not available, the trends for the effects of  $Q$  on the flame propagation should be similar, although the effects of the gas velocity and increased turbulence are expected to be less pronounced since  $S_L$  is substantially higher for hydrogen than propane at most mixture ratios.



The properties of turbulent premixed combustion processes have been classified typically by relating the characteristic flow and chemical reaction times. Borghi (1985) mapped turbulent combustion regimes comparing the length and velocity scale ratios (i.e.,  $v'_{rms}/S_L$  and  $l_0/\delta_L$ , where  $l_0$  is the integral turbulence scale,  $\delta_L$  is the laminar flame thickness, and  $v'_{rms}$  is the rms fluctuating velocity). These relations are often combined in the form of the Damkohler number [ $Da \equiv (l_0/\delta_L)(S_L/v'_{rms})$ ], which Williams (1985) used in combination with the turbulent Reynolds number ( $Re_t \equiv v'_{rms}l_0/\nu$ ) to create a different diagram representing similar regimes. These combustion regimes range in the limits from fast chemistry compared to the fluid mixing rates ( $Da \gg 1$ ) to slow reaction rates compared to the fluid mixing ( $Da \ll 1$ ) and are characterized as the wrinkled laminar flame and distributed (or well-stirred) regimes, respectively, describing the effects of the turbulence on the reaction zone. The direct flame photography technique used in the present experiments does not allow visualization of the instantaneous planar shape of the flame front/reaction zone since the CCD picks up light emission from the entire depth of the combustion chamber. However, the flame photography suggests that the flame propagation transitions from laminar propagation to the wrinkled laminar flame regime as  $Q$  is increased, with indeterminate properties at large flow rates.

The effect of different mixture ratios at increased flow rates (and therefore increased turbulence intensities) is shown in Figure 43, for hydrogen with  $d = 1.09$  mm. It is noted that the relative effect on the burn rate and pressure due to the increase in  $Q$  is larger at leaner mixture ratios. For example, for  $\Phi = 0.6$  over the range  $10 \leq Q \leq 100$  cc/s, the peak pressure increases from  $P_r = 2.99$  to 4.74 with a corresponding decrease in  $t_{peak}$  from

1.44 to 0.67 ms. Over the same range of flow rates for  $\Phi = 0.4$ , the peak pressure increases from 1.43 to 3.12 with a corresponding decrease in  $t_{peak}$  from 2.94 to 1.14 ms. As  $Q$  is increased, the values for  $t_{peak}$  across all mixture ratios become closer and the pressure curves collapse and exhibit similar pulse durations and pressure decays from the peak level. These trends are similar to those found in the literature for turbulent premixed combustion in the wrinkled laminar flame regime. Peters (1999) noted that much of the experimental data on turbulent flame speeds ( $S_T$ ) can be reduced to a relationship of the form

$$\frac{S_T}{S_L} = 1 + C \left( \frac{v'_{rms}}{S_L} \right)^n$$

where the values of constants  $C$  and  $n$  vary somewhat, but  $n$  is typically around 0.7. It is easily shown that for a constant value of  $v'_{rms}$ , the percentage increase in flame speed (represented by  $S_T/S_L$ ) will be greater for lower values of  $S_L$ . Thus it is expected that leaner mixture ratios are more sensitive to turbulent fluctuations. Although direct comparison of the present results to previous experimental turbulent flame speed data is problematic (since the earlier experiments were typically designed to avoid the mean flow speeds within the combustor which are inherent to the combustion actuator), the trends are still consistent.

It is noted from Figure 38 and Figures 43d and e that a slight increase in initial chamber pressure occurs for  $Q \geq 75$  cc/s, where the increase in Figure 43 ( $d = 1.09$  mm) is greater

than in Figure 38 ( $d = 1.30$  mm). As  $Q$  is increased, the pressure in the chamber increases owing to pressure drop at the exhaust orifice and therefore there is a slight change in the initial conditions of the combustion process. Table 6 (on the following page) shows the initial pressures for the given flow rate at a specified orifice diameter, using compressible flow equations and assuming isentropic and inviscid flow through the orifice. For  $d > 1.50$  mm, the pressure rise is essentially negligible across the full range of flow rates ( $Q \leq 100$  cc/s), and only pressures for smaller diameters are presented in the Table 6. At the smallest orifice diameter tested ( $d = 0.79$  mm), there is a significant initial pressurization of the combustion chamber at high flow rates ( $P_r = 1.276$  at  $Q = 100$  cc/s). These calculated ideal values agree well with the pressure level recorded in the combustion chamber at ignition, although the measured values are typically slightly higher value (e.g., from the data of Figure 43e, the initial pressure is  $P_r = 1.09$  compared to 1.07 from the table). Although the prepressurization of the chamber is typically small, it can have some impact on the combustion properties. For example, the ideal constant volume pressure scales directly with initial pressure (i.e., a 10% increase in initial pressure yields almost a 10% increase in CV pressure). It is expected from the data presented in Lewis and Von Elbe (1987) that the pressure effects on the flame speed and quenching distance are essentially negligible for the slight pressure increases involved.

**Table 6.** Combustion chamber pressure required to maintain desired steady flowrate ( $Q$ ) through given orifice diameter ( $d$ ).

	$P_r$				
$Q$ (cc/s)	$d = 0.79$ mm	$d = 0.89$ mm	$d = 1.09$ mm	$d = 1.30$ mm	$d = 1.50$ mm
10	1.003	1.002	1.001	1.000	1.000
30	1.023	1.014	1.006	1.003	1.002
50	1.064	1.040	1.017	1.009	1.005
75	1.149	1.091	1.039	1.019	1.011
100	1.276	1.165	1.070	1.034	1.019

Similar to the results for  $Q = 10$  cc/s (reported in §III.3.b), parametric maps of the operating space are created for each flow rate varying both  $\Phi$  and  $d$ . These are shown as contour plots of peak pressure in Figures 44 and 45 for each value of  $Q$  (including  $Q = 10$  cc/s, previously shown as surface plots in Figure 29) for hydrogen and propane, respectively. The contours are created via linear interpolation between experimental data points for variation in both  $\Phi$  and  $d$  and are plotted in pressure increments of 0.2. Within the operating space for independent combustion pulses (discussed below), an increase in  $Q$  results in higher peak pressures at any given combination of  $\Phi$  and  $d$ . The contours over the operating space for each fuel are generally consistent in shape and spacing between different flow rates. The only exception to this occurs for both hydrogen and propane when  $Q \geq 75$  cc/s and  $d \leq 0.89$  mm, where the peak pressures increase substantially (for both fuels) as a result of the increase in initial pressure for the combustion process. For all flow rates, propane continues to show greater sensitivity to chamber diameter than hydrogen (again as a result of lower flame speeds and subsequent burn rates).

For hydrogen combustion, the operating range over which the actuator functions properly is substantially affected by  $Q$ . This may be attributed to the increased supply pressure (upstream of the fluidic element) required to maintain higher flow rates. As the supply pressure increases, it is increasingly likely that flow of reactants into the chamber will begin before the flame is entirely extinguished, resulting in a standing flame within the chamber (described previously in §III.3.b). Stopping the inlet flow at higher pressures and velocities (and creating an exhaust pocket within the fluidic element) requires increasingly high chamber pressure levels and thus operation at large  $d$  is problematic. The extent of this reignition problem also depends on how flammable the incoming reactants are and whether the weak flames at the edges of the chamber are sufficient to ignite any incoming mixture. Thus it is possible to have effective actuator operation at leaner, less volatile mixture ratios at conditions where rich mixtures result in reignition. These factors are apparent in the trends for hydrogen, where the operating limits move progressively towards leaner mixtures and smaller orifice diameters as  $Q$  increases. By contrast, the propane operating space for the most part does not change either in terms of  $\Phi$  or  $d$  as the flow rate is increased. This is presumably because propane mixtures are substantially less flammable than hydrogen mixtures (see §III.3.g for an indication of this through ignition energy). In these cases, it is likely that reactants enter the combustion chamber before the combustion process is complete but are not stably ignited by the weak flames. Also, over the entire range of parameters, the propane combustion process (and resulting pressure pulse) is substantially longer. This may be useful to the passive regulation of the inlet flow, as a longer pressure pulse is more likely to overcome the dynamic response time of the fluidic element and ensure that sufficient exhaust flow

moves upstream. In any case, these limits on the operating range are essentially functions of the fluidic element, which can be redesigned to accommodate a specific desired operating condition (or replaced by another passive or active flow regulation scheme). However, the overall results the effects of flow rate should hold regardless of the inlet regulation technique.

### III.3.f Combustion Frequency

Two changes in the performance of the combustion actuator are expected as the combustion frequency is increased. First, during  $t_{pulse}$ , there is no flow of fuel/air mixture into the chamber. This time is typically a few milliseconds and makes up a negligibly small part of the overall cycle duration in the low frequency limit. However, as the frequency is increased,  $t_{pulse}$  becomes an increasingly larger fraction of the cycle period. Thus the relative fraction of  $t_{refill}$  decreases, and, in order to maintain the same  $Q$ , the refill gas velocity must increase. For example, increasing from  $f = 1$  to 100 Hz with the same flow rate and assuming  $t_{pulse} = 3$  ms,  $t_{refill}/\tau$  decreases from 99.7% to 70% and a proportional increase in refill velocity is required. As discussed in §III.3.e, increasing fill velocity may result in increased flow turbulence which affects the combustion process (in addition to turbulence generated by the combustion process itself, which also increases with frequency).

Second, beyond the combustion products which vent during the high pressure pulse, any remaining products must be displaced by the new reactants entering the chamber. The process is analogous to the scavenging of a two-stroke engine, with an associated scavenging efficiency which describes the effectiveness of the exhaust displacement. Since this displacement process is accomplished with jets of fuel/air mixture, a certain amount of mixing of products and reactants is inevitable, and this mixing increases as  $Q$  is increased and the inlet jets become more turbulent. Mixing of the fuel/air with products from previous cycles has the effect of essentially making the mixture leaner with nitrogen, and therefore less of the gas in the chamber is chemically active and participates in the combustion process. Also, the temperature of the mixture in the chamber rises somewhat as hot exhaust gases are mixed in with the cool reactants.

Both of these effects are shown in Figure 46 which shows the phase-averaged combustor pressures for hydrogen with  $d = 1.09$  mm at three different  $Q$  and  $\Phi$  combinations each for variation in the normalized frequency,  $ff_{ideal} (= fV/Q)$ . The behavior of each of these sample cases is generally the same, as an increase in frequency yields a corresponding decrease in combustor peak pressures, similar to those observed for increasingly lean mixture ratios (e.g., peak pressure decreases from  $P_r = 4.72$  to 3.31 over the range  $0.1 \leq ff_{ideal} \leq 1.0$  for  $Q = 10$  cc/s and  $\Phi = 1.0$ ). However, in all cases,  $t_{peak}$  does not increase as rapidly (i.e., the burn rate does not decrease as much) as previously noted for decreasing  $\Phi$ . A direct comparison may be made between Figure 46a (varying frequency) and Figure 43a (varying mixture ratio) for identical  $d$  and  $Q$  values to observe this. For example, the cases of  $ff_{ideal} = 1.2$  and  $\Phi = 1.0$  and  $ff_{ideal} = 0.1$  and  $\Phi = 0.6$  have nearly

identical peak pressures ( $P_r = 2.92$  and  $2.99$ , respectively), but the higher frequency case has a faster  $t_{peak}$  ( $1.21$  ms compared to  $1.44$  ms) and overall shorter pulse duration.

The tendency for the pulse durations and pressure decay curves varying  $\Phi$  to become nearly identical at increasing flow rate (noted in §III.3.e) is observed to an even greater extent with variation in frequency. The turbulence increase associated with decreasing  $t_{refill}/\tau$  (and with the combustion process itself) is a function of the dimensional frequency (as opposed to the normalized frequency  $f/f_{ideal}$ ) and so is most notable for the high flow rate case of  $Q = 100$  cc/s (Figure 46c) where  $f$  is varied from  $10$  Hz up to  $120$  Hz. Over this range,  $t_{peak}$  values vary a comparatively small degree ( $0.83 < t_{peak} < 1.05$  ms), while the peak pressure decreases substantially from  $P_r = 4.02$  to  $2.56$ . This combined change yields a stronger effect than that seen for change in only  $Q$ , with a shorter pulse duration for the high frequency compared to the low frequency cases (even though the effective mixture ratio at lower frequencies is higher). It is also noted that the initial pressure in the chamber increases slightly with increasing frequency (from  $1.09$  at  $f = 10$  Hz to  $1.15$  at  $f = 120$  Hz), confirming that the velocity of the gas flow through the chamber increases when  $f$  is increased in order to maintain constant flow rate.

The overall effect for increased  $f$  in all cases is consistent with a combination of decreased mixture ratio (below the level of the input mixture) and increasing turbulence (above the level at  $f = 1$  Hz of equivalent  $Q$ ). Since these effects can not be accounted for separately from one another, the scavenging efficiency can not be calculated from the present data. However, since the increase in turbulence levels increase is expected to



lead to an increase in peak pressure, an upper bound on the scavenging efficiency may be approximated as 65% for  $Q = 10$  cc/s (i.e., the peak pressure at  $ff_{ideal} = 1.0$  equals the peak pressure that is expected at  $\Phi = 0.65$  from the low frequency baseline). This treatment is an oversimplification in that excess products are not chemically the same as excess air (excess air contains more oxidizer than excess products and is thus more conducive to the overall combustion process). However, it does provide a general sense of the scavenging efficiency and indicates that even at low flow rates, substantial improvement could be made to the exhaust gas displacement process.

The variation of the peak pressure with frequency is summarized for several sample flow rates in Figures 47 and 48 for hydrogen and propane, respectively. The results are all for  $d = 1.09$  mm with  $\Phi = 1.0$  for propane cases and  $\Phi$  for hydrogen is adjusted for each  $Q$  adjusted to keep it within the operating limits established in §III.3.e and plotted in Figure 44. The operating range of  $d$  and  $\Phi$  values established for the low frequency baselines holds for increased frequencies, although the maximum frequency at which the actuator successfully operates varies somewhat over this parameter space. For both fuels, excessively high operating frequencies result in the same type of actuator failures described previously, with either a standing flame created within the chamber or a sputtering and erratic combustion process. (Within the range tested, the maximum frequencies for successful operation are  $f = 120$  Hz for hydrogen and  $f = 60$  Hz for propane.) Most hydrogen cases are operated to values of  $ff_{ideal} > 1.0$ , (e.g., for  $Q = 100$  cc/s and  $\Phi = 0.5$ ,  $f = 120$  Hz is attained), which even with perfect exhaust scavenging has an effectively leaner mixture. For propane, the system only operates for  $ff_{ideal} \leq 0.8$  for

most test cases, presumably as a result of the more limited lean flammability range of propane (see Table 1). A generally linear decrease in peak pressure is observed for all test cases as the frequency is increased, although the peak values are nominally constant for hydrogen at  $Q \geq 50$  cc/s and  $f/f_{ideal} \leq 0.3$ . In these cases, substantial overfill of the chamber takes place (compared to the frequency of combustion) which is sufficient to displace nearly all of the exhaust products from previous cycles. It is also noted that the decrease in peak pressure with increasing  $f$  is typically faster for propane than hydrogen as a result of the greater sensitivity of propane combustion properties to changes in mixture ratio.

### III.3.g Ignition Energy

The ignition energy ( $E$ ) is of much greater interest in small-scale combustion than in typical larger scale combustion processes. For a given set of system properties, the ignition energy is essentially fixed regardless of the size of combustion volume. As such, the percentage of energy that has to be provided to initiate combustion relative to the energy released by the combustion process (one measure of the efficiency of the system) increases with decreasing volume. Also, at ignition, there is a transient start-up process where the ignition energy dictates the flame spreading before the combustion process and typical flame propagation takes over. Theoretically, this period should become increasingly important with decreasing volume. In the small volume limit when the system is below the flame quenching size, no stable combustion process can take place,

and heating and expansion of the gas may be due solely to energy addition from the spark. This concept of spark-only actuation is the basis of pulsed arcjet actuation schemes planned for micro-thrust and propulsion. Typical of these is the work of Willmes and Burton (1999) which used spark discharges with pulse energies of 24 to 132 mJ fired at frequencies on the order of 1 kHz to accelerate a helium propellant stream through a 380  $\mu\text{m}$  diameter nozzle and generate thrust levels up to 31 mN.

Turns (1996) lists the minimum ignition energy for stoichiometric mixtures of hydrogen and propane at STP as 0.02 mJ and 0.33 mJ, respectively. The effect of mixture ratio on minimum ignition energy varies substantially with fuel type, with hydrogen minimum ignition energy levels found at nearly exactly stoichiometric mixtures (Drell and Belles, 1958) and most hydrocarbons (including propane) having minimum ignition energies at somewhat fuel rich conditions (Lewis and von Elbe, 1987). The behavioral trends for minimum ignition energy level with variation in most parameters are similar to those for quenching distance, i.e., decreasing with increases in the initial pressure and temperature of the gas mixture (Lewis and von Elbe, 1987). Flow conditions at the spark gap are also of importance where the required ignition energy increases with flow velocity (Swett, 1949) and turbulence intensity (Ballal and Lefebvre, 1977, and Ujiie, 1994). Other studies have also found that the minimum ignition energy level may be substantially affected by the properties of the spark, particularly in the comparative energies and durations of the breakdown and arc phases of the discharge (Ballal and Lefebvre, 1975, and Maly and Vogel, 1978). It is sufficient to note that the spark ignition energy required for the combustion actuator (with increased flow velocity and turbulence at the spark gap

and a spark initiation process that is not optimized) will probably be substantially higher than the values listed by Turns.

The sensitivity of the combustion actuator to changes in spark ignition energy ( $E$ ) was assessed using a CDI system to nominally control the value of  $E$ . Test values for one operating state (hydrogen,  $\Phi = 1.0$ ,  $d = 1.09$  mm,  $Q = 10$  cc/s) are presented in Figure 49 for  $2 < E < 40$  mJ from the CDI system as well as ignition using the conventional induction coil automotive system used for all previous experiments. The resulting pressure curves are essentially invariant (within the error associated with the mixture reproducibility), suggesting that ignition energy has no effect on system operation provided it is sufficient to ignite the mixture. This result was found across the entire range of parameters tested, with all hydrogen and propane mixtures reliably ignited for  $E \geq 2$  and 20 mJ, respectively. Further reduced values may be achieved by tailoring the ignition energy level to the specific mixture and flowrate, however a specific mapping of minimum levels that are attained when varying these parameters was not attempted. (It should be noted that for  $E \leq 1$  mJ in the ignition capacitors, the spark could not reliably jump across the 2 mm spark gap prescribed in the parametric study, however, previous experiments with 1 mm spark gaps allowed successful ignition for all hydrogen mixtures with  $E = 1$  mJ.)

Firing of the spark gap in the chamber filled with pure air (i.e.,  $\Phi = 0.0$ ) produced no detectable pressure rise within the sensitivity of the pressure transducer. (Although not presented as a separate plot, this behavior can be inferred from the propane data of Figure

28, where the pressure rise over the 1 ms duration of the spark is negligible.) The ignition energy level does not affect the chamber pressure because  $E$  is substantially smaller than the chemical energy release associated with the combustion process. For a 1 cc combustion chamber (assuming complete burning of the mixture inside), the chemical energy release of  $\Phi = 1.0$  mixtures of hydrogen and propane at STP is 3190 and 3670 mJ, respectively. Across the entire range of mixture ratios and volumes tested, the chemical energy release is at least one order of magnitude larger than  $E$ , and more typically two to three orders of magnitude larger. This also indicates that the input/output efficiency of the device (at least comparing energy input to potential chemical energy release) is reasonable.

## CHAPTER IV

### LOW SPEED SEPARATION CONTROL WITH COMBUSTION-DRIVEN JET ACTUATORS

#### IV.1 Experimental Set-Up and Measurements

The utility of the combustion-driven jet actuator is demonstrated in low-speed flow control experiments where an airfoil model is equipped with a bank of 8 combustion-driven jet actuators integrated near the leading edge as shown schematically in Figure 50. The details of the airfoil design are proprietary and therefore the airfoil cross-section is not presented in its entirety here. The generally notable features of the airfoil section are that it is comparatively thin with a relatively sharp leading edge, such that the maximum thickness of the airfoil equal to 0.108 times the chord length,  $C$ , and the leading edge radius is approximately  $0.016C$ . The airfoil model is machined from aluminum using wire EDM and is of constant cross-section (2-D) with  $C = 22.9$  cm and the active spanwise section is 15.2 cm wide. To fit the eight combustion actuators as close to the leading edge as possible, the combustion chambers have a triangular cross-section with a base of 1.73 cm, height of 0.70 cm, and width along the span of 1.40 cm (yielding a volume of 0.85 cc per chamber). Each combustion chamber has a single slot exhaust orifice spanning the width of the combustion chamber with a height of 0.15 mm. The exhaust slot is machined perpendicular to the axis of the chord and exits 0.5 mm back from the maximum leading edge of the airfoil.

The airfoil was mounted in an open-return, low-speed wind tunnel having a square test section measuring 91 cm on a side. The maximum tunnel velocity is 30 m/s with a free-stream turbulence level less than 0.15%. The upper and lower walls of the wind tunnel are adjusted to compensate for blockage created by the wing. The active airfoil section was mounted at the center of the tunnel with clear thin fences at both ends, and the remainder of the test section was spanned by two dummy fiberglass sections. The spark wires and premixed fuel/air delivery lines are fed from the side of the model through dummy wing sections. Although the spark plugs to each chamber are wired and controlled individually, all are fired simultaneously in each of the test runs presented to keep the flow field across the active section as uniform as possible. In all the experiments shown, the mixture flow rate was held constant at 340 cc/s ( $f_{ideal}$  of 50 Hz per chamber) in order to eliminate mass flux from the actuator as a variable and to eliminate the effect of fill rate on the flame propagation. Hydrogen is used as the fuel with  $\Phi = 0.6$  (the maximum mixture ratio to maintain consistent actuator operation for the fixed slot orifice size and over the range of frequencies tested).

The nominally two-dimensional flow field is obtained from a sequence of PIV images that are captured in the  $x$ - $y$  plane above the suction side of the airfoil. Each PIV data set is comprised of a frame measuring 150 mm on the side where phase-averaged velocity (and vorticity) distributions are computed from an ensemble of 125 image pairs using a standard cross-correlation technique. The illumination is provided by a pair of 120mJ Nd:YAG lasers with a maximum repetition rate of 15Hz. The laser sheet is formed using a standard optical arrangement, and the images are captured using a 1008x1016 pixel

dual frame CCD camera mounted on a two-axis traverse (motion resolution  $\pm 0.06$  mm). The acquisition timing and spark ignition signals are provided by a National Instruments data acquisition board, and Labview codes are used to control the time delay between the spark ignition and the PIV acquisition. Smoke flow visualization images are selected randomly from the unprocessed images taken during the PIV data acquisition.

Since space limitations prevent the integration of a pressure transducer into the airfoil itself, a test chamber of identical shape and size is constructed to provide pressure measurements. The results for this geometry are generally comparable to similar results in cylindrical test chambers, with pulse durations of approximately 2 ms and with the same frequency effects (i.e., increasing frequency yields an effectively lower mixture ratio due to mixing with products from previous cycles and results in lower peak pressures). Several different calculations of  $C_\mu$  are presented in Table 7 (on the following page) for the baseline case and each of the actuation frequencies tested. In the absence of combustion (i.e., steady blowing),  $C_\mu$  is calculated directly using conservation of mass and the density of the fuel/air mixture. For cases with the actuators firing,  $C_\mu$  is calculated using the pressure data measured in the test chamber and the idealized thrust equations described in §III.3.b (the calculated values are reduced by 40% to match the typical discrepancy between measured and experimental values as shown in Figure 32). Three different calculations of  $C_\mu$  are presented for each case: the peak value (corresponding to the peak pressure level), the mean over the pulse duration, and the mean over the cycle period (including the high pressure pulse and subsequent slow, steady bleed from refill). In general, it may be stated that the peak and mean over the



pulse values of  $C_\mu$  decrease with increasing frequency, while the mean  $C_\mu$  over the cycle period increases with frequency. The peak values of  $C_\mu$  are much greater than conventional flow control experiments (where  $C_\mu \sim O(10^{-3})$ ) and are indicative of the high momentum which can be generated by the combustion-driven jet actuator. These calculations are presented for the sake of completeness, although, as is shown in the results section, the effects on flow separation in the present experiments are essentially the same across the full range of  $C_\mu$  values. Due to the impulsive nature of the combustion actuator (as opposed to the typically time periodic or sinusoidal nature of most flow control schemes), each of these  $C_\mu$  values may be of interest as a parameter and more in-depth study will be required to determine the relative importance of each to flow control effectiveness.

**Table 7.** Calculated dimensionless momentum coefficients for low speed separation control experiments with combustion-driven jet actuators.

Freestream velocity, $U_\infty$ (m/s)	Frequency, $f$ (Hz)	$C_\mu (\times 10^3)$		
		Peak	Mean over pulse duration	Mean over cycle period
12.5	0 (steady blowing)	n/a	n/a	0.98
	3	228.1	89.2	1.64
	15	217.7	84.8	4.10
	30	186.7	78.2	6.72
	45	142.1	67.7	8.39
25.0	0 (steady blowing)	n/a	n/a	0.25
	3	57.0	22.3	0.41
	15	54.4	21.2	1.03
	30	46.7	19.6	1.68
	45	35.5	16.9	2.10

## IV.2 Experimental Results

The airfoil is mounted at an angle of attack,  $\alpha$ , of  $24.1^\circ$ , where the flow is massively separated near the leading edge of the airfoil with a large recirculation region over the upper surface. Figures 51 and 52 show the velocity vector fields and vorticity contours in the absence of actuation for free stream velocities of  $U_\infty = 12.5$  and  $25$  m/s, respectively (where the corresponding Reynolds numbers based on the chord length ( $Re_c$ ) are 180,000 and 360,000). Figures 51a and 52a show the conditions with the actuator fully off (i.e., with no fuel/oxidizer flow to the actuator), and in both cases, the flow separates broadly from the airfoil at  $X/C = 0.1$ , corresponding closely to the location where the upper surface of the airfoil begins to slope downward at this angle of attack. The separating shear is clearly visible and is marked by concentrations of CW vorticity (with the shear layer centerline generally linear from the separation point, tilted upward at an upward angle of approximately  $30^\circ$ ). Figures 51b and 52b show the same conditions but with the premixed fuel/air flowing through the slots on the leading edge of the airfoil, with dimensionless momentum coefficients of  $0.98 \times 10^{-3}$  and  $0.25 \times 10^{-3}$ , respectively. The addition of this steady blowing moves the shear layer slightly away from the airfoil surface near the leading edge and somewhat decreasing the distance from the leading edge at which full separation occurs. This effect is more pronounced at the lower free stream velocity (i.e., higher  $C_\mu$ ) (Figure 51b - where the separation point is at roughly  $X/C = 0.05$ ), but it is minor in both cases and has no other effect on the large scale separation over the remainder of the airfoil.

The transient effect of the combustion-driven jet actuators on the flow is shown qualitatively in a series of smoke flow visualization images (Figure 53). These images are for  $f = 3$  Hz and  $Re_c = 180,000$ , with images of the flowfield starting at ignition (before any jet exhausts the orifice) and subsequently through 20 ms after ignition. The image at ignition (Figure 53a) shows the same type of broad separation at the leading edge as indicated in the PIV from the baseline cases. Near the peak of the pressure curve (approximately 1 ms – Figure 53b), the jet from the actuator can be seen as a dark (unseeded) region in the flow emanating from the leading edge. The pressure pulse is largely over by 2 ms (Figure 53c) with the jet structure still visible but with ambient seed particles entrained into the jet. By 5 ms (Figure 53e), the forward momentum of the actuator jet fluid has been stopped and turned back by the free stream flow. The actuation apparently leads to a significant change in circulation as is evident by the appearance of a large vortical structure which increases in size as it is advected over the length of the airfoil, approximately following the same trajectory as the shear layer of the separated region. By 20 ms (Figure 53i), the structure has moved to the edge of the field of view. Behind this structure, the flow is reattached to the airfoil surface, strongly at first (Figure 53f) and then gradually transitioning back to the initial broadly separated condition.

Smoke flow visualization images of when the actuator is operating with  $f = 45$  Hz are shown in Figure 54 with the same free stream velocity ( $Re_c = 180,000$ ). The images show the same type of flow developments as observed in the nearly transient (i.e., low frequency) case, with the jet fluid from the combustion actuator turned back by the

freestream approximately 3 ms after ignition (Figure 54c), and a subsequent large vortex which is advected along the surface of the airfoil. In this case, however, the actuation frequency is sufficiently high that when the actuation is repeated, the flow is still largely attached to the surface from the previous cycle. Once again, the vortical structure are advected along the same path as the shear layer, in this case following just above the airfoil surface, while the flow upstream of the structure is reattached (Figure 54f).

PIV data sets (including velocity vectors and vorticity contours) for four dynamic cases are presented in Figures 55 through 58. In these data sets, the Strouhal number (based on the chord length,  $St \equiv fC/U_\infty$ ) is varied, and the phase is characterized in terms of  $t/\tau$  (the percentage of the cycle period). The results for all four cases show the same type of flow structures as observed in the smoke flow visualization images, with the vortical structure resulting from the combustion pulse clearly visible in the vorticity contours. Figure 55 shows data for  $St = 0.137$  where the flow is still broadly separated at the beginning of each cycle (although the angle of the separated shear layer relative to the free stream is substantially reduced compared to the baseline and transient cases). The vortex which is formed as a result of each pulse from the actuator bank is clearly indicated by the vorticity contours (Figure 55a) and is advected downstream along the path of the shear layer at slightly lower than the free stream velocity, with a temporary reattachment of the flow behind it. By  $t/\tau = 0.60$ , the flow is again separated and has moved nearly back to its original state. Figure 56 ( $St = 0.274$ ) shows similar but slightly smaller initial flow separation, with the curvature of the shear layer near the edge of the field of view

suggesting a confined separation bubble over the airfoil surface. Similar momentary attachment of the flow is observed before it returns to the separated state (Figure 56g).

Figures 57 and 58 ( $St = 0.549$  and  $0.823$ , respectively) continue this trend, with a separation bubble on the airfoil surface that is visible within the field of view. The size of this region decreases as  $St$  is increased and, for Figure 58 (which corresponds to the smoke flow visualization case of Figure 54), the initial separation bubble is relatively small and limited to  $X/C$  between  $0.1$  and  $0.5$ . Again the vortical structure formed as a result of the actuator pulse follows the shear layer (in these cases almost directly over the surface of the airfoil) and is advected downstream at approximately  $80\%$  of the free stream velocity. The data suggest that with  $St$  approaching  $1.0$  or greater (such that actuation time is greater than or equal to flight time over the airfoil surface) effectively steady reattachment of the flow can be achieved. Although this is not an unexpected result in light of previous flow control experiments, it is worth noting that this key frequency level is still important for the impulsive actuation of the combustion-driven jet actuator (as opposed to other periodic or sinusoidal actuation schemes).

## **CHAPTER V**

### **CONCLUSIONS**

Two novel fluidic actuators for flow control are demonstrated: the compressible synthetic jet and the combustion-driven jet actuator. Both of these devices are characterized over a range of relevant operating parameters, and both are shown to be capable of producing high speed jets (with subsequently high momentum), making them suitable candidates for high speed flow control applications. Each could be integrated into aerodynamic systems for testing at flight speeds, but the combustion-driven jet actuator is the better candidate for further testing, due to the fact that it is low in weight and infrastructure requirements and can effectively be operated with no moving parts. Practical integration into existing flight platforms will require adaptation of the combustion process to liquid fuels, and thus further actuator characterization for its performance with combusting droplet sprays rather than gaseous fuels will be required. By contrast, the reciprocating pistons used in the present experiments to generate the compressible synthetic jets are likely too heavy and hardware intensive to be of practical use in flight systems. However, the development of a lighter driver technology could render such actuators feasible and the results of the present experiments should hold for any suitable driver with sinusoidal motion.

## V.1 Compressible Synthetic Jet

The compressible synthetic (i.e., zero net mass flux) jet is studied using a reciprocating piston/cylinder actuator with a volume displacement of 6.49 cc. Variation in three fundamental system parameters is investigated: orifice diameter ( $d$ , normalized as the dimensionless stroke length,  $76 \leq L_0/d \leq 2065$ ), actuation frequency ( $0 \leq f \leq 200$  Hz), and compression ratio of the cylinder ( $3.2 \leq r \leq 27.1$ ). For sufficiently low combinations of  $L_0/d$  and  $f$  for a given  $r$ , the system operates in accordance with previous synthetic jets in the literature, with a sinusoidal pressure waveform which corresponds closely to the velocity of the piston driver, yielding blowing and suction phases of nearly equivalent durations and pressure ratios. As either  $L_0/d$  or  $f$  is increased, the pressure waveform develops greater extrema in both the suction and blowing phases (for the highest pressure experimental case,  $0.23 \leq P_r \leq 7.93$  over the cycle) and compressibility effects within the cylinder develop. These effects change the shape of the pressure curve as the maximum pressure over the cycle migrates from  $t/\tau = 0.25$  (where the piston velocity is at a maximum) towards  $t/\tau = 0.50$  (where the cylinder volume is at a minimum) and an asymmetry develops in the rise and fall times of the pressure curve. There is also a corresponding shift in the duty cycle of the system towards greater periods in suction. This is due to the flow through the orifice during the blowing phase being driven by the high pressures generated within the cylinder, while the flow during the suction phase is inherently driven by only the ambient pressure outside the cylinder. As a result, the system must spend greater periods in suction in order to remain zero net mass flux.

The maximum and minimum pressures over the cycle are recorded, and, for  $r = 27.1$ , sonic pressure levels for blowing and suction may be achieved for any sufficiently high combination of  $f$  and  $L_0/d$ . It is noted that due to the shift in duty cycle towards greater periods in suction, the maximum pressure increase at a faster rate than the minimum pressure decreases, and as a result, the maximum blowing velocity of the system increases more rapidly than the maximum suction velocity. The dimensionless parameter  $St_{L_0}$  is introduced which combines  $f$  and  $L_0/d$  into a single parameter (with an experimental range of  $0 \leq St_{L_0} \leq 1.93$ ). The data for maximum and minimum pressures for variation in both frequency and orifice diameter collapse onto a single curve for variation in  $St_{L_0}$ , suggesting it as a key characterization parameter for the compressible synthetic jet. For individual experimental cases with identical  $St_{L_0}$  but different  $f$  and  $L_0/d$ , the pressure variation over the cycle is extremely similar with a slight tendency towards more extreme pressure curves for the higher frequency cases. This is attributed to unsteady losses at the orifice which are expected to increase with the frequency and correspondingly increase the resistance to flow through the orifice.

The pressure curves over the cycle for variation in compression ratio are essentially identical for cases where low cylinder pressures are observed (i.e., low  $f$  and/or  $L_0/d$ ) and the system operation is nominally incompressible. However, as the pressures are increased, the effect of  $r$  is substantial, with lower compression ratios yielding smaller pressure extrema for both the blowing and suction phases. The phase shift in the maximum pressure towards TDC is consistent regardless of the compression ratio, even though the pressure curve over the cycle at low  $r$  remains nearly sinusoidal in shape over



the full range of  $f$  and/or  $L_0/d$ . The data for each compression ratio reduce well with  $St_{Lo}$  but with each value for  $r$  showing a different characteristic curve for the maximum and minimum pressures over the cycle. It is noted that at smaller compression ratios the pressure curve over the cycle (and the corresponding pressure peaks) approach a level at which they are largely invariant with  $St_{Lo}$ , suggesting that there may be a characteristic limit on the pressure levels for a given  $r$ .

The fundamental structure of the compressible synthetic jet is observed with Schlieren flow visualization and PIV measurements. Due to the large  $L_0/d$  values over the experimental range, the structure of the compressible synthetic jet is dominated by a strong starting jet, in contrast to conventional synthetic jets which are composed primarily of vortex rings/pairs which coalesce into a turbulent jet in the far field. A starting vortex appears with the compressible synthetic jet but it is quickly followed and overtaken by the high speed starting jet. For sufficiently high combinations of  $f$ ,  $L_0/d$ , and  $r$ , the cylinder pressure is high enough for the jet to reach supersonic velocities, and an underexpanded supersonic jet emanates from the orifice, with shock cells in the near field. The flow outside the cylinder over the suction phase is similar to conventional synthetic jets, with a hemispherical sink-like flow at the orifice. The jet strength corresponds closely to the cylinder pressure, and jet speeds up to 600 m/s are documented.

A quasi-static numerical model is developed to aid in understanding the system operation. This simplified simulation assumes inviscid and isentropic flow through the

orifice, isentropic compression and expansion within the cylinder, and no heat transfer to the cylinder or orifice plate. The model agrees well with the experimental trends observed (including the changes in pressure magnitudes and the shape of the pressure curve) while it typically underestimates the pressures for individual experimental cases (due primarily to the unrealistic assumption of lossless flow through the orifice). The simulation indicates that substantial gas temperatures may be generated within the cavity and that the air mass displacement per cycle decreases as the cavity pressure increases. The maximum air mass within the cylinder over the cycle decreases substantially as a result of the compressibility effects confirming that the essential limit on the system operation is the intake of air into the cylinder during the suction phase. For the idealized model, all cases with the same  $St_{Lo}$  have identical pressure curves, again confirming the utility of this parameter.

The numerical simulation allows for general predictions to be made about compressible synthetic jet performance beyond the current experimental range. Specifically, the trend towards an upper limit on the cylinder pressure with increasing  $St_{Lo}$  is fully realized for the simulation results. It is noted that the maximum and minimum pressures over the cycle asymptotically approach  $r^{\gamma/2}$  and  $r^{-\gamma/2}$ , respectively. These relations may be combined to match the pressure-volume equation for isentropic compression-expansion of a closed system. It is found that as  $St_{Lo}$  is increased (i.e, the orifice size decreased or the frequency increased), the mass displacement is small in comparison to the mass that remains within the cylinder, and thus in the limit the system is essentially closed. This limit is reached at lower  $St_{Lo}$  for lower compression ratios, due to the inherently greater

air mass within the cylinder which can not be displaced at lower  $r$  and subsequently lower cylinder pressures and mass fluxes through the orifice.

Finally, a simple experiment is performed with flapper valves on the inside of the cylinder head, essentially increasing the orifice area over the suction phase of the cycle. This technique mitigates the compressibility limitations on system performance by allowing more air to enter the cylinder during the suction phase. The result is a substantial increase in the maximum cylinder pressure over the cycle and a correction in the duty cycle back to nearly equal blowing and suction durations.

## V.2 Combustion-Driven Jet Actuator

The combustion driven-jet actuator is a novel device which uses a combustion process within a small-scale ( $V \sim 1$  cc) chamber to create a high-speed jet of product gases through an exhaust orifice. The premixed fuel/air is ignited by an integrated spark gap, and the flow of reactants is controlled by a small fluidic pressure drop element such that the device has no moving parts. For this configuration, combustor pressure ratios ( $P_r$ ) up to 5 are demonstrated and operating frequencies greater than 100 Hz are realized. The operation of this device is characterized for cylindrical combustion chambers with variation in fuel type and mixture ratio, exhaust orifice diameter, chamber aspect ratio, chamber volume, mixture flow rate, ignition/combustion frequency, and spark ignition energy.

The fuel type and mixture ratio are integral parameters in that they set the chemical energy released by the combustion process and the flame speed (which controls the rate at which the chemical energy is released). Hydrogen and propane are both demonstrated as viable fuels, with hydrogen showing substantially higher peak pressures and shorter pulse durations due to its faster laminar flame speed compared to propane. For both fuels, leaner mixture ratios result in lower peak pressures and longer pulse durations as a result of decreased flame speeds and lower chemical energy release, with hydrogen exhibiting typically lower lean flammability limits than propane. The time to the peak pressure scales closely with the flame propagation speed, further confirming it as a key parameter and suggesting fast burn times are necessary to generate higher combustor pressures.

The exhaust orifice diameter is also critical here as it controls the rate at which exhaust gas is vented from the chamber. As expected, smaller orifice diameters yield higher peak pressures and overall longer pulse durations. It is noted, however, that the time at which the peak combustor pressure is reached is virtually invariant with orifice diameter, suggesting that the combustion process is largely independent of the orifice size. The behavioral trends for mixture ratio hold for all orifice diameters tested, and it is noted that there is differential between the idealized constant volume combustor pressure and the peak combustor pressure which is characteristic to each orifice diameter (and increases with increasing  $d$ ). This differential increases slightly as the mixture ratio is reduced as a result of decreased flame speeds. The operating range of the actuator (in terms of

mixture ratio) varies with the orifice diameter, as sufficient chamber pressure must be generated to stop the flow of reactants

While the combustor pressure can be increased continuously by decreasing the orifice diameter, this is not necessarily useful for flow control applications where jet momentum is the parameter of interest. It is shown that an idealized momentum flux (or thrust) of the jet may be calculated directly from the pressure data, and limited experimental thrust measurements give results that are roughly 60-65% of this idealized value. This calculation allows the peak momentum flux of the jet to be characterized, and this value typically decreases as the orifice diameter is decreased. For experimental cases with low chamber pressure (i.e., propane at all mixture ratios and hydrogen with  $\Phi \leq 0.7$ ), an optimum diameter is found for maximizing this value. At higher chamber pressures, the thrust increases continually as orifice diameter is increased over the experimental range.

The chamber aspect ratio is of interest in that it controls the flame propagation directions and the subsequent rate of chemical energy release. In accordance with expectations, chambers with  $H/D \approx 1$  exhibit the fastest burn times, with somewhat slower burn times for  $H/D < 1$ , and substantially slower burn times for  $H/D > 1$ . The shape of the pressure curve varies substantially with the aspect ratio, suggesting that it is possible to use the shape of the chamber to tailor the pressure characteristics. It is noted that higher chamber peak pressures are observed for  $H/D < 1$  in spite of the slower burn times. This is attributable to a reduced loss of unburned reactants through the exhaust orifice (as the distance from the spark gap to the exhaust orifice is smaller and thus the flame front

reaches the orifice earlier in the cycle). This suggests an additional loss mechanism which future actuators may be designed to minimize.

The chamber volume dictates both the amount of chemical energy contained within the combustor and the volume to surface area ratio (which will affect the extent of heat transfer losses to the walls). Chamber volumes as low as 0.25 cc (with characteristic dimensions still well above the quenching distance) are demonstrated for the combustion-driven jet actuator. For a given orifice diameter, the peak pressure decreases substantially with decreasing chamber volume, although the characteristic pressure rise is faster for smaller volumes. It is noted that smaller volumes allow faster burn and chamber refill times and subsequently higher operating frequencies, such that a design trade-off between higher chamber pressures and greater frequencies may be made.

The flow rate of mixture into the chamber affects the flame propagation in that it may increase the turbulence intensity within the chamber and it also creates a mean flow within the chamber that can substantially influence the initial flame propagation. The combined effect is an overall increase in the burning velocity which results in higher peak pressures and shorter pulse durations. Flame photography of propane-air in a 1 cc cubical chamber reveals that the flame is initially driven towards the exhaust orifice by the mean flow of the refill gases (and that the extent of this may be gauged by the ratio of the mean refill velocity in the chamber to the laminar flame speed). The flame front only propagates towards the inlets of the chamber after sufficient pressure develops within the chamber to shut off the flow of inlet gases. Substantial wrinkling of the flame front is

observed as the flow rate is increased and the flame propagation transitions from laminar propagation at low flow rate ( $Q = 10$  cc/s) towards a wrinkled laminar flame front at higher flow rates. Similar effects are anticipated for hydrogen but with a somewhat reduced flow rate effect due to the higher flame speed and lower flame thickness for hydrogen. The operating space (in terms of  $\Phi$  and  $d$ ) for hydrogen mixtures changes towards smaller diameters and leaner mixture ratios as the mixture flow rate is increased in order to ensure stable, independent combustion bursts and prevent the creation of a standing flame front within the chamber. This is not observed for propane due to its reduced flammability and longer pulse duration. At any combination of  $\Phi$  and  $d$  at which the actuator successfully operates, increased mixture flow rate increases the peak pressure and shortens the pulse duration, consistent with a net increase in the burning velocity.

The operating frequency also exhibits a dual effect on the combustion process. First, increased frequencies reduce the amount of overfill of the chamber with reactants, and, due to mixing with products from the previous cycle, the mixture is effectively driven leaner. Second, increased burning time as a percentage of the cycle period necessitates faster refill velocities in order to maintain the same mixture flow rate and thus yields a further increase in mixture turbulence. The combined effect is that higher operating frequencies yield decreases in peak pressure (consistent with leaner mixtures), but due to the increased turbulence, the burn time (and corresponding pulse duration) does not increase as much as previously observed for mixture effects. Excessively high frequencies yield the same type of actuator failure noted previously with insufficient chamber pressure to cut off the flow of reactants to the chamber. Due to their relative

lean flammability limits, it is noted that hydrogen mixture ratios typically operate to a normalized frequency above 1.0 (greater than 100% of the idealized frequency based upon the chamber volume and mixture flow rate) whereas propane mixtures typically only operate at normalized frequencies less than or equal to 0.8.

The effect of the spark ignition energy on the combustor pressure curve is found to be negligible provided that it is sufficient to initiate the combustion process. Over the range of operating conditions, minimum ignition energies of 2 and 20 mJ are found to be sufficient to ignite all hydrogen and propane mixtures, respectively. This energy input is 2 to 3 orders of magnitude smaller than the typical chemical energy release from the combustion process, and thus the small-scale combustion process (at least on the 1 cc scales envisioned) is deemed practical from an energy input to output perspective.

Finally, a bank of eight combustion-driven jet actuators are mounted in the leading edge of an airfoil in order to demonstrate their utility at operating conditions similar to previous flow control experiments. The airfoil is of unconventional design with a sharp leading edge which creates a baseline massive flow separation at high angle of attack ( $\alpha = 24.1^\circ$ ). A transient pulse from the combustion actuators results in a large vortical structure which develops. This structure rolls backwards over the surface of the airfoil with a momentary reattachment of the flow to the airfoil surface behind it. For increased actuation frequencies, the same structure is observed as each pulse occurs, but the degree of separation between pulse decreases. As Strouhal number based on the chord length



approaches 1 (such that the flight time over the airfoil is commensurate with the period of the actuation), effectively steady reattachment of the flow to the airfoil is observed.

## APPENDIX

### ORIFICE GEOMETRY EFFECTS

In the present experiments, straight-walled, round orifices are used as the primary orifice geometry in order to ensure dimensional similarity between all orifices, as the relatively small diameters tested (as low as  $d = 1.6$  mm for the compressible synthetic jet and  $d = 0.79$  mm for the combustion driven jet actuator) make it difficult to reliably reproduce any taper or nozzle-like shaping across all of the orifices diameters. The selection of the orifice plate thickness ( $l/d = 2.0$ ) is based upon the work of Fried and Idelchik (1989) who report that for steady flow (with  $Re > 10,000$ ) through a thick-walled simple orifice with infinite flow cross-sections on either side, the discharge coefficient decreases as the orifice plate thickness is increased (from 2.85 for an infinitely thin orifice to a minimum value of 1.55 at  $l/d \geq 2.0$ ). Although the physical mechanism behind this is not explicitly discussed, it is likely that for sufficiently thick orifices the flow reattaches to the orifice walls before exhausting, thus minimizing the losses associated with the formation of a vena contracta around the sharp edged corners of the orifice entrance. A separate loss term must also be included for pipe flow losses within the orifice itself as the thickness is further increased, thus  $l/d = 2.0$  results in the minimum flow resistance under the above stated conditions.

The present actuators differ from this simple case in the literature primarily in that the flow through the orifice is highly unsteady, and the flow speed can range from zero to

sonic levels over comparatively short time intervals. As discussed in §II.2, the results for the compressible synthetic jet already suggest that potential unsteady effects in the orifice flow resistance may be responsible for the differences in pressure magnitudes for cases with the same  $St_{Lo}$  but differing frequencies (see Figure 8). Several different orifice configurations are tested to determine the sensitivity of both actuation schemes to changes in orifice geometry and to assess the assumption of unsteady effects contributing to the losses. Sample results for the compressible synthetic jet are presented in Figure 59 for  $r = 27.1$  and  $L_0/d = 2065$  varying  $f$ . In addition to the standard orifice geometry ( $l/d = 2.0$ ), a thinner orifice plate ( $l/d = 0.5$ ) is tested as well as an orifice plate of standard thickness but with a  $45^\circ$  conical chamfer (to a depth of approximately 25% of the plate thickness) on each side of the orifice, thus eliminating the sharp edges of the orifice for flow in both the suction and blowing phases. The results for  $f = 10$  Hz (Figure 59a) show performance trends of the type expected for steady flow through each of these configurations. In agreement with Fried and Idelchik, the thinner orifice plate yields substantially greater pressure extrema over the cycle than the standard plate ( $0.90 \leq P_r \leq 1.16$  for  $l/d = 0.5$  versus  $0.91 \leq P_r \leq 1.12$  for  $l/d = 2.0$ ) as would be expected for an orifice with a higher discharge coefficient (i.e., greater flow resistance). Similarly, the orifice plate with chamfered edges has reduced flow resistance compared to the standard orifice and subsequently has a lower pressure range over the cycle ( $0.93 \leq P_r \leq 1.08$ ). At  $f = 25$  Hz (Figure 59b), the results are generally similar with wide differences in the pressures for all three orifices and the comparative results in the same order as previously observed. However, by  $f = 50$  Hz (Figure 59c), the percentage difference in the pressure magnitudes reduces dramatically, with the maximum  $P_r = 4.12, 3.85$ , and  $3.63$ , for the thin, standard,

and chamfered orifices, respectively. Further increase in frequency to 100 Hz (Figure 59d) yields pressure curves and magnitudes that are nearly identical for both straight-walled orifice configurations ( $0.22 \leq P_r \leq 6.41$  for  $l/d = 0.5$  versus  $0.22 \leq P_r \leq 6.35$  for  $l/d = 2.0$ ). The pressure magnitudes for the chamfered orifice still lag these values ( $0.23 \leq P_r \leq 5.75$ ), but the percentage difference is further reduced. Generally similar results were found for variation in orifice geometry at other values of  $r$  and  $L_0/d$  over the experimental range, and the overall trend is for the pressures curves for different orifice geometries to become increasingly similar as frequency is increased. This suggests that unsteady losses at the orifice do play a significant role in determining the resistance to flow through the orifice and, in the high frequency limit, can be of greater significance than the effect associated with the orifice geometry.

The orifice geometry variation for the combustion-driven jet actuator for  $d = 1.30$  mm and  $Q = 10$  cc/s is presented in Figures 60a and b for stoichiometric mixtures of hydrogen and propane, respectively. Results for the standard orifice geometry ( $l/d = 2.0$ ), a thinner orifice plate ( $l/d = 0.75$ ) and an orifice plate of standard thickness but with a  $45^\circ$  conical chamfer (to a depth of approximately 50% of the plate thickness) on the upstream side of the orifice. In contrast to the compressible synthetic jet (where the time scale of the pressure curve scales directly with frequency), the pressure rise time for the compression-driven jet actuator stays on the same approximate time scale ( $O \sim 1$  ms) regardless of the combustion frequency. Thus, the unsteady effects for flow through the orifice are largely decoupled from the actuator frequency and may be quite substantial at any operating conditions. The results presented in Figure 60 indicate that there is only a slight variation

in the peak chamber pressure (and overall pressure curve) with changes to the orifice geometry. The variation that is observed is consistent with expectations, with the thin orifice ( $l/d = 0.75$ ) yielding slightly larger peak pressures than the standard and the chamfered orifice yielding slightly smaller peak pressures. For both hydrogen and propane, the peak pressure variance over the range of orifice geometries is less than 10%. This further indicates that at high rate of change in the pressure (typical for the combustion-driven jet actuator and for high frequency operation of the compressible synthetic jet), the unsteady losses at the orifice are more substantial than losses associated with the variation in geometry.

## FIGURES

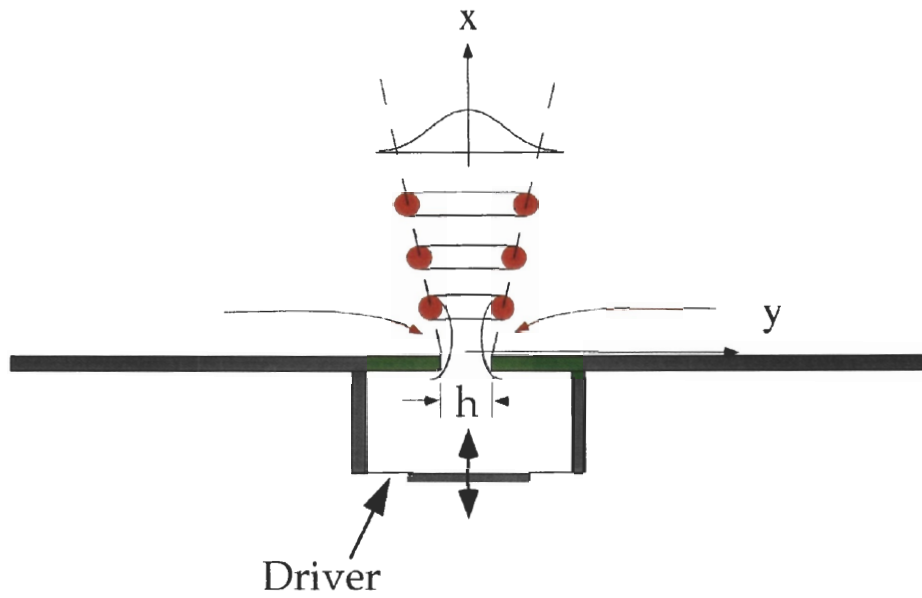


Figure 1. Conceptual drawing of synthetic jet. (Courtesy of Smith and Glezer, 1998.)

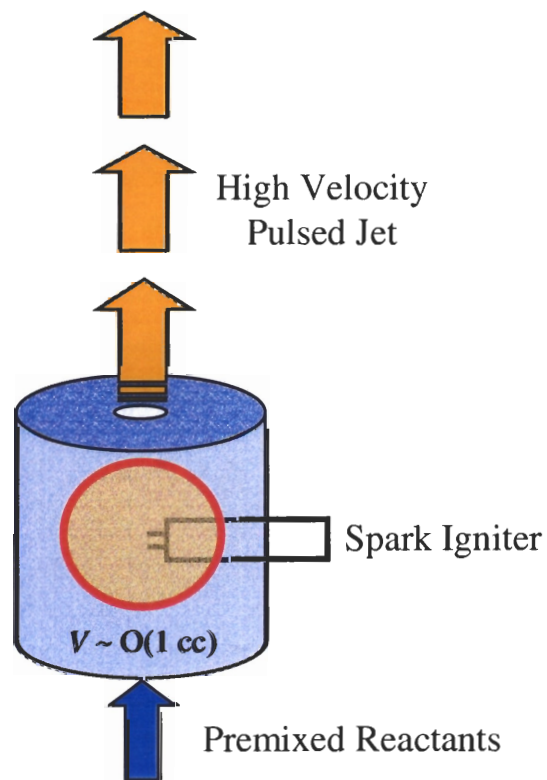


Figure 2. Conceptual drawing of combustion-driven jet actuator.

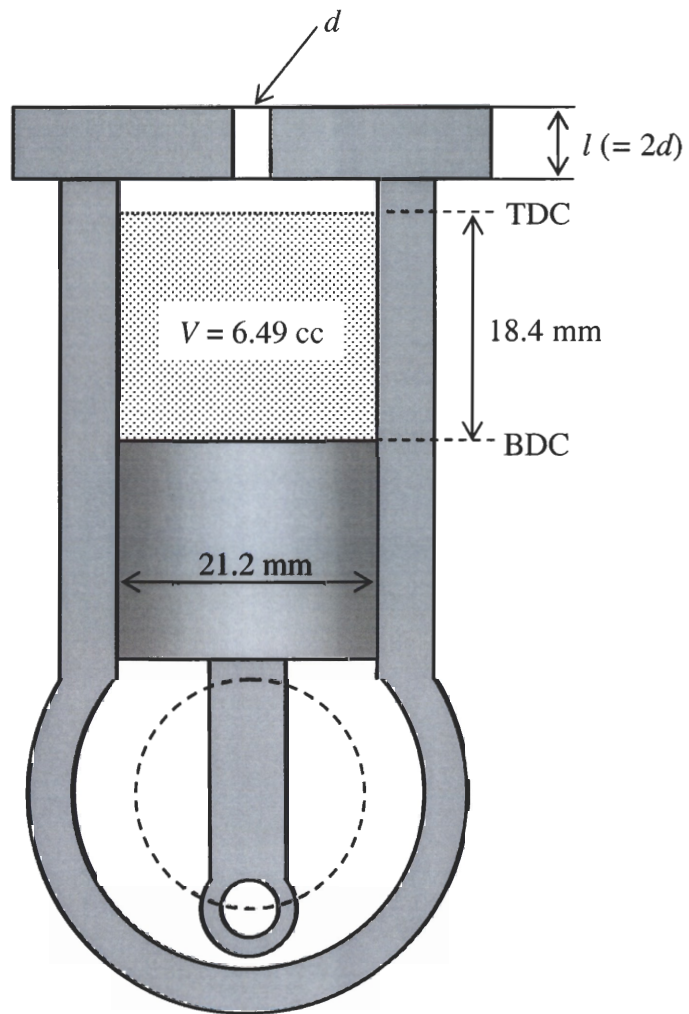


Figure 3. Schematic diagram of piston/cylinder actuator.



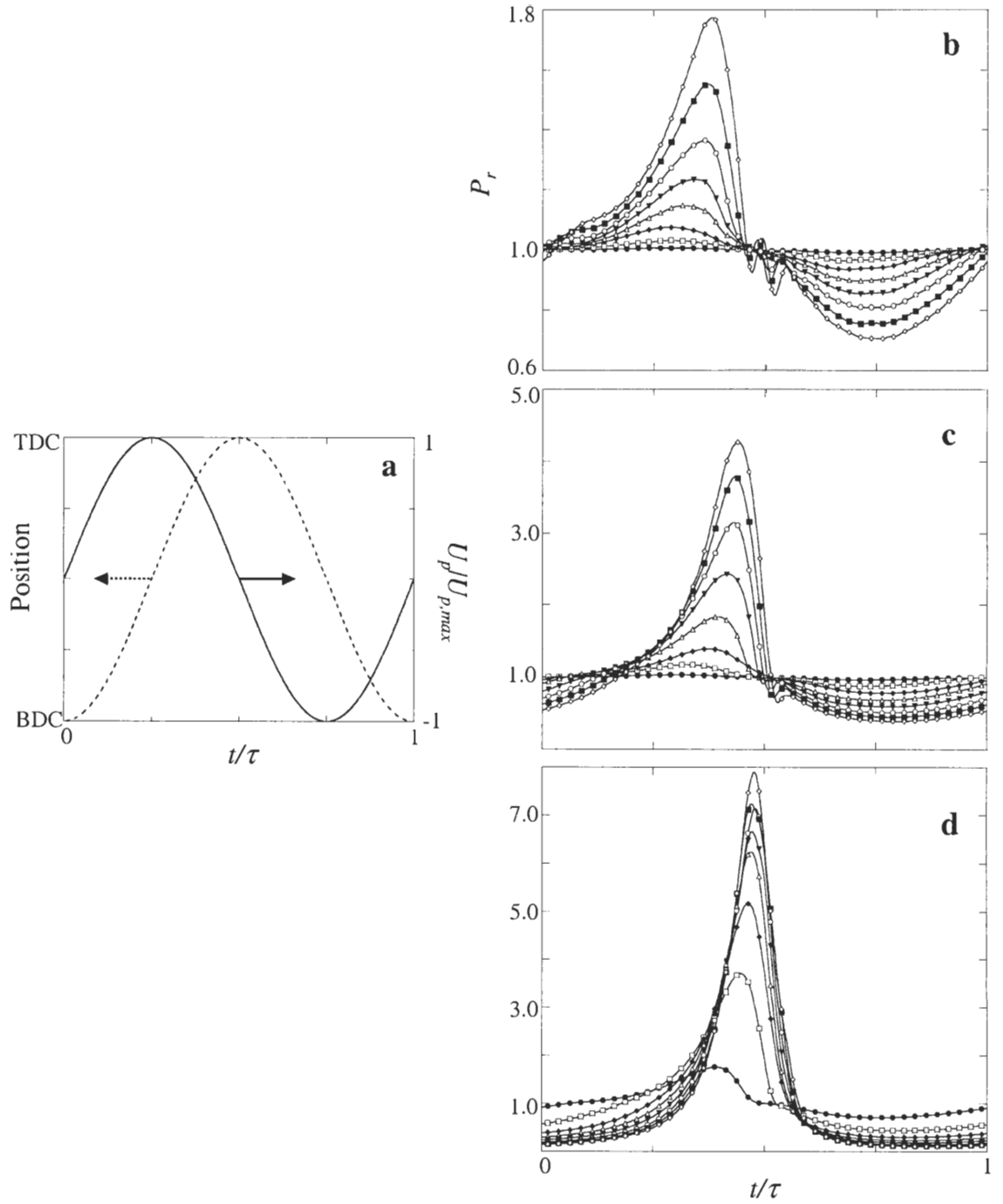


Figure 4. Piston position and velocity over cycle (a) and phase-averaged cylinder pressures for  $r = 27.1$  and  $L_0/d = 76$  (b), 258 (c), and 2065 (d) for  $f = 25$  (●), 50 (□), 75 (◆), 100 (Δ), 125 (▼), 150 (○), 175 (■), and 200 (◇) Hz.

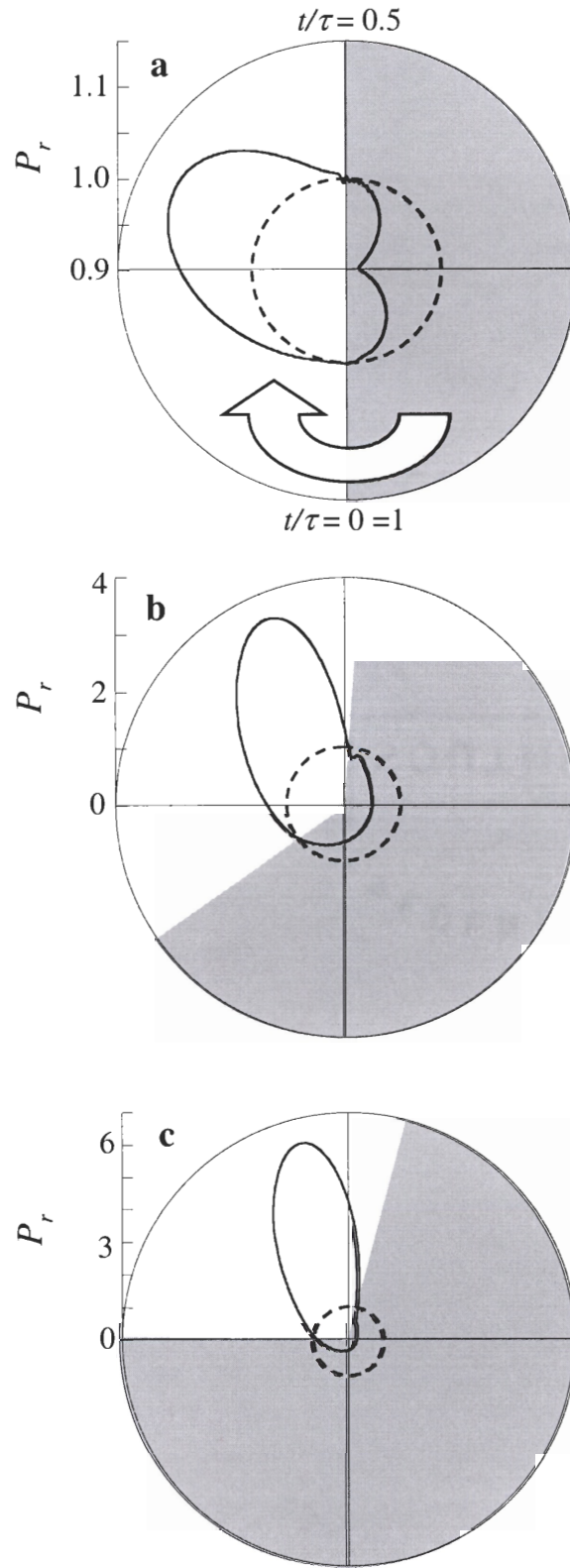


Figure 5. Phase-averaged cylinder pressures over cycle in polar coordinates for  $r = 27.1$  and  $L_0/d = 612$  for  $f = 25$  (a), 100 (b), and 200 Hz (c) with reference circle at  $P_r = 1.0$  and suction cycle shaded.

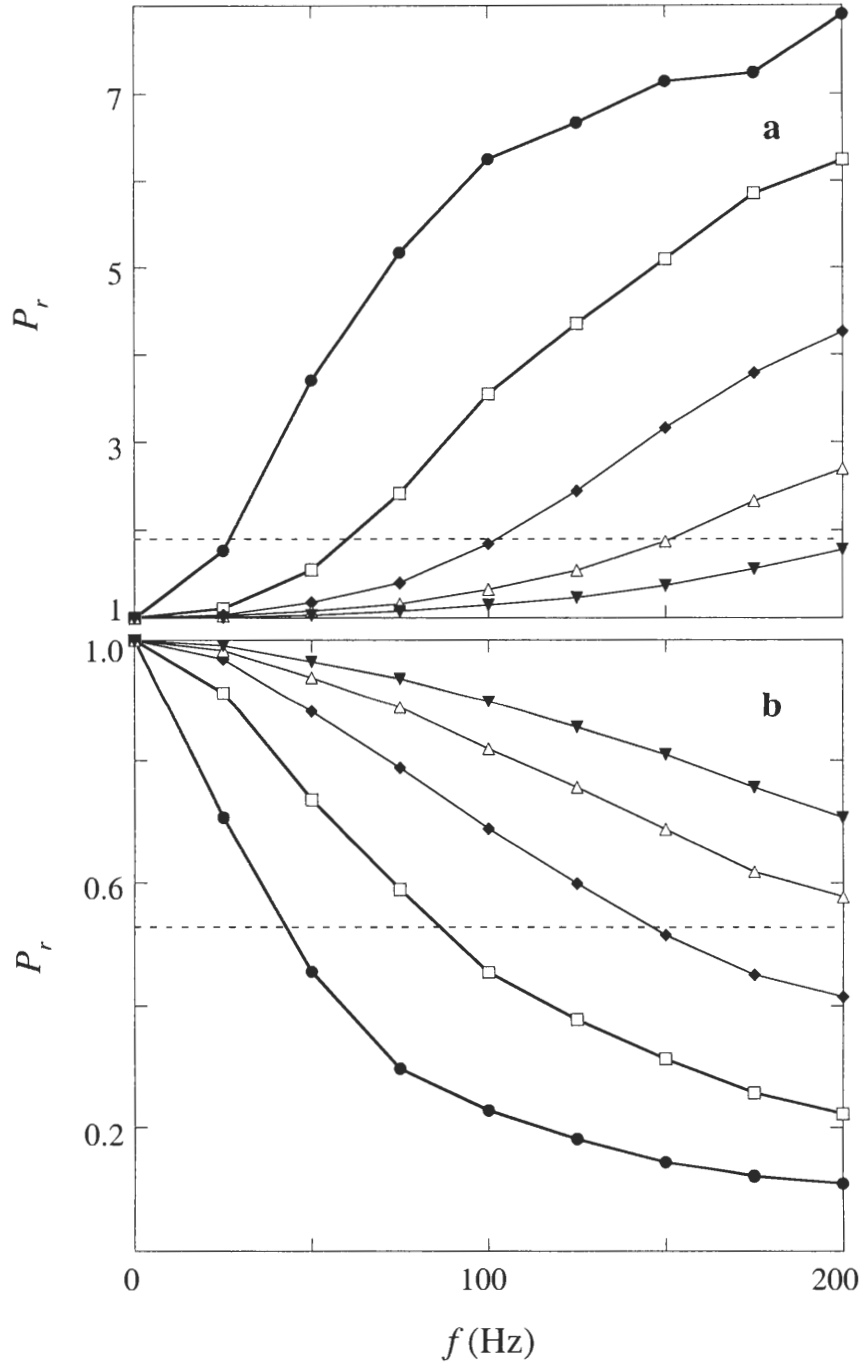


Figure 6. Maximum (a) and minimum (b) pressures over cycle varying  $f$  for  $r = 27.1$  and  $L_0/d = 2065$  ( $\bullet$ ), 612 ( $\square$ ), 258 ( $\blacklozenge$ ), 132 ( $\triangle$ ), and 76 ( $\blacktriangledown$ ). Dashed line denotes sonic levels for blowing and suction in (a) and (b), respectively.

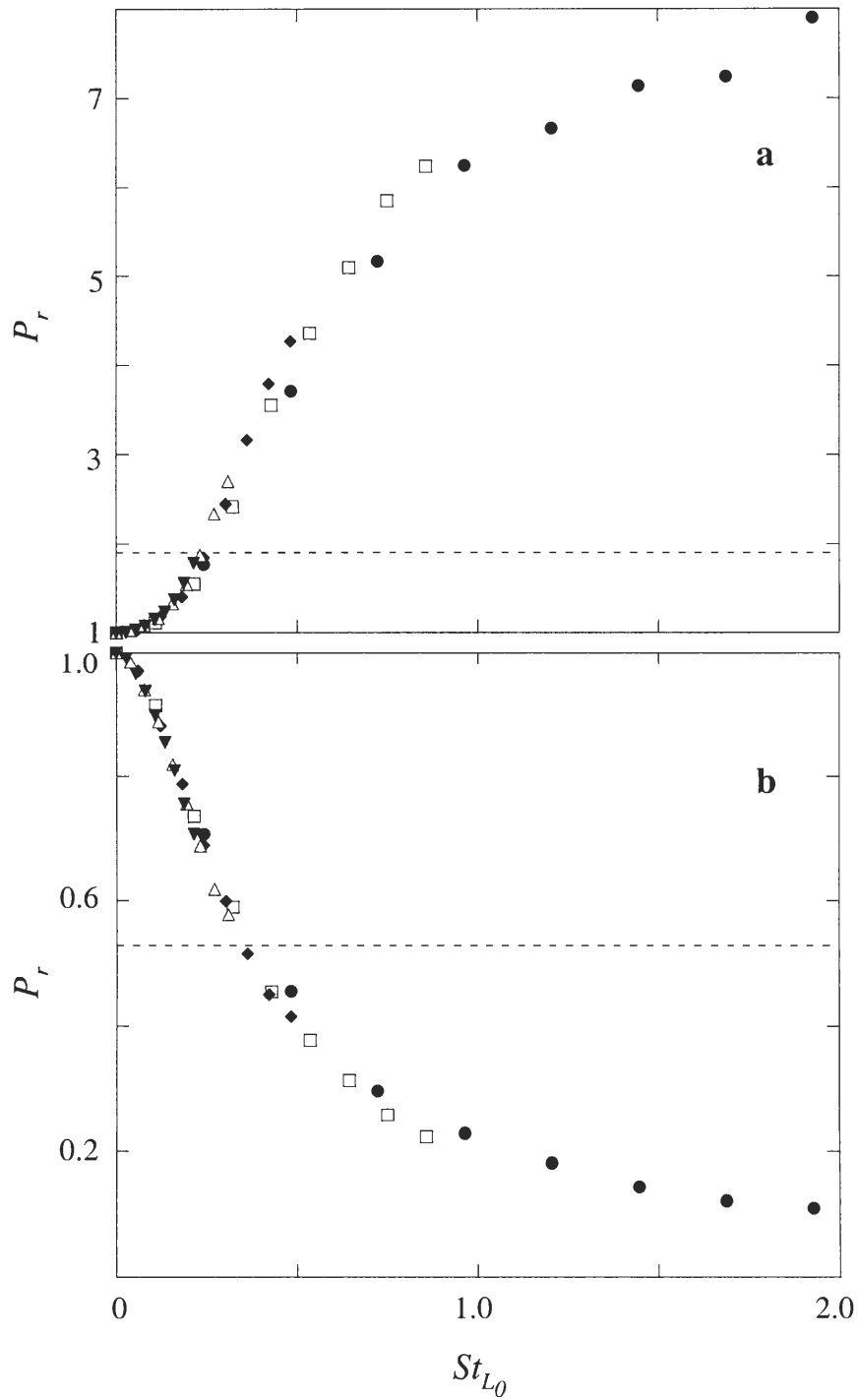


Figure 7. Maximum (a) and minimum (b) pressures over cycle varying  $f$  (normalized as  $St_{L_0}$ ) for  $r = 27.1$  and  $L_0/d = 2065$  ( $\bullet$ ), 612 ( $\square$ ), 258 ( $\blacklozenge$ ), 132 ( $\triangle$ ), and 76 ( $\blacktriangledown$ ). Dashed line denotes sonic levels for blowing and suction in (a) and (b), respectively.

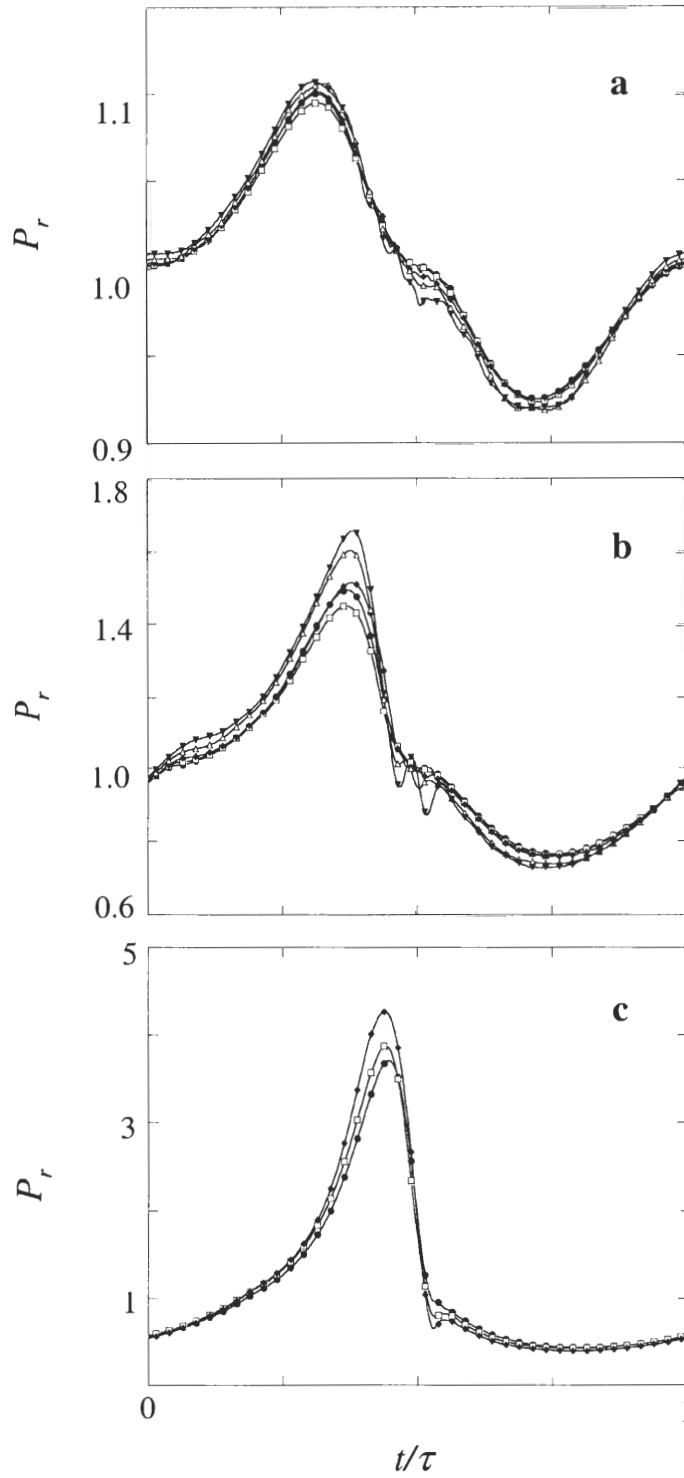


Figure 8. Phase-averaged cylinder pressures over cycle for  $St_{Lo} = 0.1$  (a),  $0.2$  (b), and  $0.48$  (c) for  $r = 27.1$  and  $L_o/d = 2065$  ( $\bullet$ ),  $612$  ( $\square$ ),  $258$  ( $\blacklozenge$ ),  $132$  ( $\triangle$ ), and  $76$  ( $\blacktriangledown$ ).

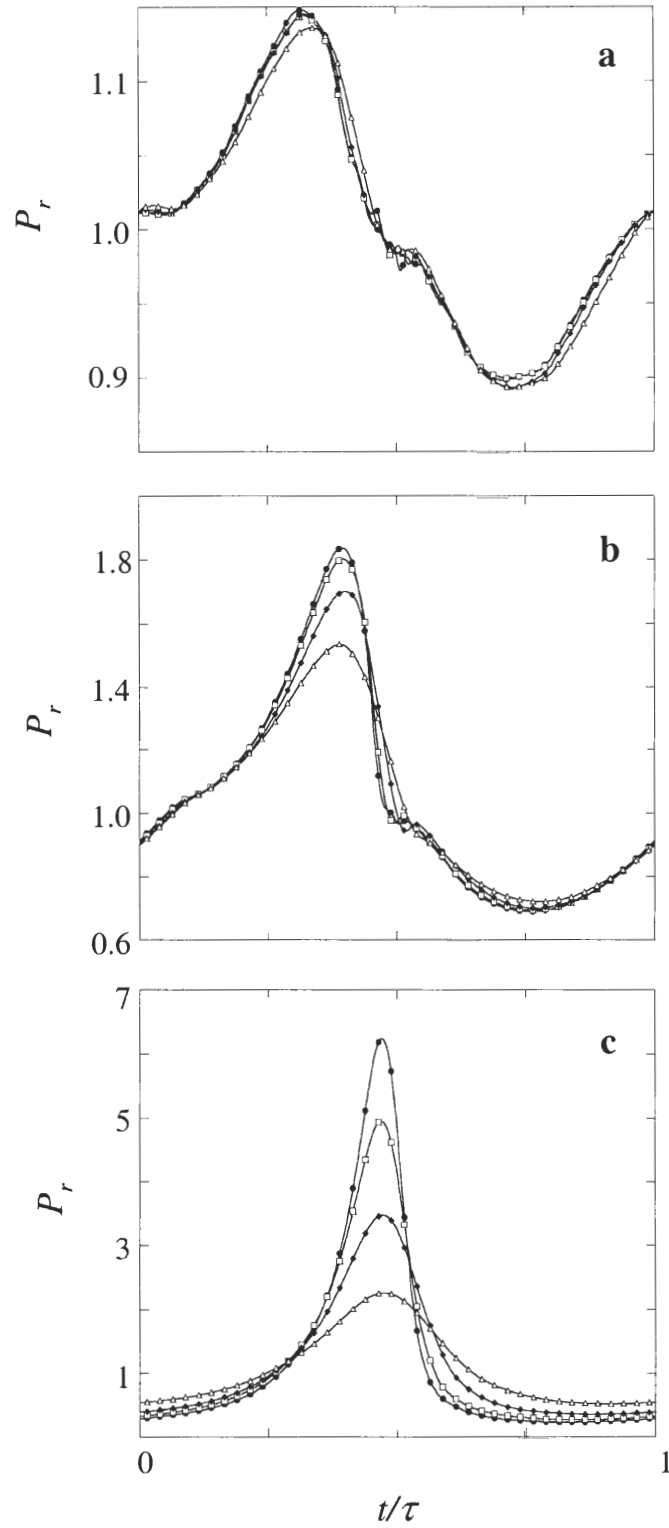


Figure 9. Phase-averaged cylinder pressures over cycle for  $f = 100$  Hz and  $L_0/d = 76$  (a), 258 (b) and 2065 (c) for  $r = 27.1$  ( $\bullet$ ), 14.6 ( $\square$ ), 6.7 ( $\blacklozenge$ ), and 3.2 ( $\triangle$ ).

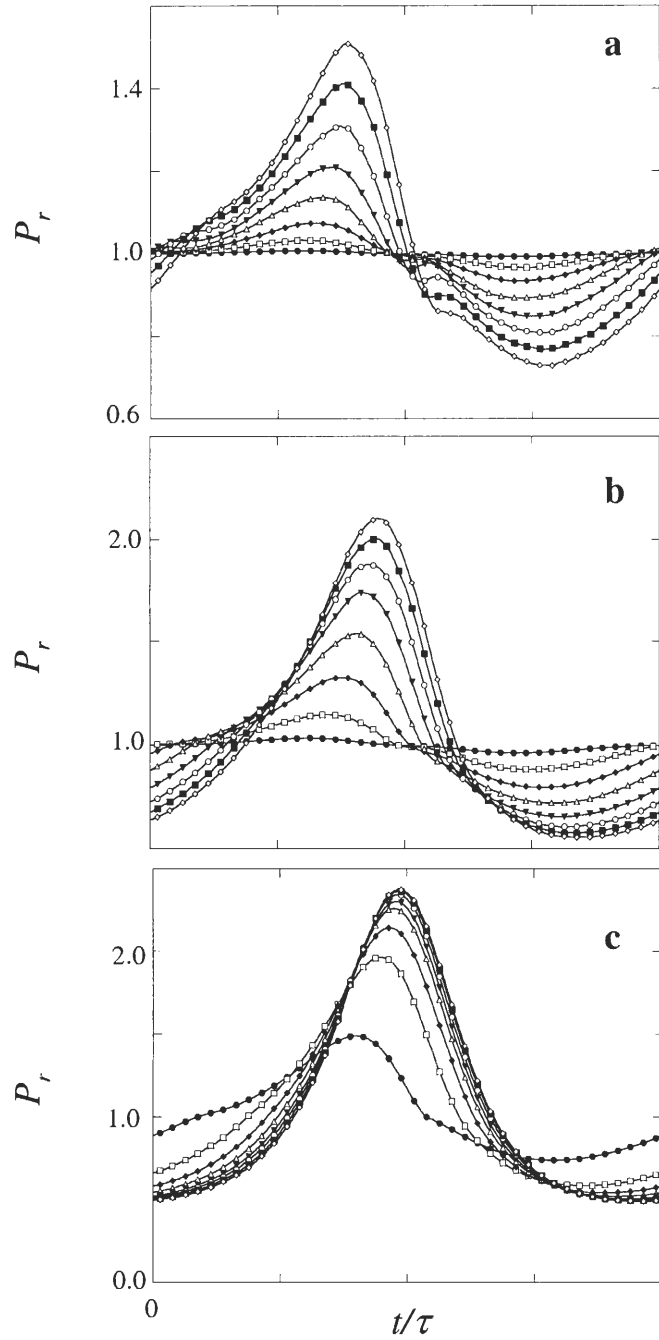


Figure 10. Phase-averaged cylinder pressures over cycle for  $r = 3.2$  and  $L_0/d = 76$  (a), 258 (b), and 2065 (c) for  $f = 25$  ( $\bullet$ ), 50 ( $\square$ ), 75 ( $\blacklozenge$ ), 100 ( $\triangle$ ), 125 ( $\blacktriangledown$ ), 150 ( $\circ$ ), 175 ( $\blacksquare$ ), and 200 ( $\diamond$ ) Hz.

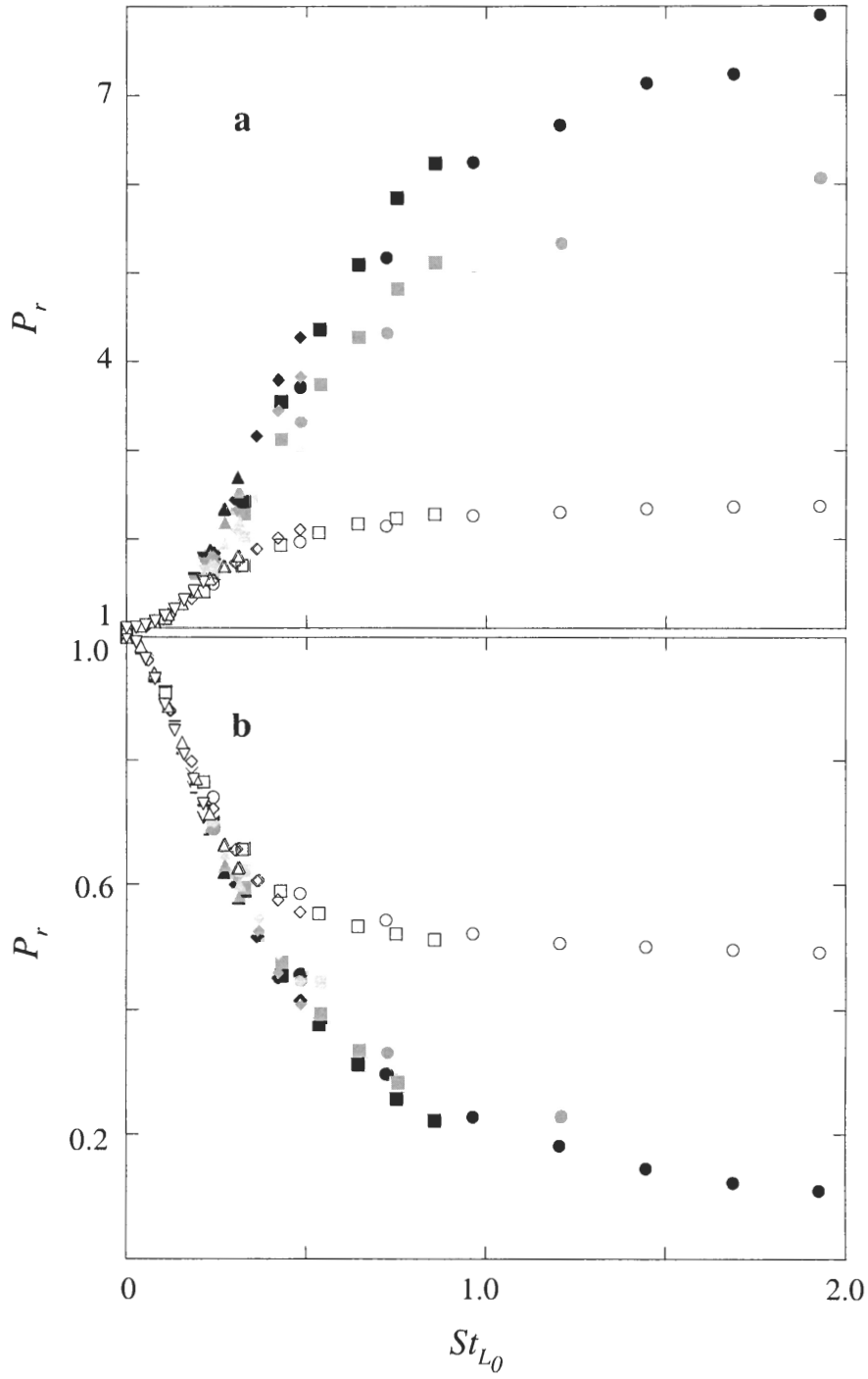


Figure 11. Maximum (a) and minimum (b) pressures over the cycle varying  $f$  (normalized as  $St_{L_0}$ ) for  $L_0/d = 2065$  ( $\bullet$ ), 612 ( $\square$ ), 258 ( $\blacklozenge$ ), 132 ( $\triangle$ ), and 76 ( $\blacktriangledown$ ), and  $r = 27.1$  (black), 14.6 (dark gray), 6.7 (light gray), and 3.2 (open).



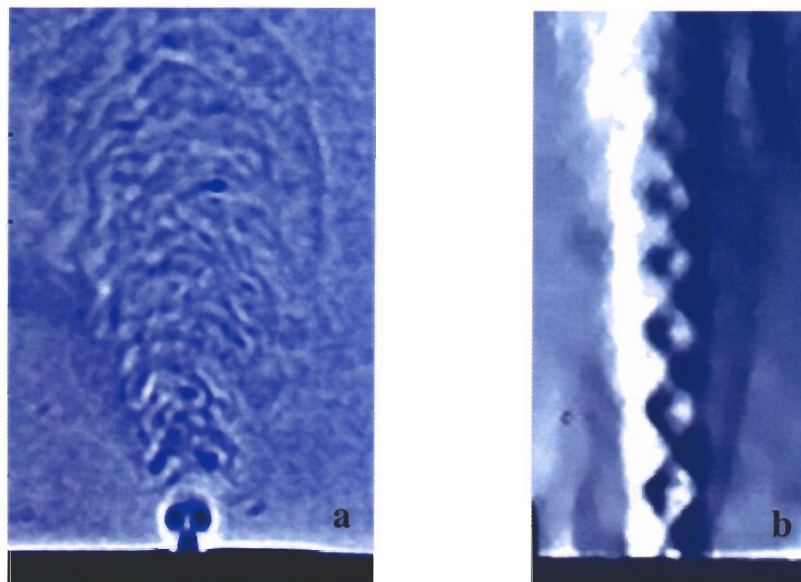


Figure 12. Schlieren images from conventional synthetic jet (a - driven by piezoelectric membrane,  $f \approx 1$  kHz), and compressible synthetic jet (b -  $L_0/d = 612$ ,  $r = 27.1$ ,  $f = 120$  Hz). (Image a) courtesy of Smith and Glezer, 1998.)

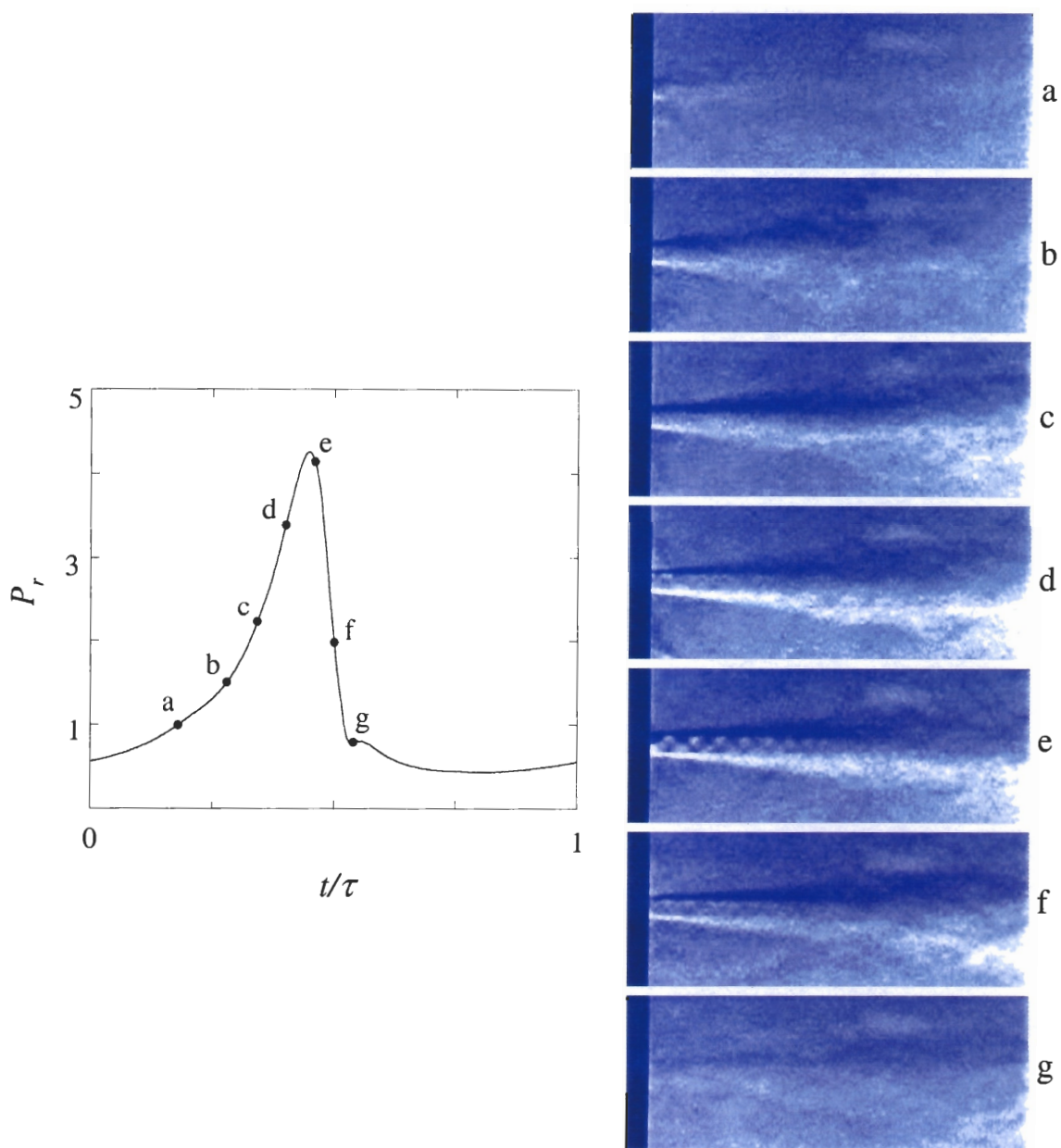


Figure 13. Cylinder pressure over cycle and phase-locked Schlieren images of blowing jet for  $r = 27.1$ ,  $L_0/d = 612$ , and  $f = 120$  Hz for  $t/\tau = 0.18$  (a), 0.28 (b), 0.34 (c), 0.40 (d), 0.46 (e), 0.50 (f), and 0.54 (g).

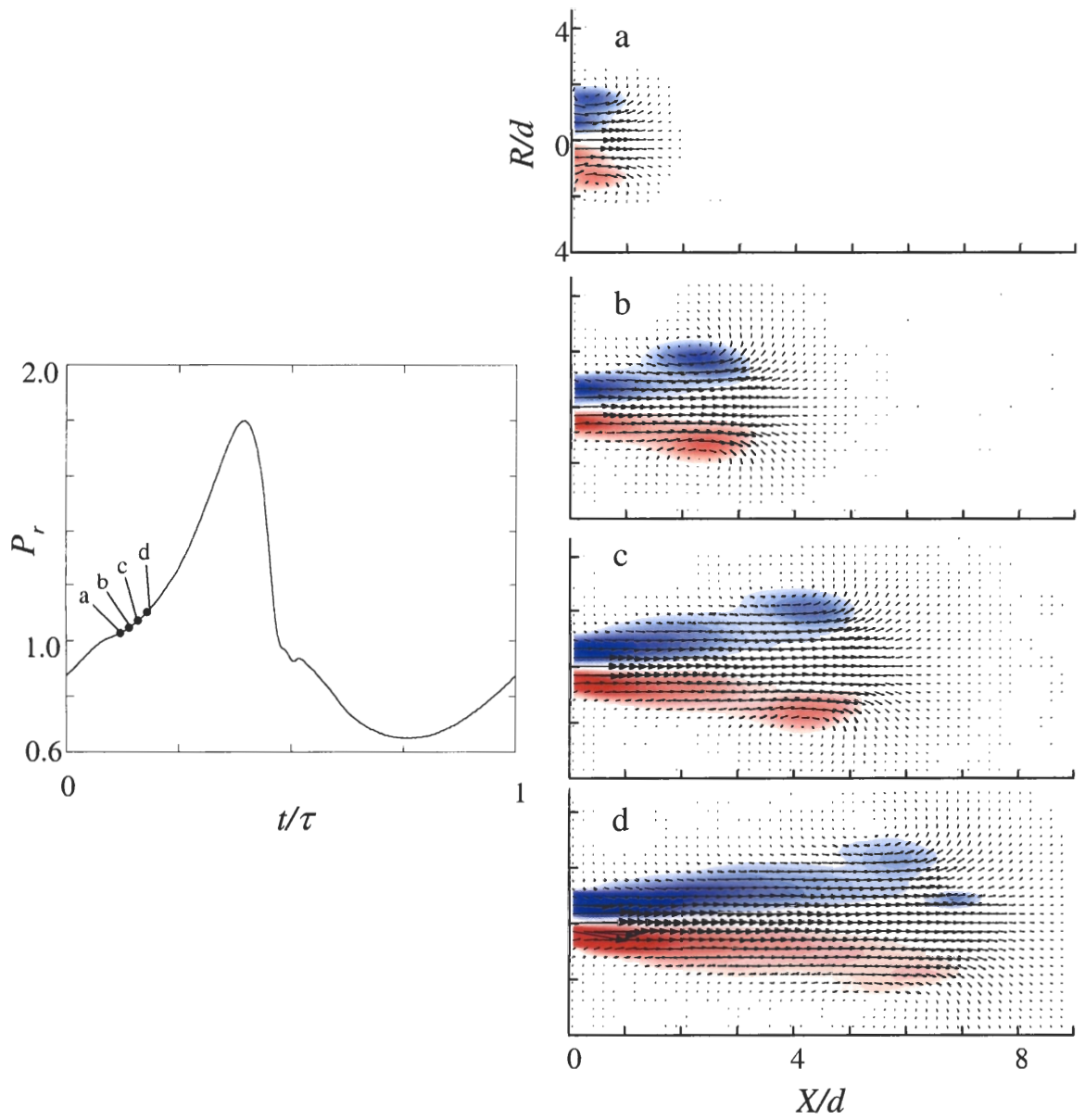


Figure 14. Cylinder pressure over cycle with PIV velocity vectors and vorticity contours for initial blowing for  $r = 27.1$ ,  $L_\phi/d = 258$ , and  $f = 100$  Hz at  $t/\tau = 0.12$  (a),  $0.14$  (b),  $0.16$  (c), and  $0.18$  (d).

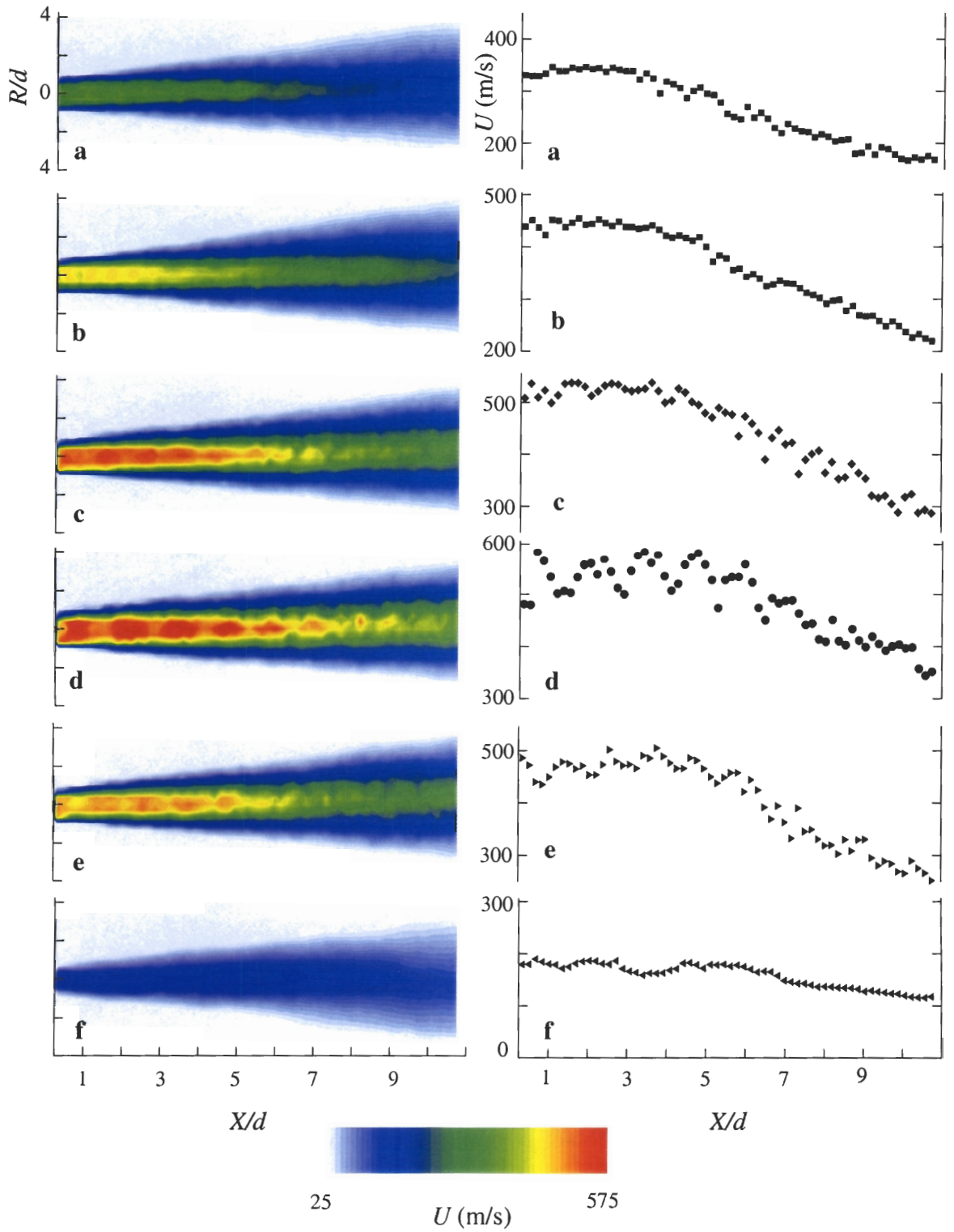


Figure 15. PIV streamwise velocity contours and centerline velocity data for  $r = 27.1$ ,  $L_0/d = 612$ , and  $f = 100$  Hz at  $t/\tau = 0.30$  (a),  $0.34$  (b),  $0.38$  (c),  $0.42$  (d),  $0.46$  (e), and  $0.50$  (f).

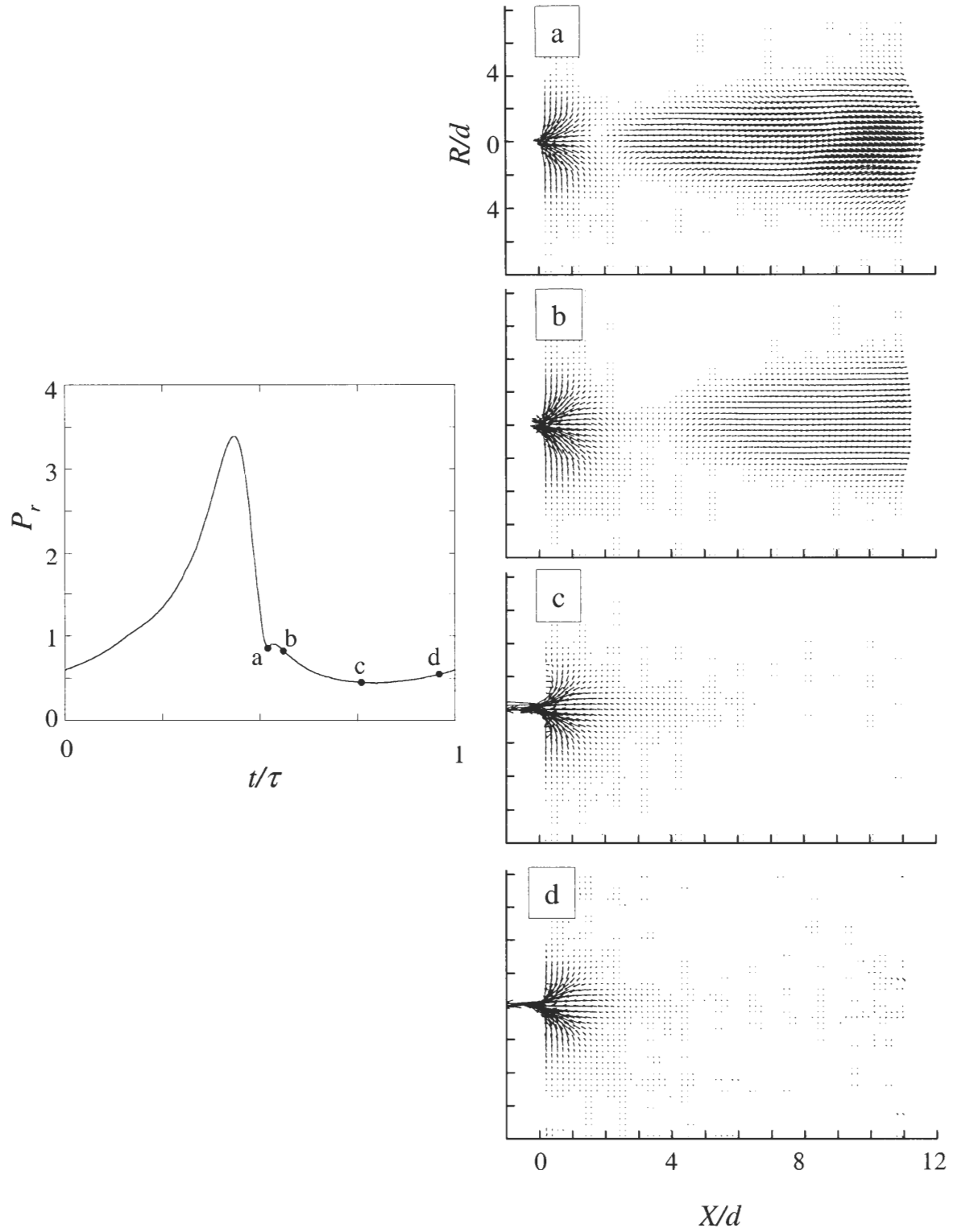


Figure 16. Cylinder pressure over cycle with sample PIV velocity vector fields over suction phase for  $r = 27.1$ ,  $L_0/d = 612$ , and  $f = 100$  Hz at  $t/\tau = 0.52$  (a),  $0.56$  (b),  $0.76$  (c), and  $0.96$  (d).

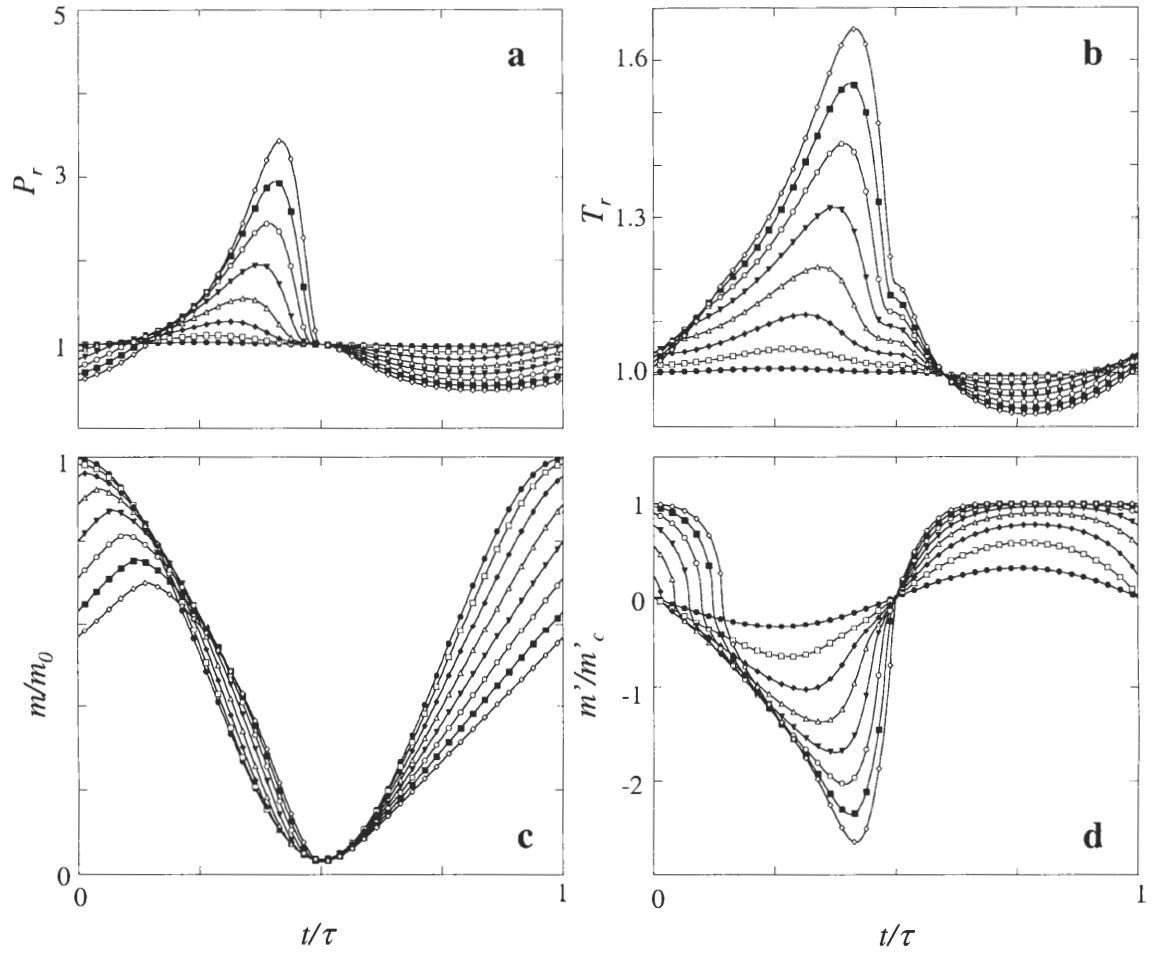


Figure 17. Simulation results for cylinder pressure (a), temperature (b), mass (c), and mass flux through orifice (d) for  $r = 27.1$  and  $L_o/d = 258$  for  $f = 25$  ( $\bullet$ ), 50 ( $\square$ ), 75 ( $\blacklozenge$ ), 100 ( $\Delta$ ), 125 ( $\blacktriangledown$ ), 150 ( $\circ$ ), 175 ( $\blacksquare$ ), and 200 ( $\diamond$ ) Hz.

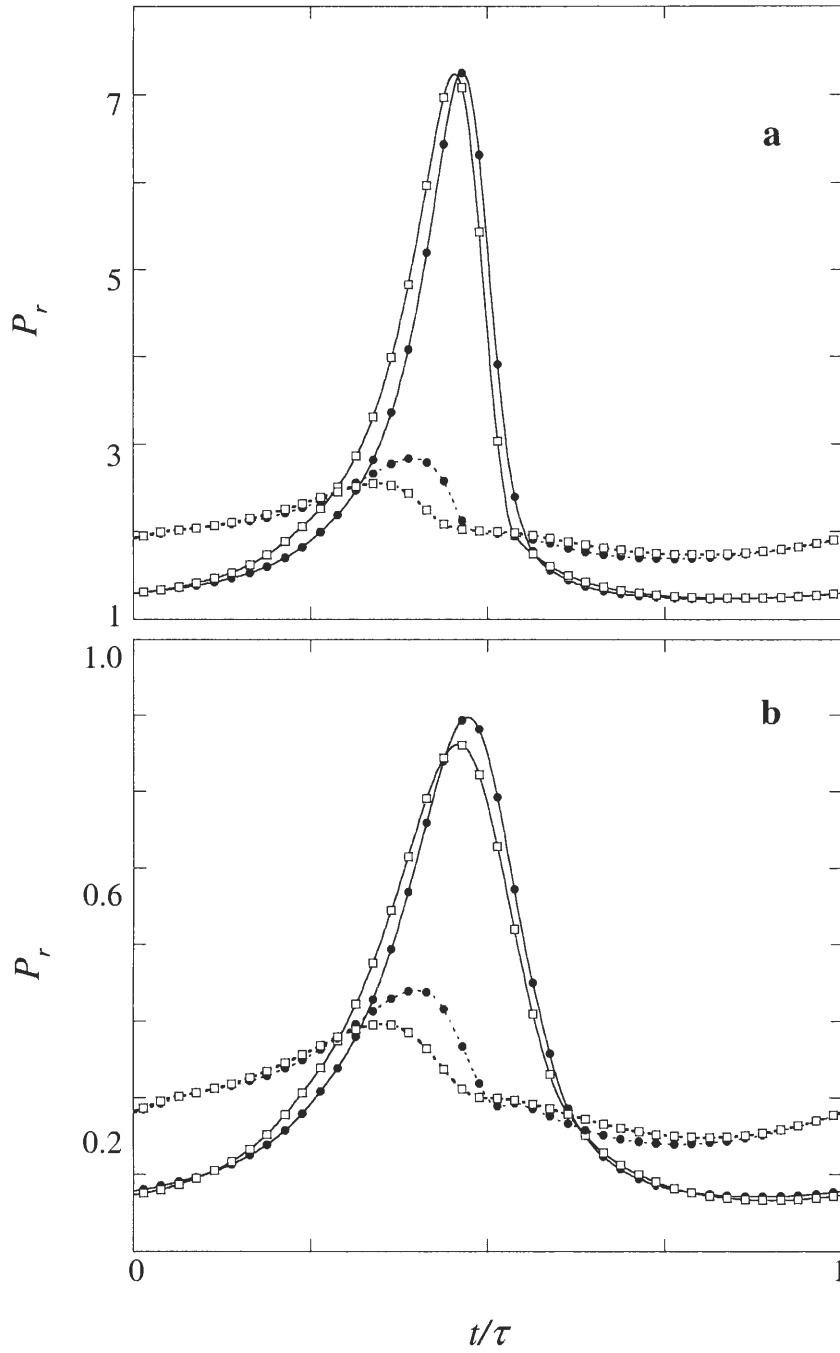


Figure 18. Experimental phase-averaged cylinder pressures ( $\bullet$ ) compared to numerical simulation pressure ( $\square$ ) over cycle for  $f = 100$  Hz and  $r = 27.1$  (a) and  $6.7$  (b) with  $L_0/d = 2065$  (solid line) and  $258$  (dashed line).

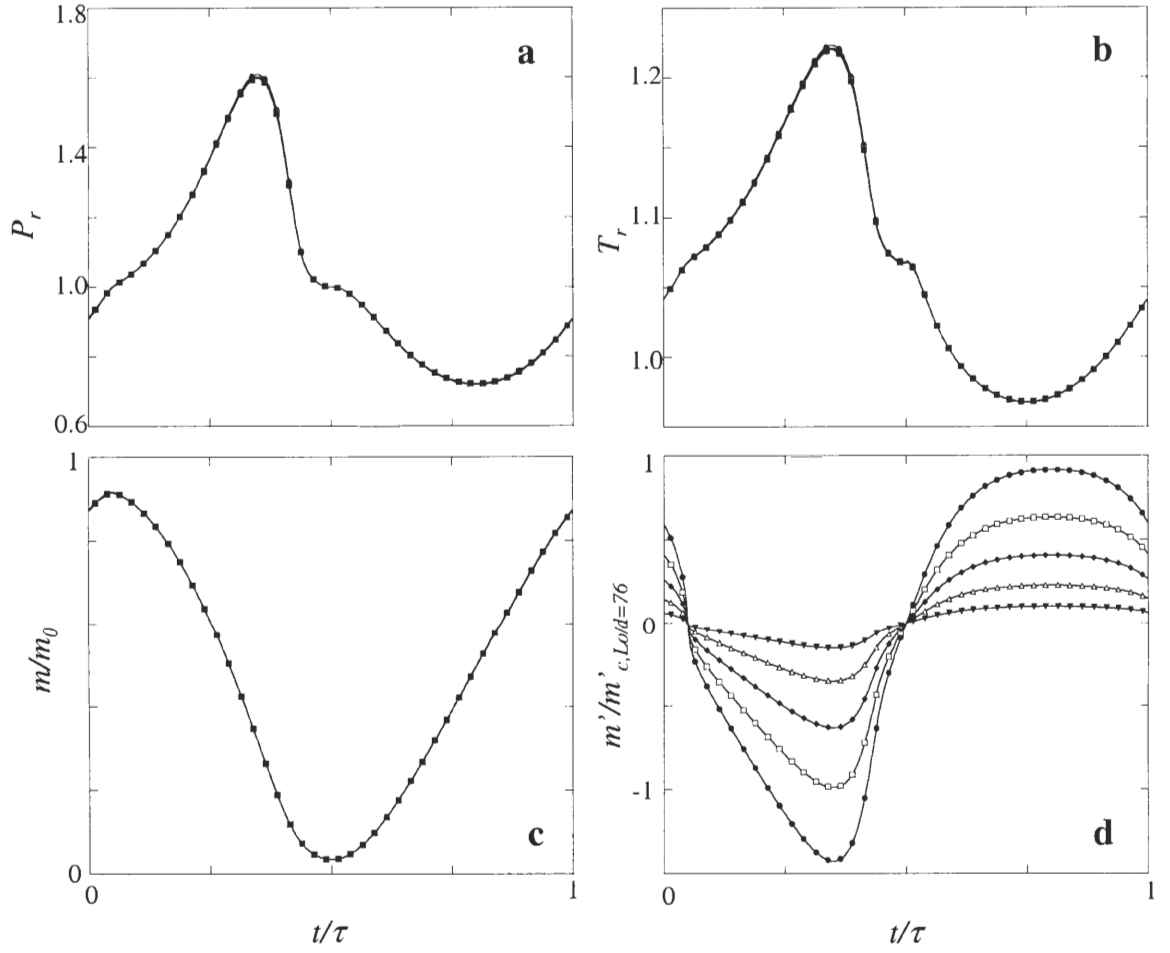


Figure 19. Simulation results for cylinder pressure (a), temperature (b), mass (c), and mass flux through orifice (d) for  $r = 27.1$  and  $St_{Lo} = 0.25$  for  $L_o/d = 76$  (●), 132 (□), 256 (◆), 612 (Δ), and 2065 (▼).



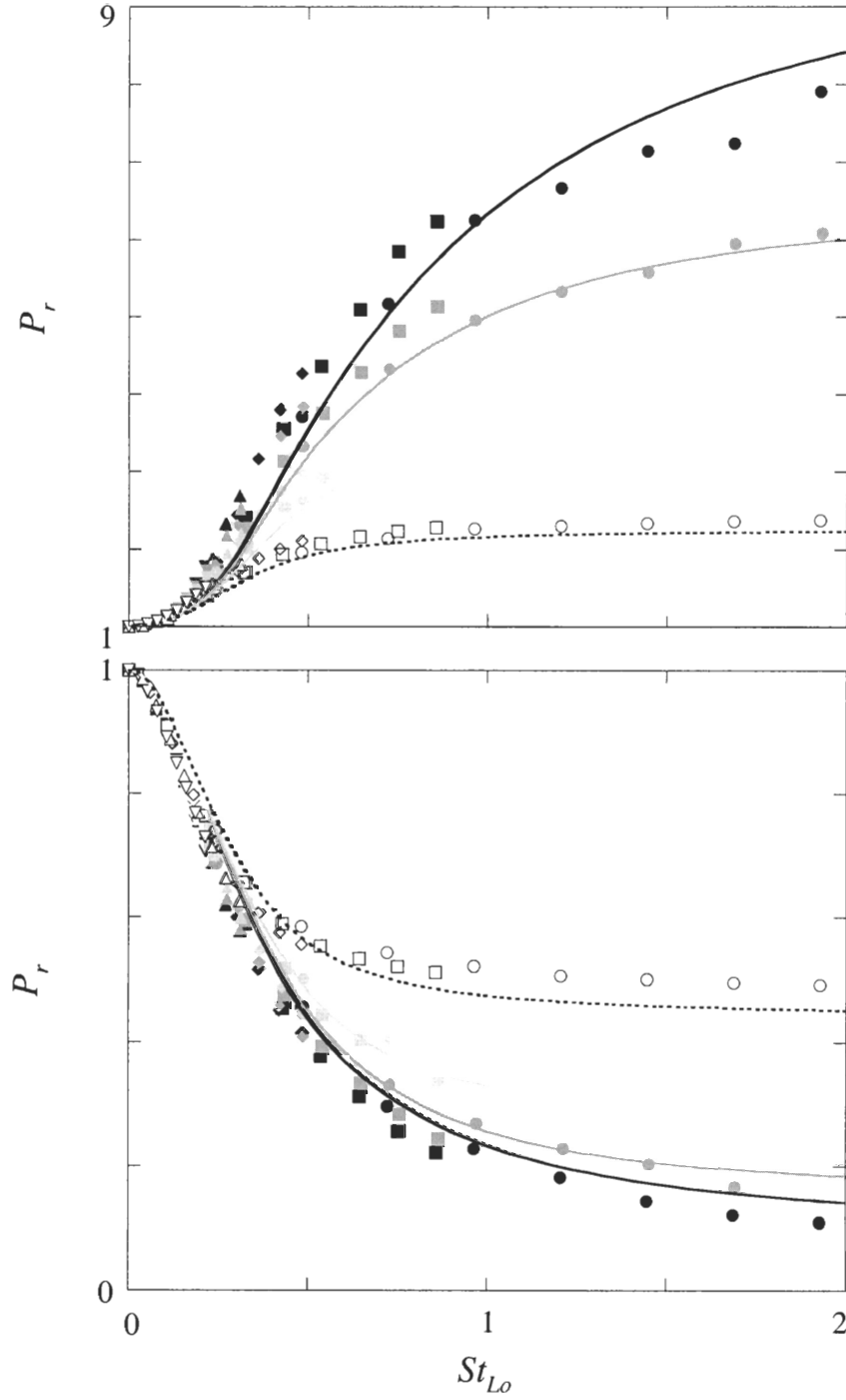


Figure 20. Maximum (a) and minimum (b) pressures over cycle varying  $f$  (normalized as  $St_{Lo}$ ) for  $L_0/d = 2065$  (●), 612 (□), 258 (◆), 132 (Δ), and 76 (▼), and  $r = 27.1$  (black), 14.6 (dark gray), 6.7 (light gray), and 3.2 (open), with lines denoting simulation results.

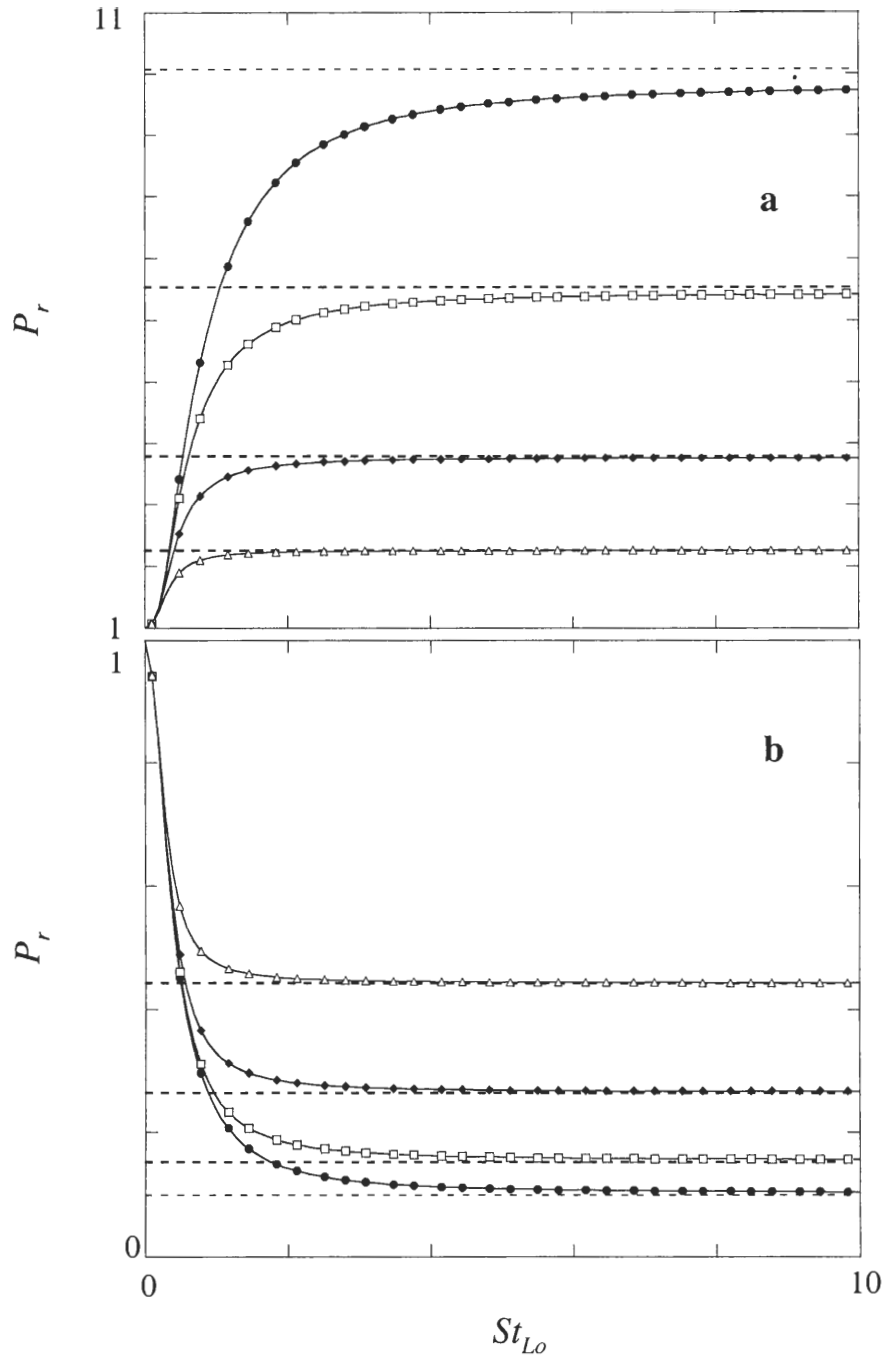


Figure 21. Maximum (a) and minimum (b) pressures over cycle from simulation varying  $f$  (normalized as  $St_{Lo}$ ) for  $r = 27.1$  ( $\bullet$ ),  $14.6$  ( $\square$ ),  $6.7$  ( $\blacklozenge$ ), and  $3.2$  ( $\triangle$ ) (with  $r^{\gamma/2}$  and  $r^{-\gamma/2}$  denoted with dashed lines in (a) and (b), respectively).

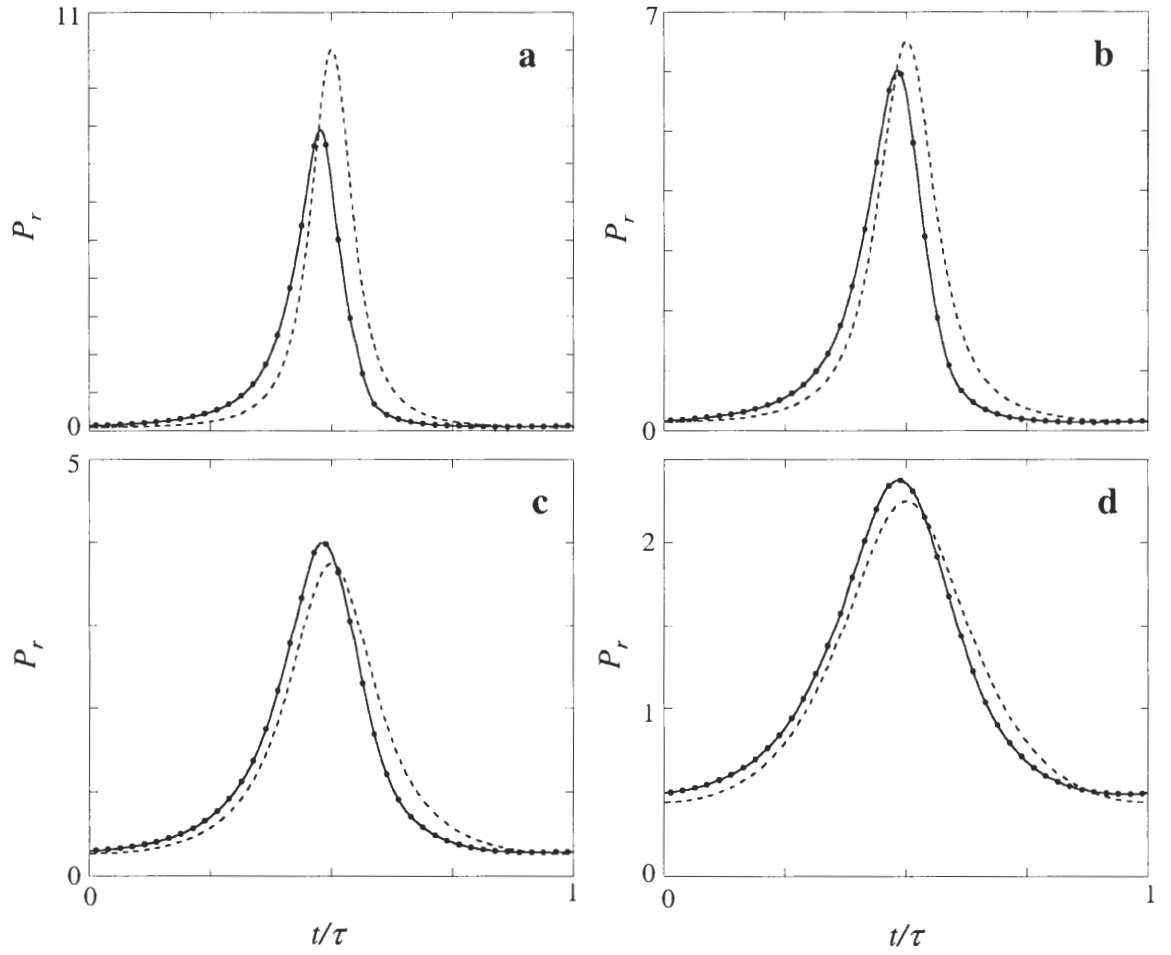


Figure 22. Phase-averaged cylinder pressures for  $L_0/d = 2065$  and  $f = 200$  Hz (●) with isentropic closed system pressure (dashed) over cycle for  $r = 27.1$  (a), 14.6 (b), 6.7 (c), and 3.2 (d).

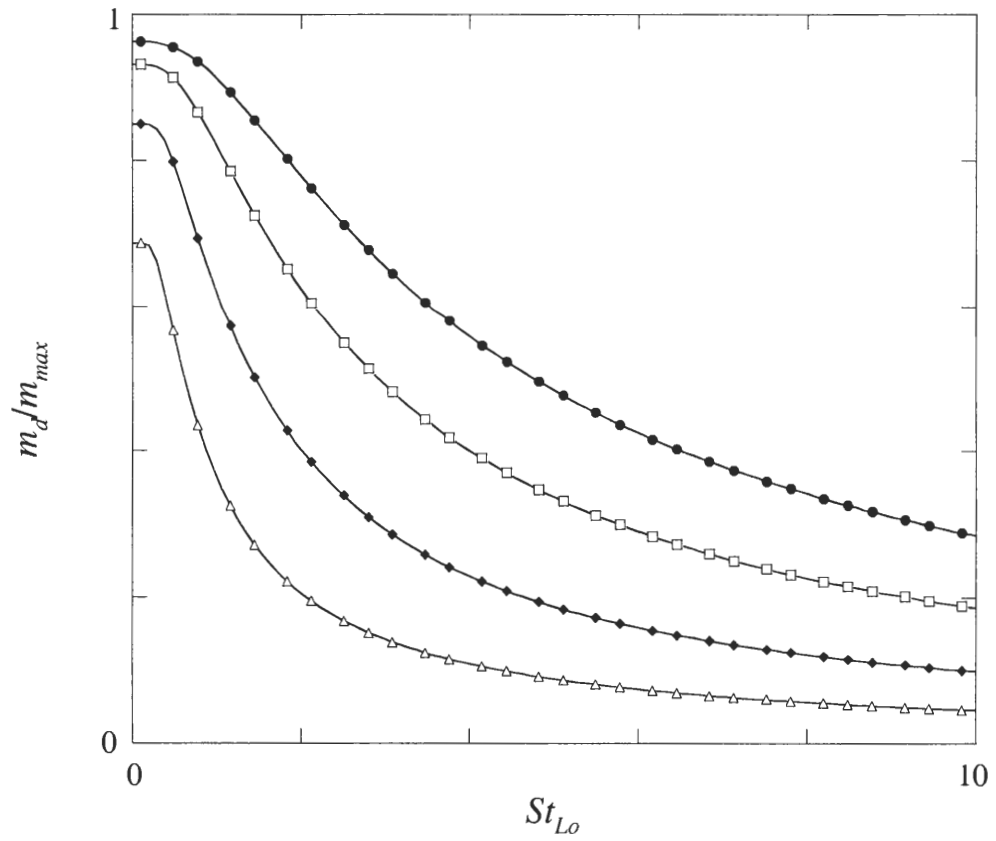


Figure 23. Simulation results for mass displacement over cycle varying  $f$  (normalized as  $St_{Lo}$ ) for  $r = 27.1$  (●), 14.6 (□), 6.7 (◆), and 3.2 (Δ).

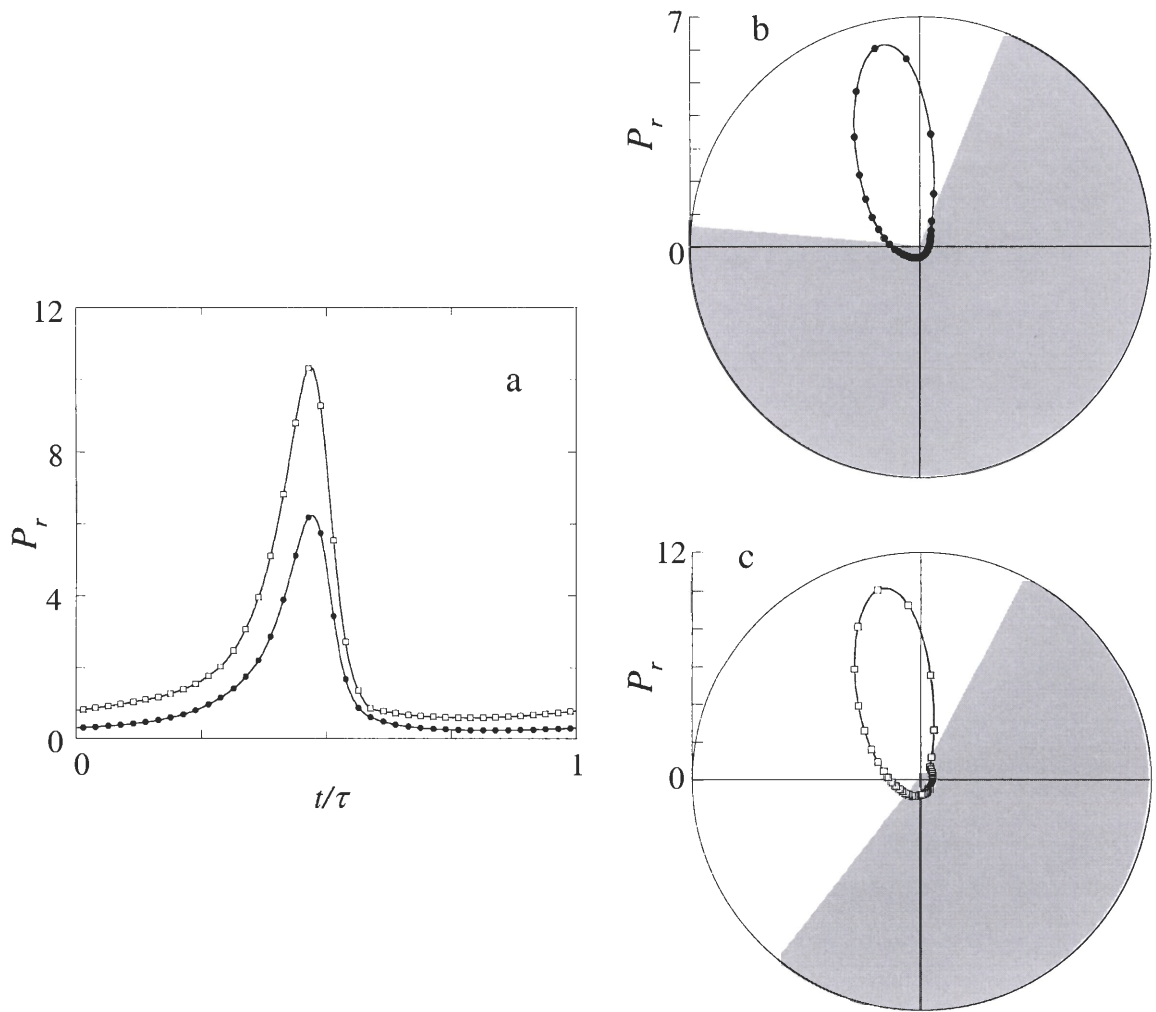


Figure 24. Phase-averaged cylinder pressure over cycle for  $r = 27.1$ ,  $L_0/d = 612$ , and  $f = 100$  Hz for unvalved ( $\bullet$ ) and valved ( $\square$ ) cylinder head in rectangular coordinates (a) and polar coordinates (b and c) with suction cycle shaded.

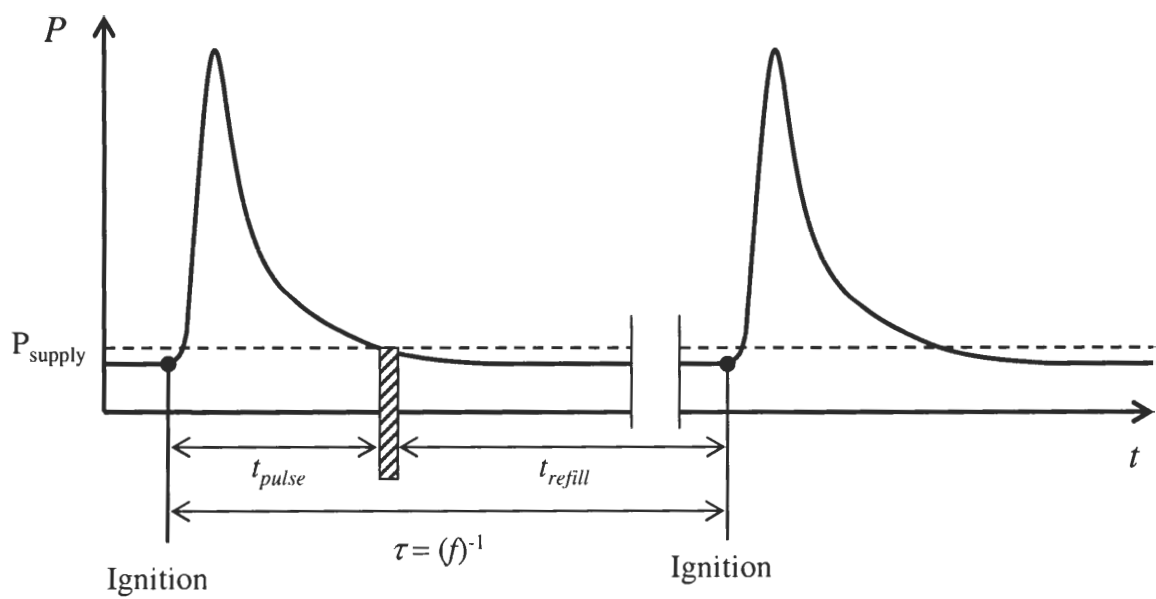


Figure 25. Conceptual pressure-time history for combustion-driven jet actuator.

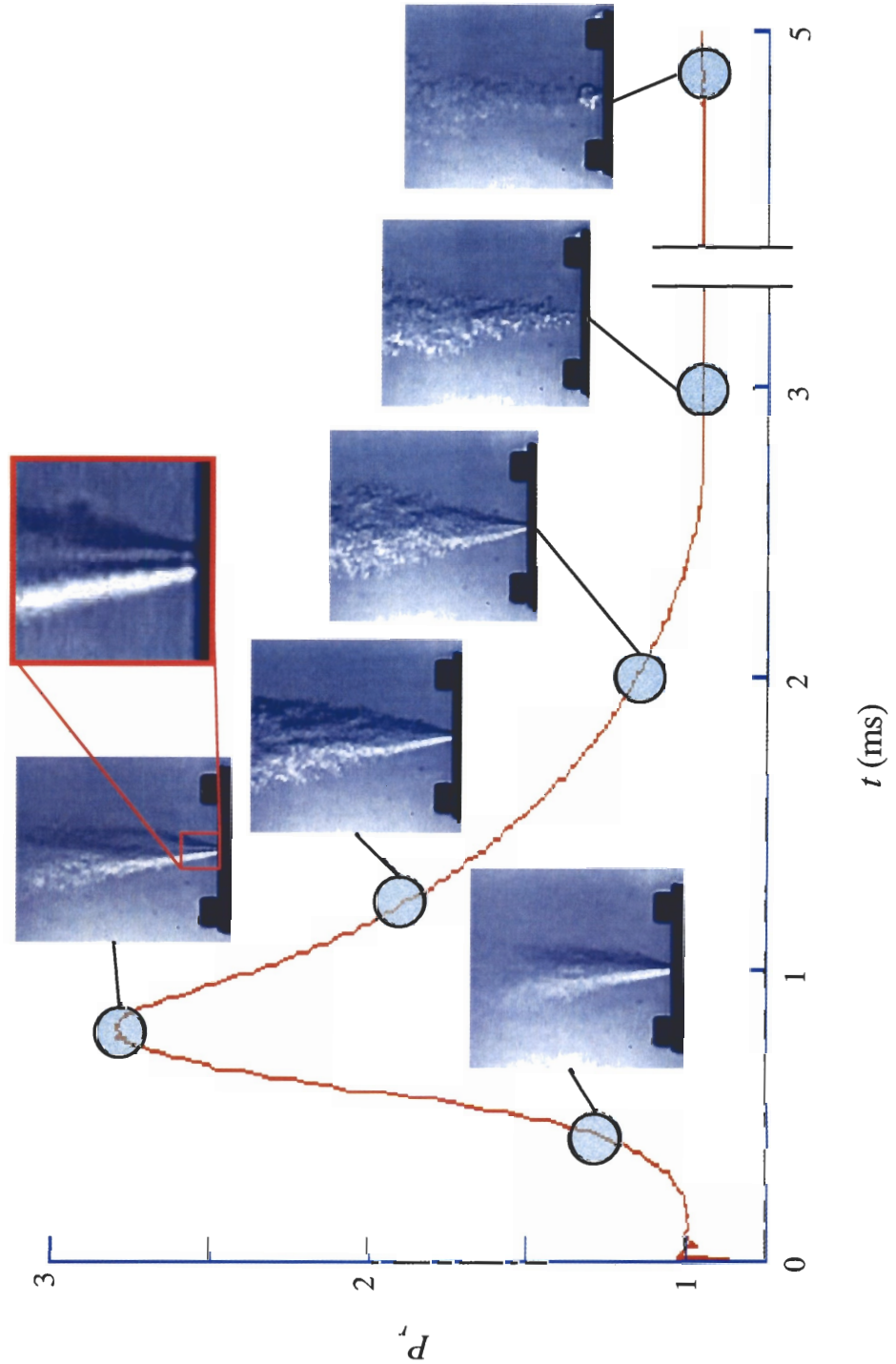


Figure 26. Phase-averaged combustor pressure and a sequence of phase-locked Schlieren images of the exhaust jet ( $V = 1$  cc,  $H/D = 1.27$ , hydrogen-air ( $\Phi = 0.7$ ),  $d = 1.30$  mm,  $Q = 50$  cc/s, and  $f = 30$  Hz)

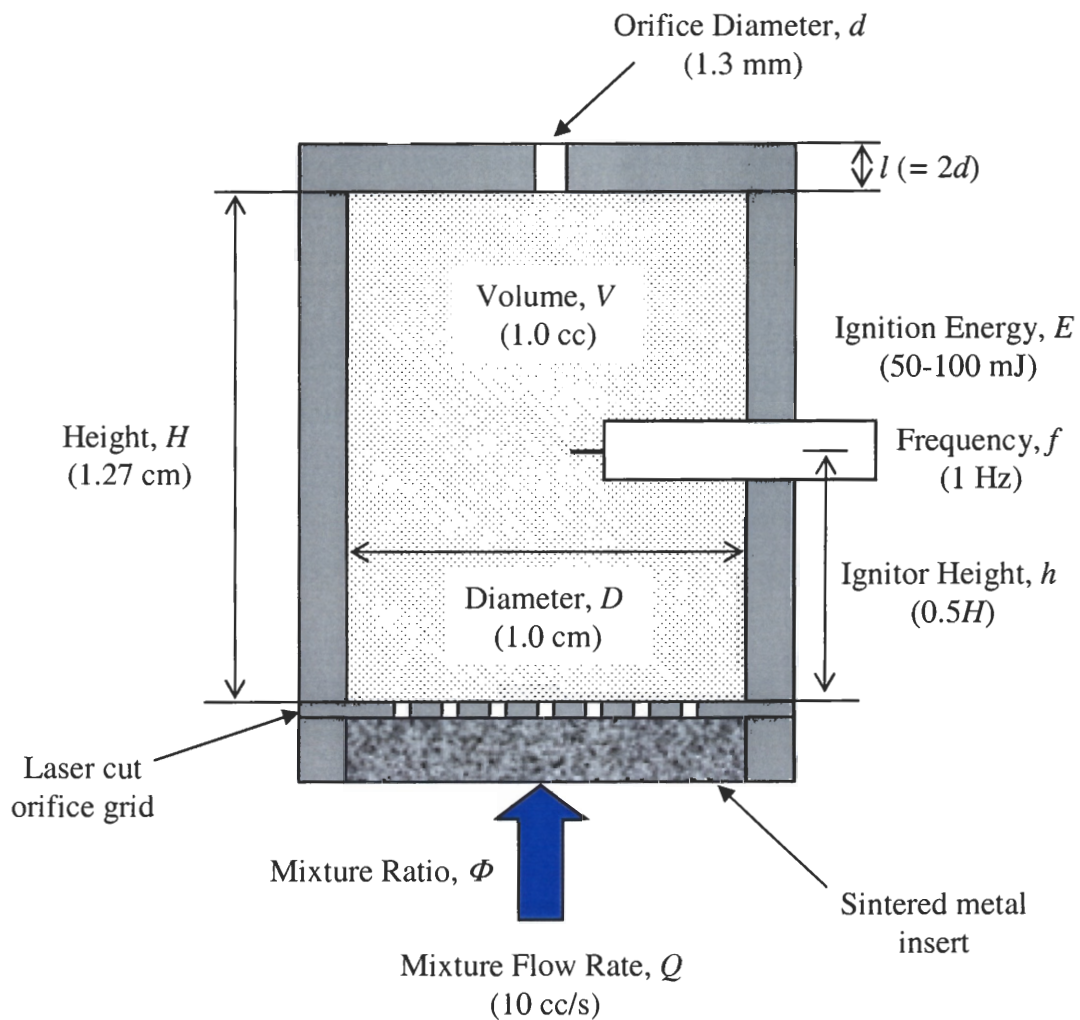


Figure 27. Schematic diagram of parametric test chamber for combustion actuator. Baseline values are denoted in parentheses.



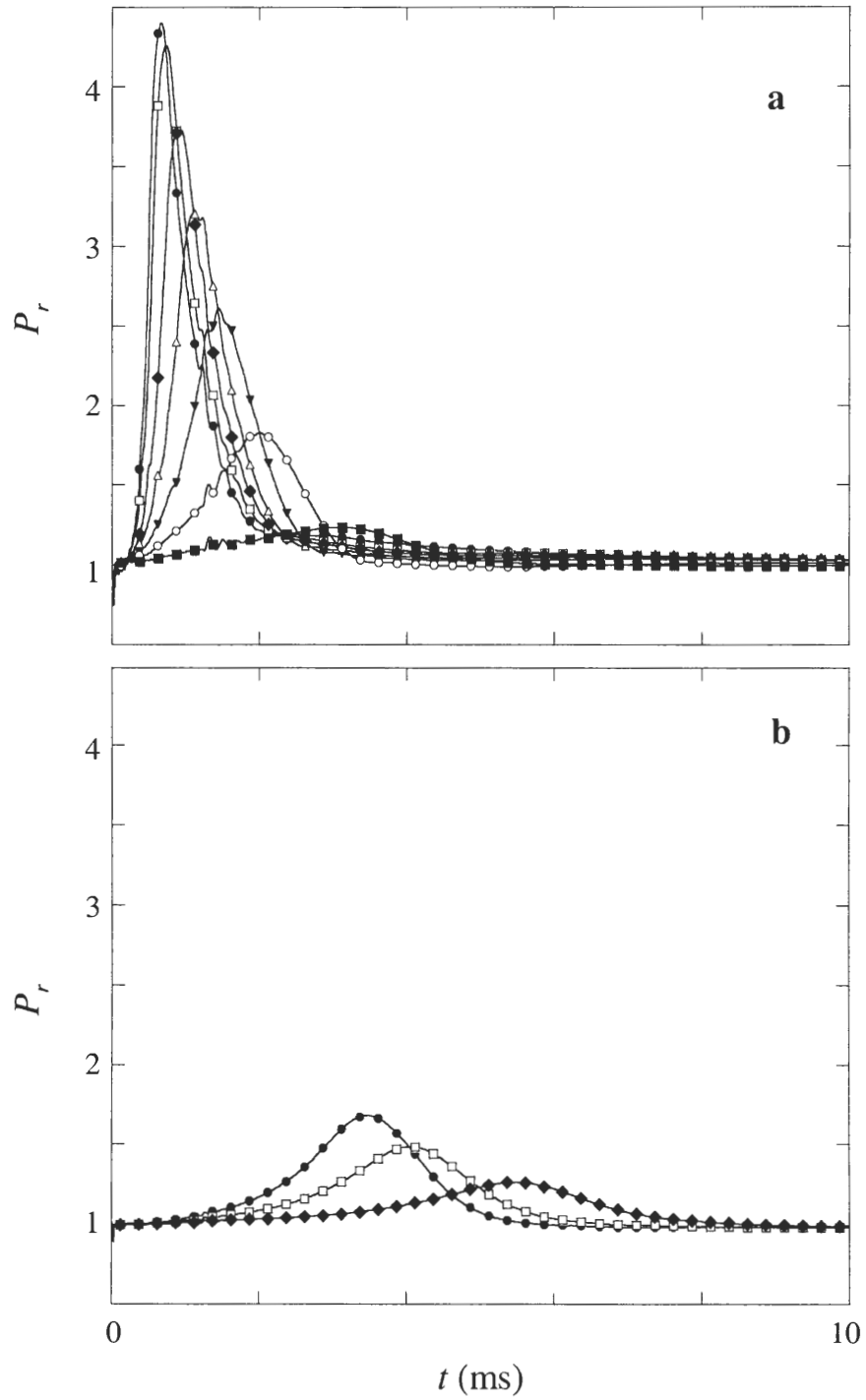


Figure 28. Phase-averaged combustor pressure for  $d = 1.30$  mm for hydrogen (a) and propane (b) with  $\Phi = 1.0$  ( $\bullet$ ),  $0.9$  ( $\square$ ),  $0.8$  ( $\blacklozenge$ ),  $0.7$  ( $\triangle$ ),  $0.6$  ( $\blacktriangledown$ ),  $0.5$  ( $\circ$ ), and  $0.4$  ( $\blacksquare$ ).

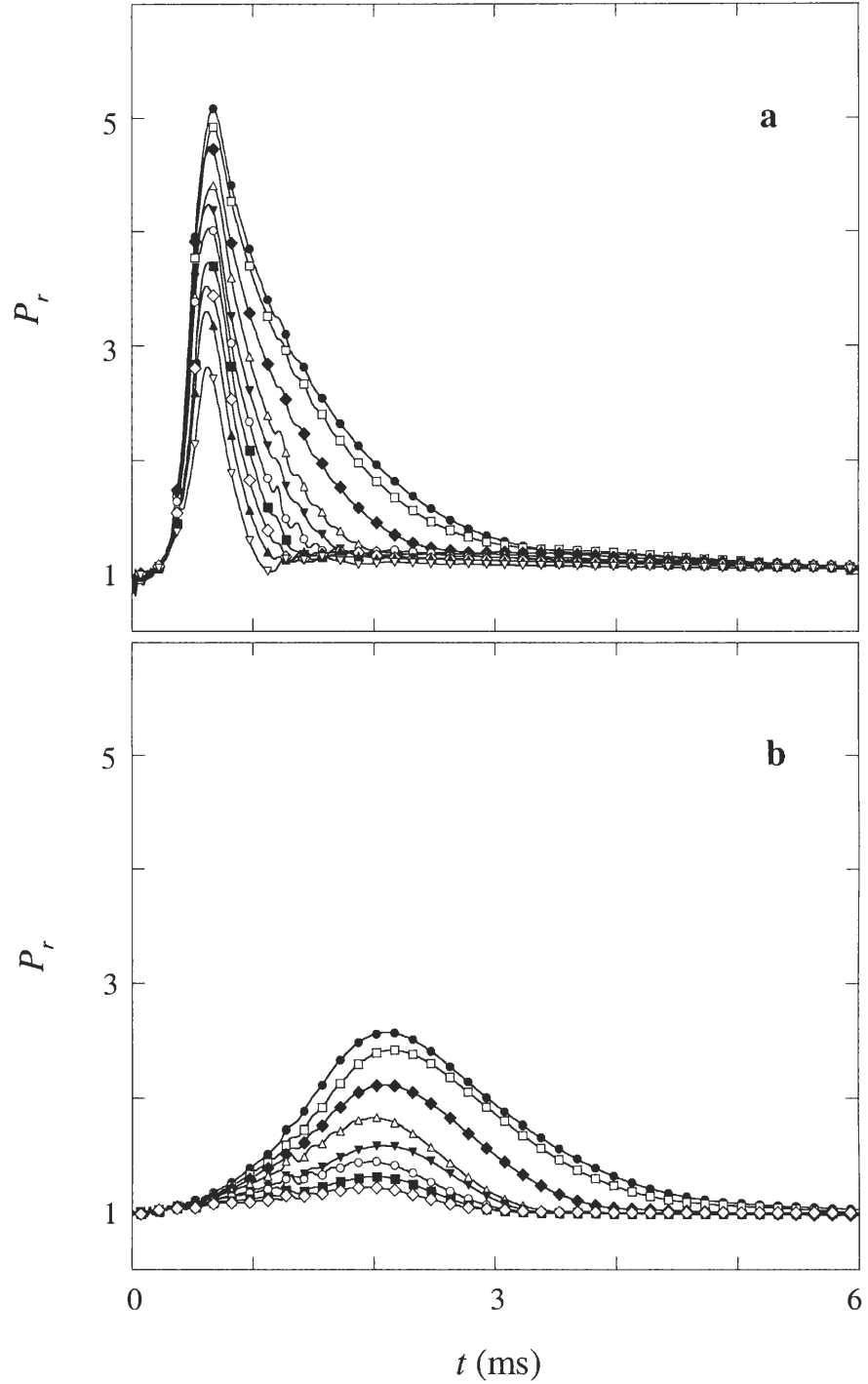


Figure 29. Phase-averaged combustor pressures for hydrogen with  $\Phi = 1.0$  (a) and  $0.5$  (b) for  $d = 0.79$  ( $\bullet$ ),  $0.89$  ( $\square$ ),  $1.09$  ( $\blacklozenge$ ),  $1.30$  ( $\triangle$ ),  $1.50$  ( $\blacktriangledown$ ),  $1.63$  ( $\circ$ ),  $1.78$  ( $\blacksquare$ ),  $1.98$  ( $\diamond$ ),  $2.21$  ( $\blacktriangle$ ), and  $2.50$  ( $\nabla$ ) mm.

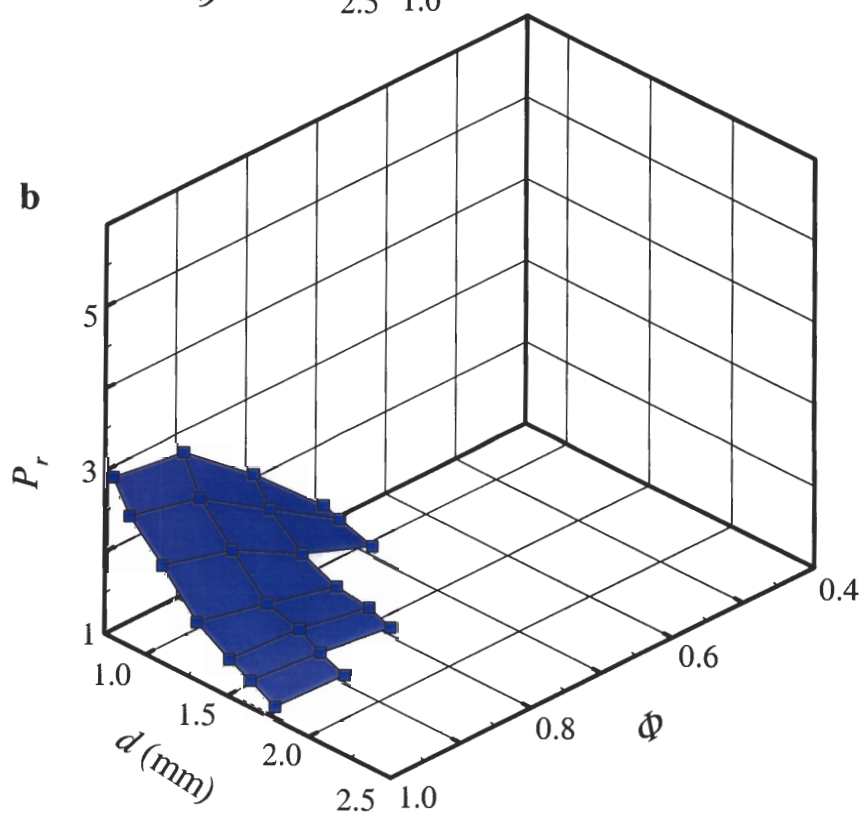
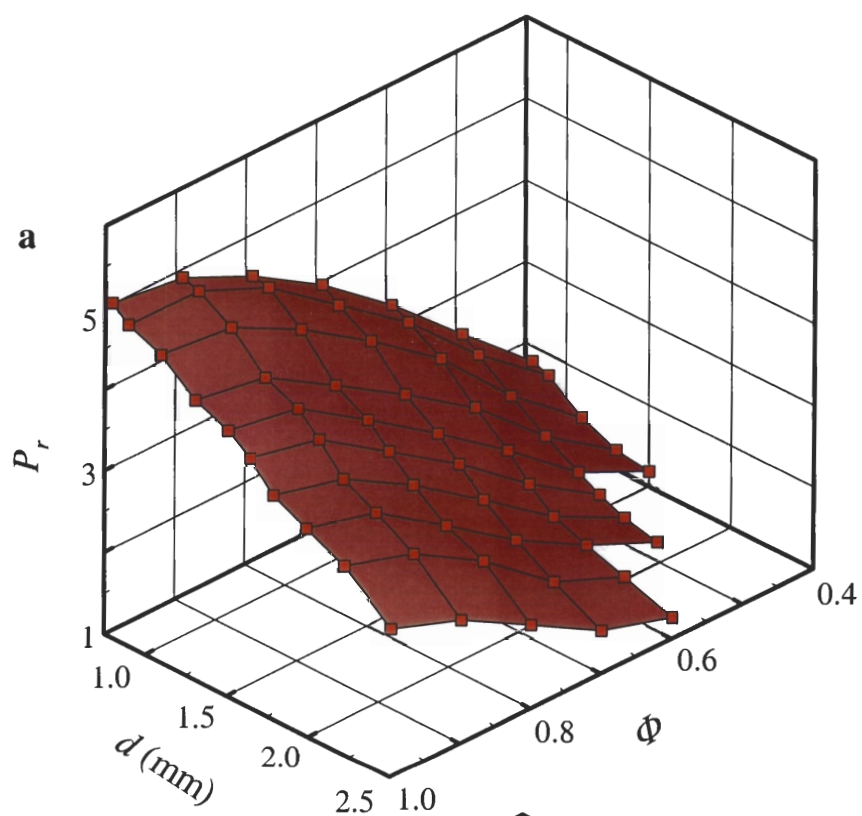


Figure 30. Surface plots of variation of the phase-averaged peak pressure with  $\Phi$  and  $d$  for hydrogen (a) and propane (b).

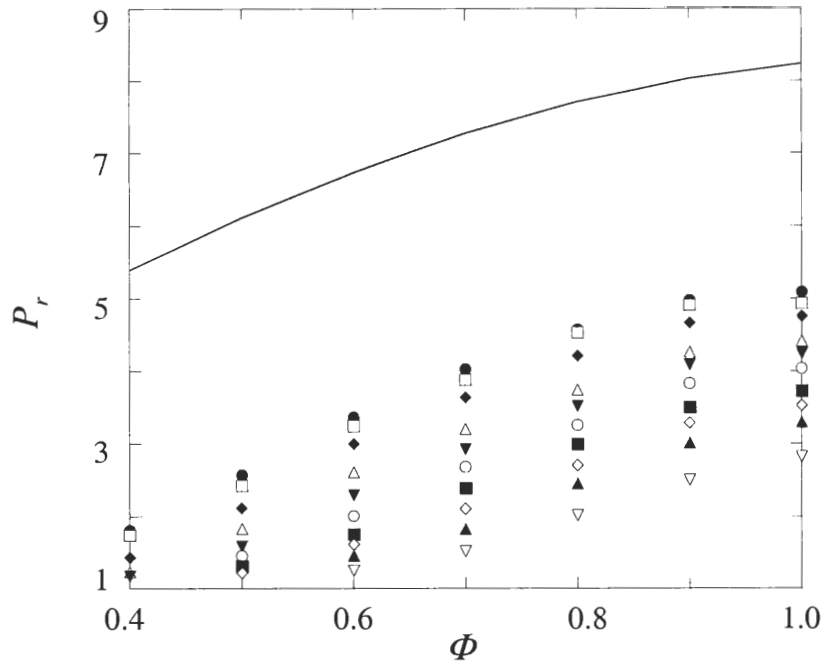


Figure 31. Variation of the phase-averaged peak pressures with  $\Phi$  for hydrogen for  $d = 0.79$  ( $\bullet$ ),  $0.89$  ( $\square$ ),  $1.09$  ( $\blacklozenge$ ),  $1.30$  ( $\triangle$ ),  $1.50$  ( $\blacktriangledown$ ),  $1.63$  ( $\circ$ ),  $1.78$  ( $\blacksquare$ ),  $1.98$  ( $\diamond$ ),  $2.21$  ( $\blacktriangle$ ), and  $2.50$  ( $\nabla$ ) mm. The solid line is the idealized constant volume pressure.

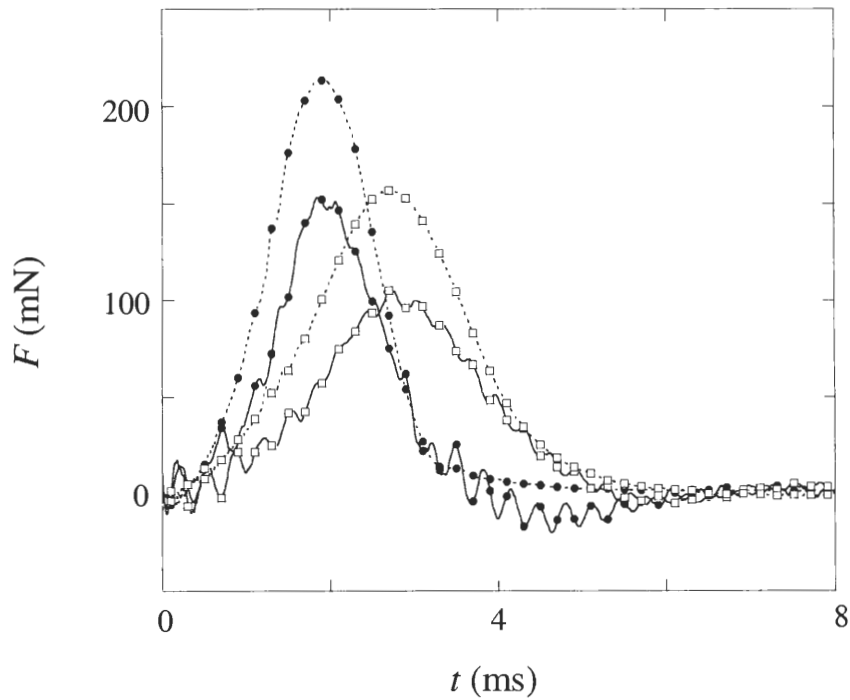


Figure 32. Comparison of the phase-averaged measured (solid line) and computed (from pressure values - dashed line) thrust with  $d = 1.30$  mm for hydrogen with  $\Phi = 0.6$  ( $\bullet$ ) and propane with  $\Phi = 1.0$  ( $\square$ ).

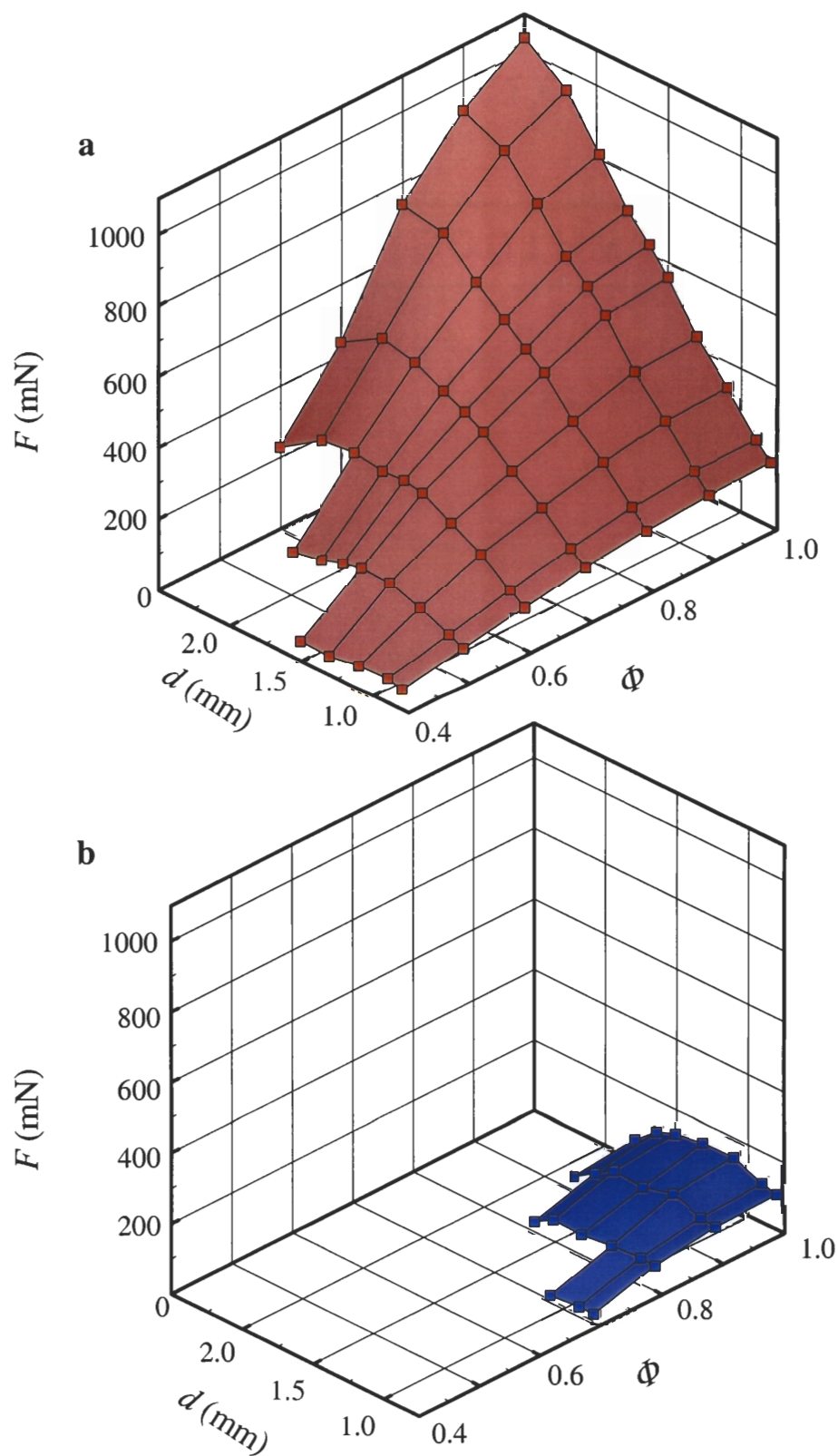


Figure 33. Surface plots of variation of the calculated peak thrust with  $\Phi$  and  $d$  for hydrogen (a) and propane (b).

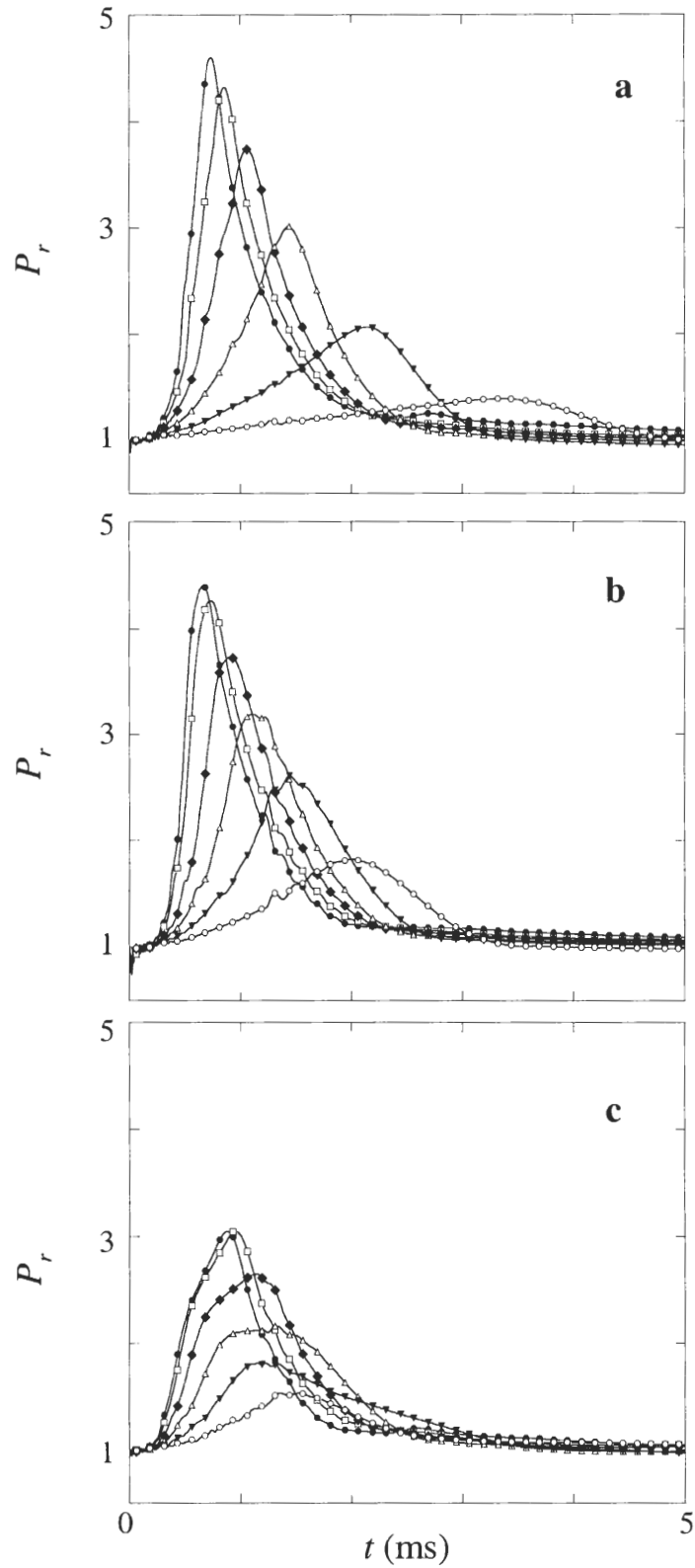


Figure 34. Phase averaged-combustor pressure for hydrogen with  $d = 1.30$  mm for  $H/D = 0.45$  (a),  $1.27$  (b), and  $3.59$  (c) for  $\Phi = 1.0$  ( $\bullet$ ),  $0.9$  ( $\square$ ),  $0.8$  ( $\blacklozenge$ ),  $0.7$  ( $\Delta$ ),  $0.6$  ( $\blacktriangledown$ ), and  $0.5$  ( $\circ$ ).

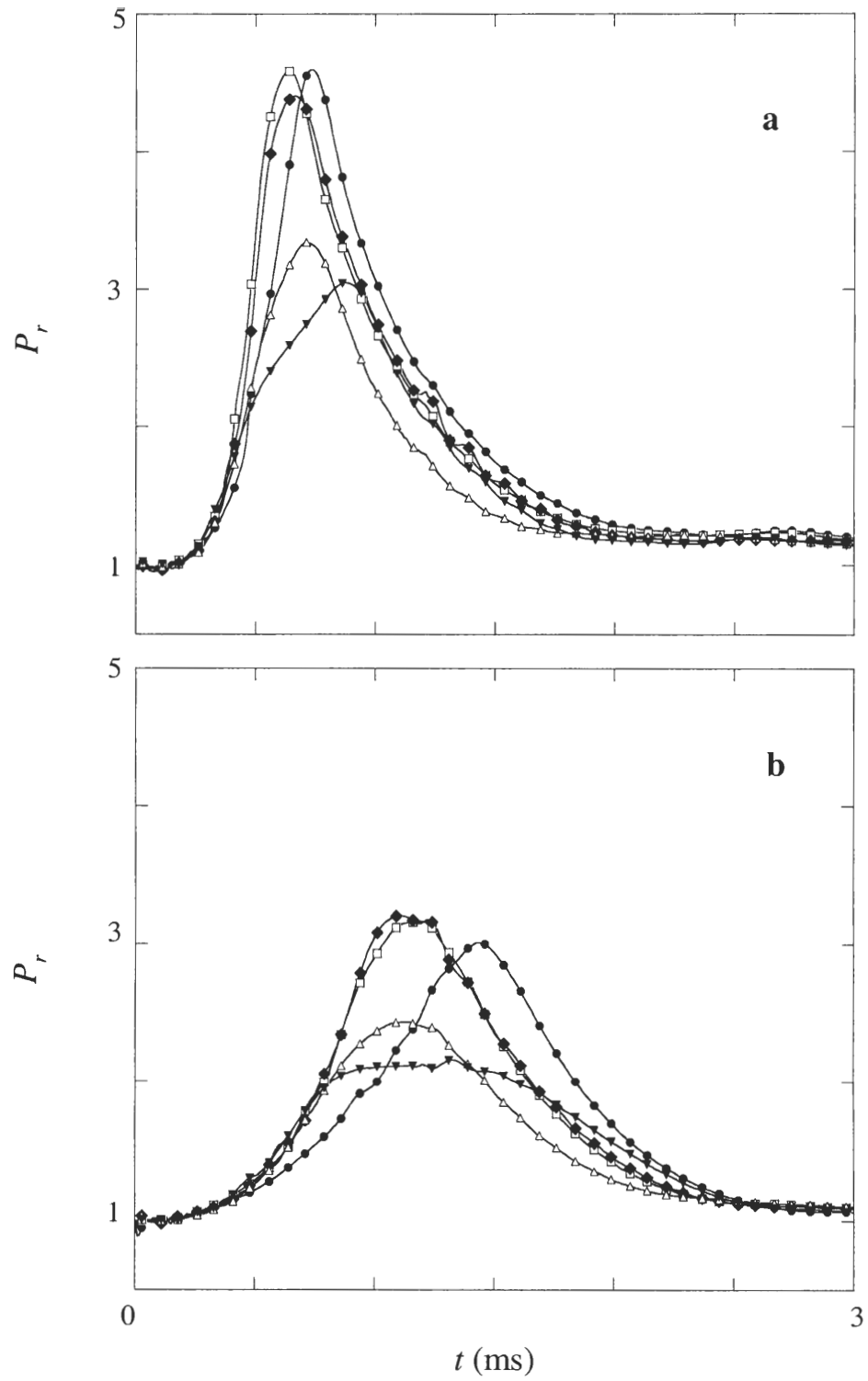


Figure 35. Phase-averaged combustor pressure for hydrogen with  $d=1.30$  mm and  $\Phi = 1.0$  (a) and  $0.7$  (b) for  $H/D = 0.45$  ( $\bullet$ ),  $0.82$  ( $\square$ ),  $1.27$  ( $\blacklozenge$ ),  $2.33$  ( $\triangle$ ), and  $3.59$  ( $\blacktriangledown$ ).

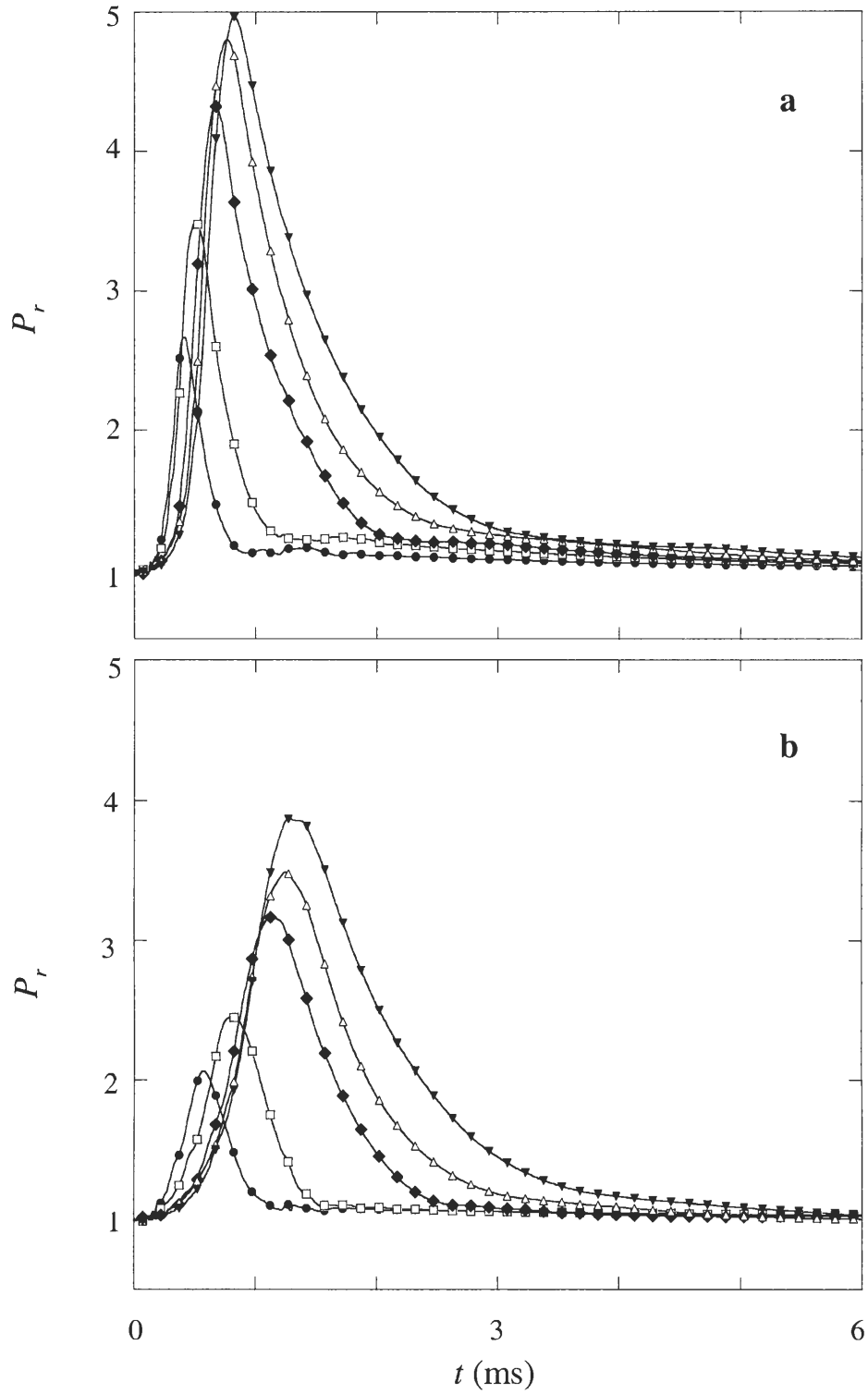


Figure 36. Phase-averaged combustor pressure for hydrogen with  $d = 1.30$  mm,  $f_{ideal} = 10$  Hz, and  $\Phi = 1.0$  (a) and  $0.7$  (b) for  $V = 0.25$  (●),  $0.50$  (□),  $1.00$  (◆),  $1.50$  (Δ), and  $2.00$  (▼) cc.



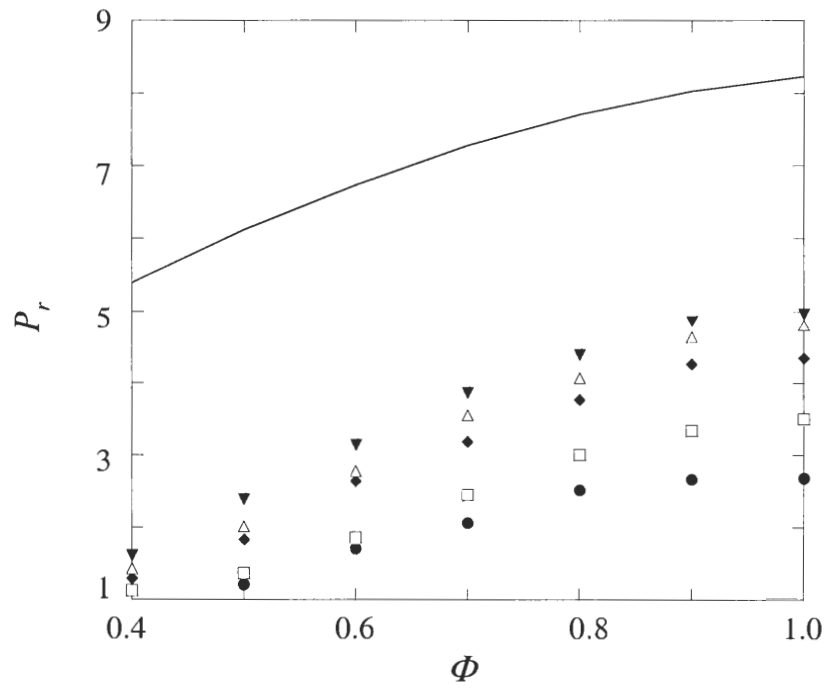


Figure 37. Variation of the phase-averaged peak pressures with  $\Phi$  for hydrogen with  $d = 1.30$  mm for  $V = 0.25$  ( $\bullet$ ),  $0.50$  ( $\square$ ),  $1.00$  ( $\blacklozenge$ ),  $1.50$  ( $\triangle$ ), and  $2.00$  ( $\blacktriangledown$ ) cc. The solid line is the idealized constant volume pressure.

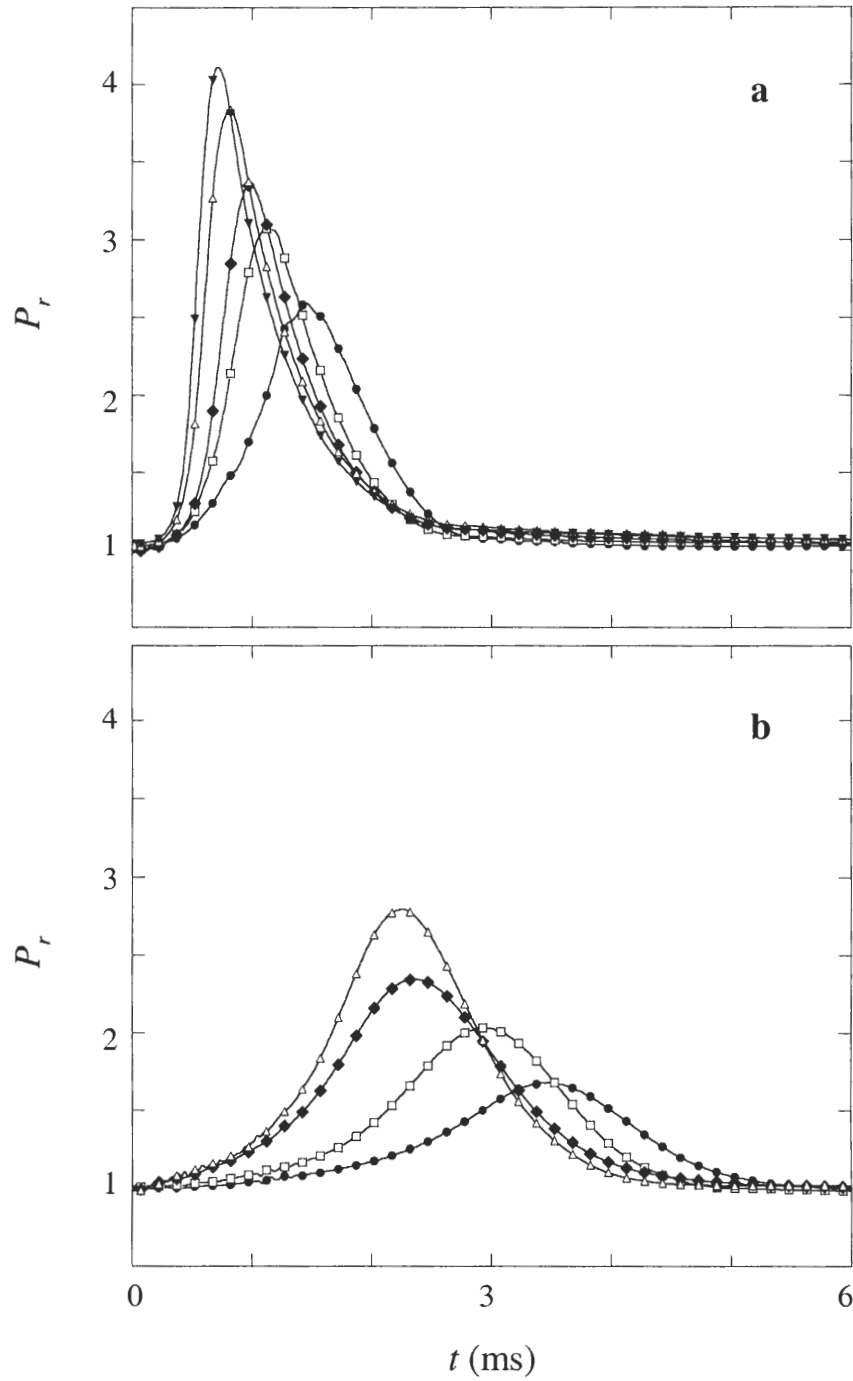


Figure 38. Phase-averaged combustor pressure for  $d = 1.30$  mm for hydrogen with  $\Phi = 0.6$  (a) and propane with  $\Phi = 1.0$  (b) for  $Q = 10$  (●), 30 (□), 50 (◆), 75 (Δ), and 100 (▼) cc/s.

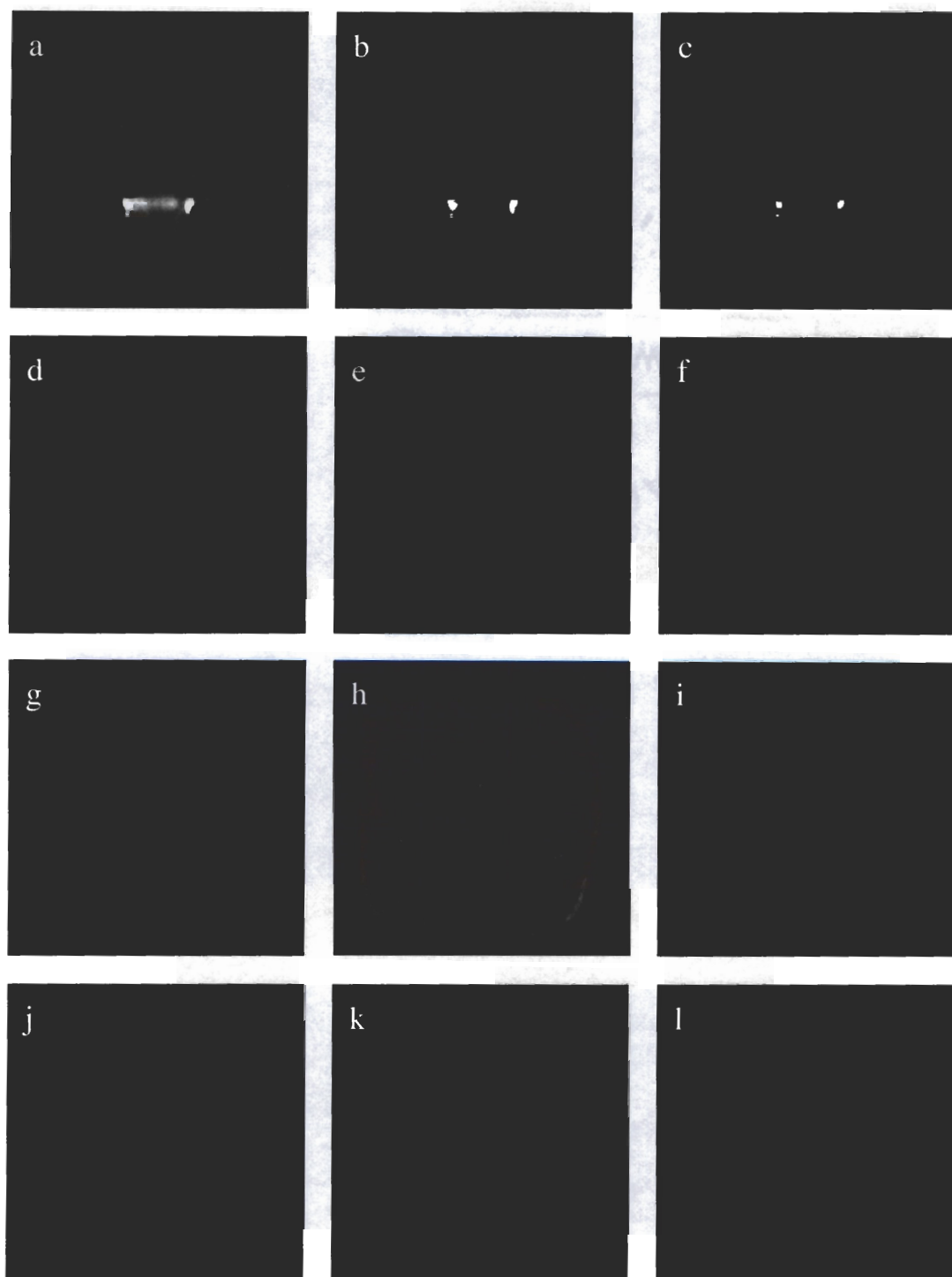


Figure 39. Sample flame photography images for stoichiometric propane-air mixture with  $d = 1.30$  mm and  $Q = 10$  cc/s for 0.5 (a), 1.0 (b), 1.5 (c), 2.0 (d), 2.5 (e), 3.0 (f), 3.5 (g), 4.0 (h), 4.5 (i), 5.0 (j), 5.5 (k), and 6.0 (l) ms after ignition.

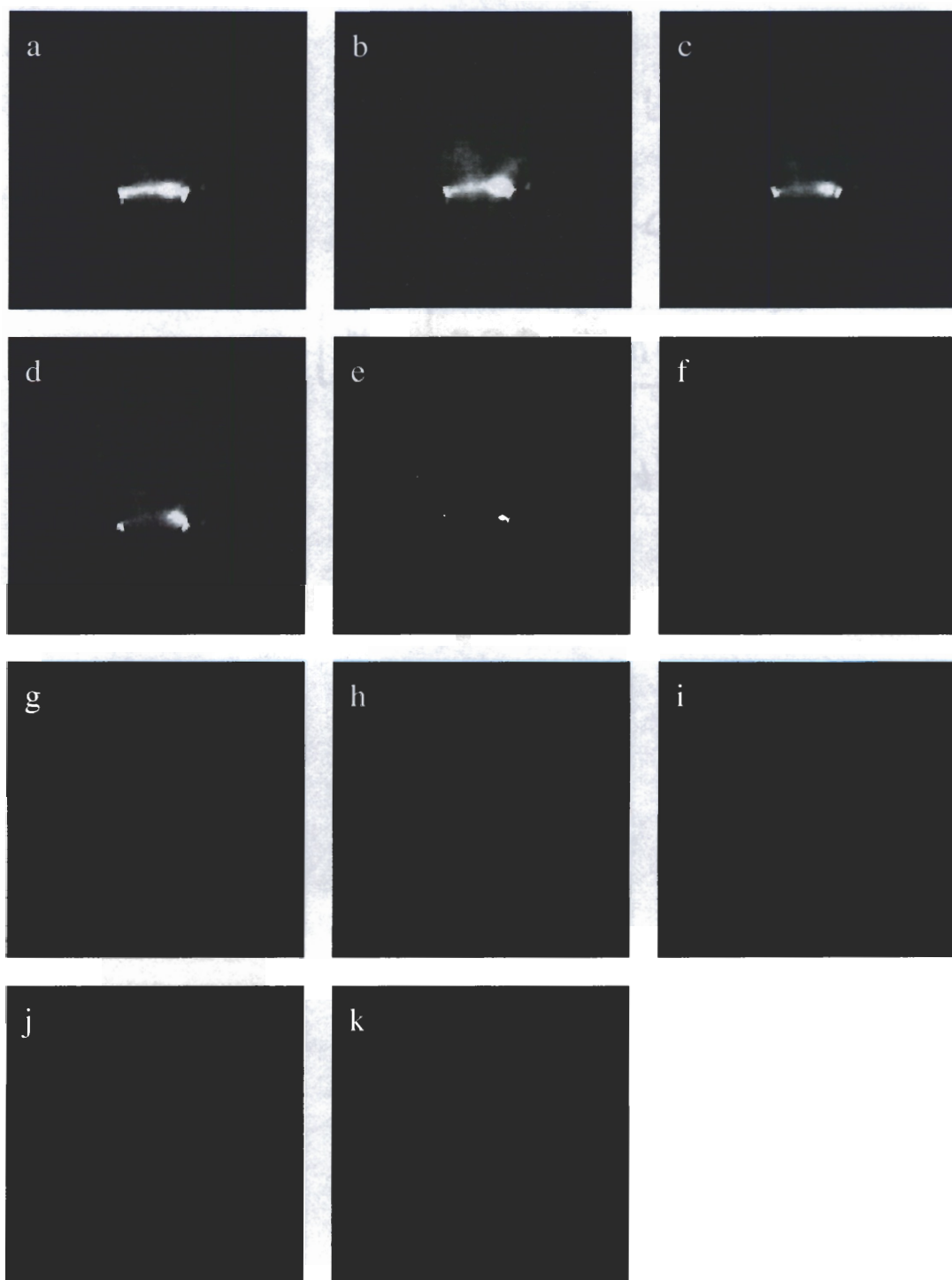


Figure 40. Sample flame photography images for stoichiometric propane-air mixture with  $d = 1.30$  mm and  $Q = 30$  cc/s for 0.25 (a), 0.5 (b), 0.75 (c), 1.0 (d), 1.5 (e), 2.0 (f), 2.5 (g), 3.0 (h), 3.5 (i), 4.0 (j), and 4.5 (k) ms after ignition.

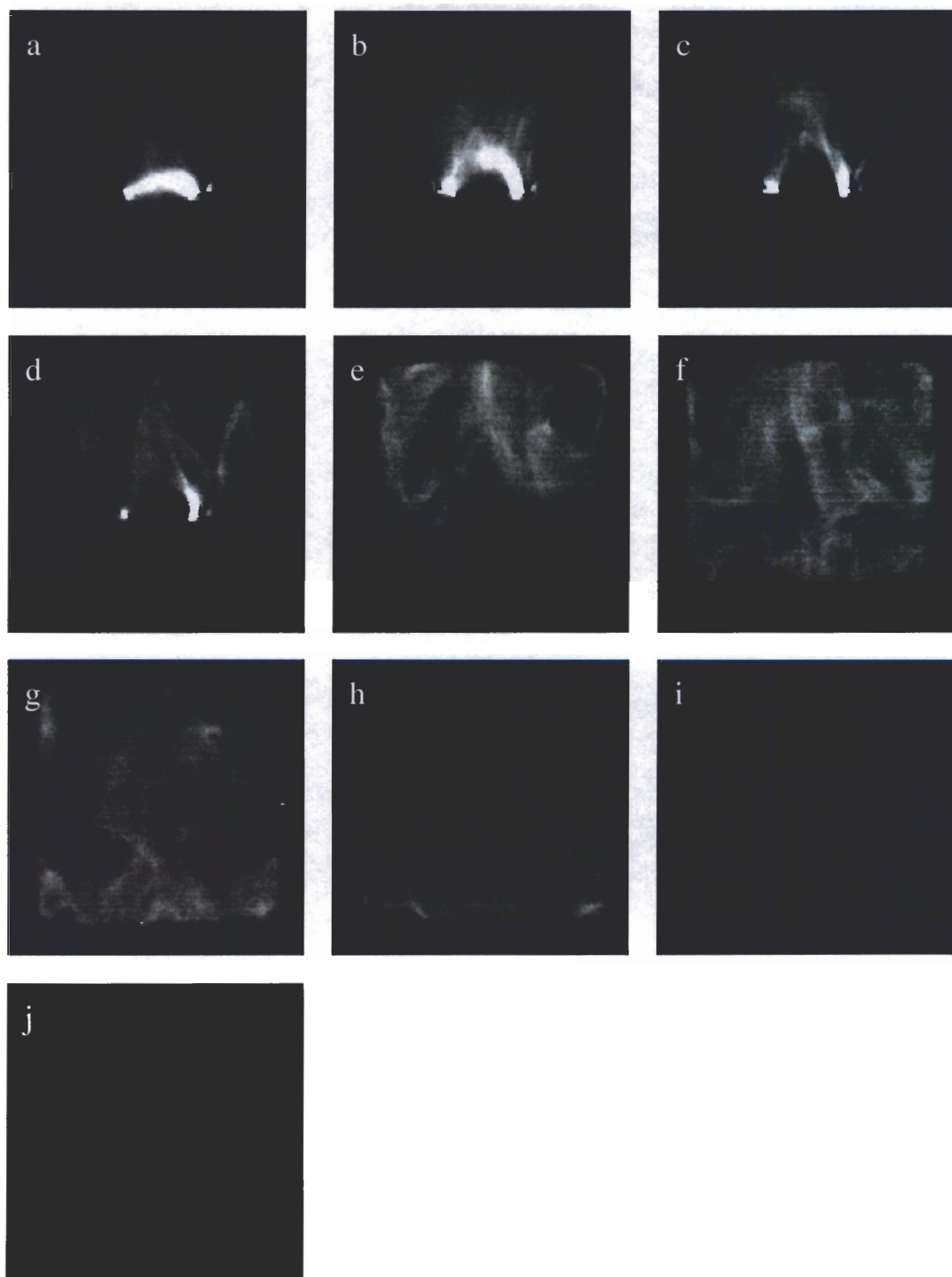


Figure 41. Sample flame photography images for stoichiometric propane-air mixture with  $d = 1.30$  mm and  $Q = 50$  cc/s for 0.25 (a), 0.5 (b), 0.75 (c), 1.0 (d), 1.5 (e), 2.0 (f), 2.5 (g), 3.0 (h), 3.5 (i), and 4.0 (j) ms after ignition.

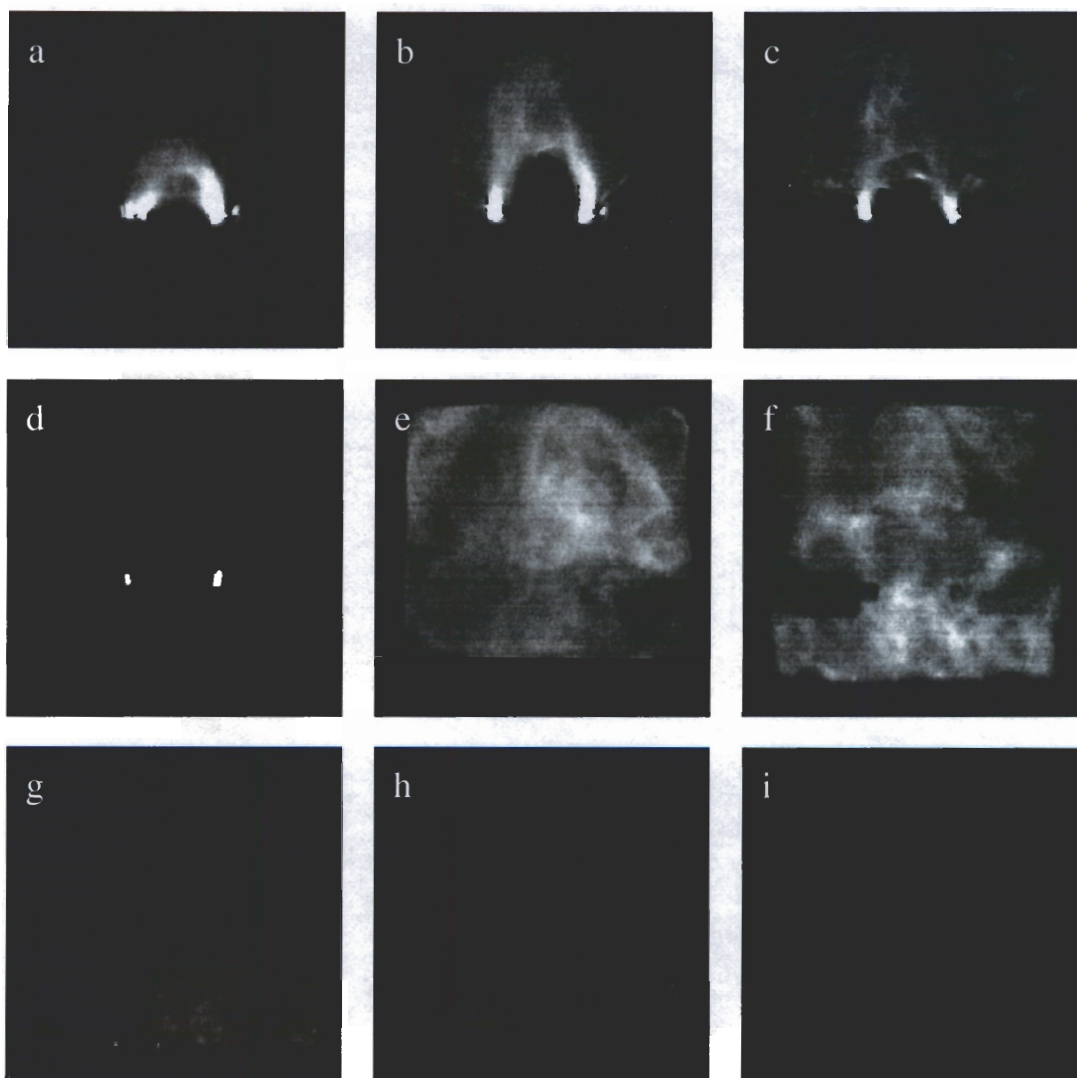


Figure 42. Sample flame photography images for stoichiometric propane-air mixture with  $d = 1.30\text{mm}$  and  $Q = 75\text{ cc/s}$  for 0.25 (a), 0.5 (b), 0.75 (c), 1.0 (d), 1.5 (e), 2.0 (f), 2.5 (g), 3.0 (h), 3.5 (i) ms after ignition.

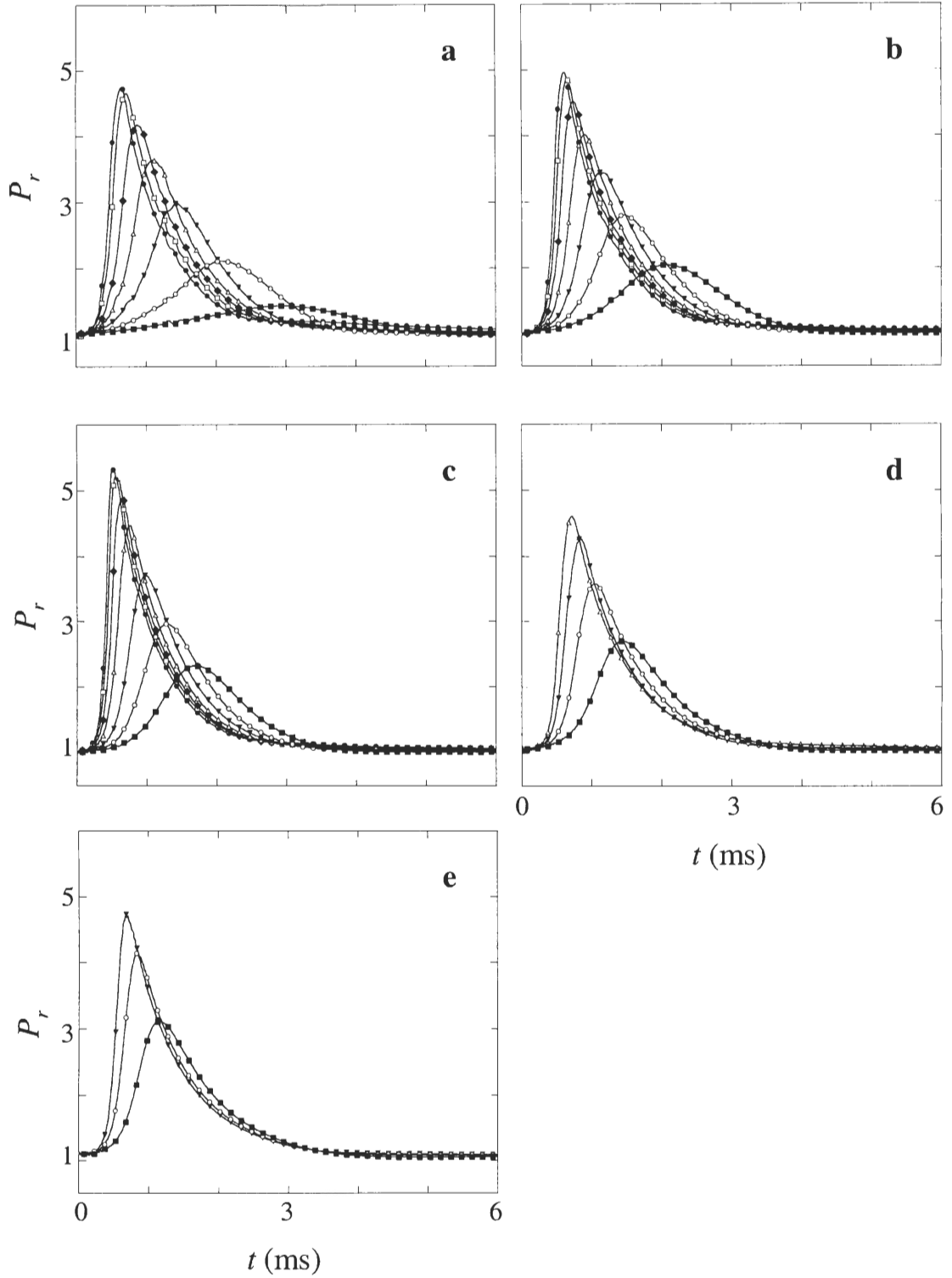


Figure 43. Phase-averaged combustor pressure for  $d = 1.09$  mm for hydrogen with  $\Phi = 1.0$  ( $\bullet$ ),  $0.9$  ( $\square$ ),  $0.8$  ( $\blacklozenge$ ),  $0.7$  ( $\triangle$ ),  $0.6$  ( $\blacktriangledown$ ),  $0.5$  ( $\circ$ ), and  $0.4$  ( $\blacksquare$ ) for  $Q = 10$  (a),  $30$  (b),  $50$  (c),  $75$  (d), and  $100$  (e) cc/s.

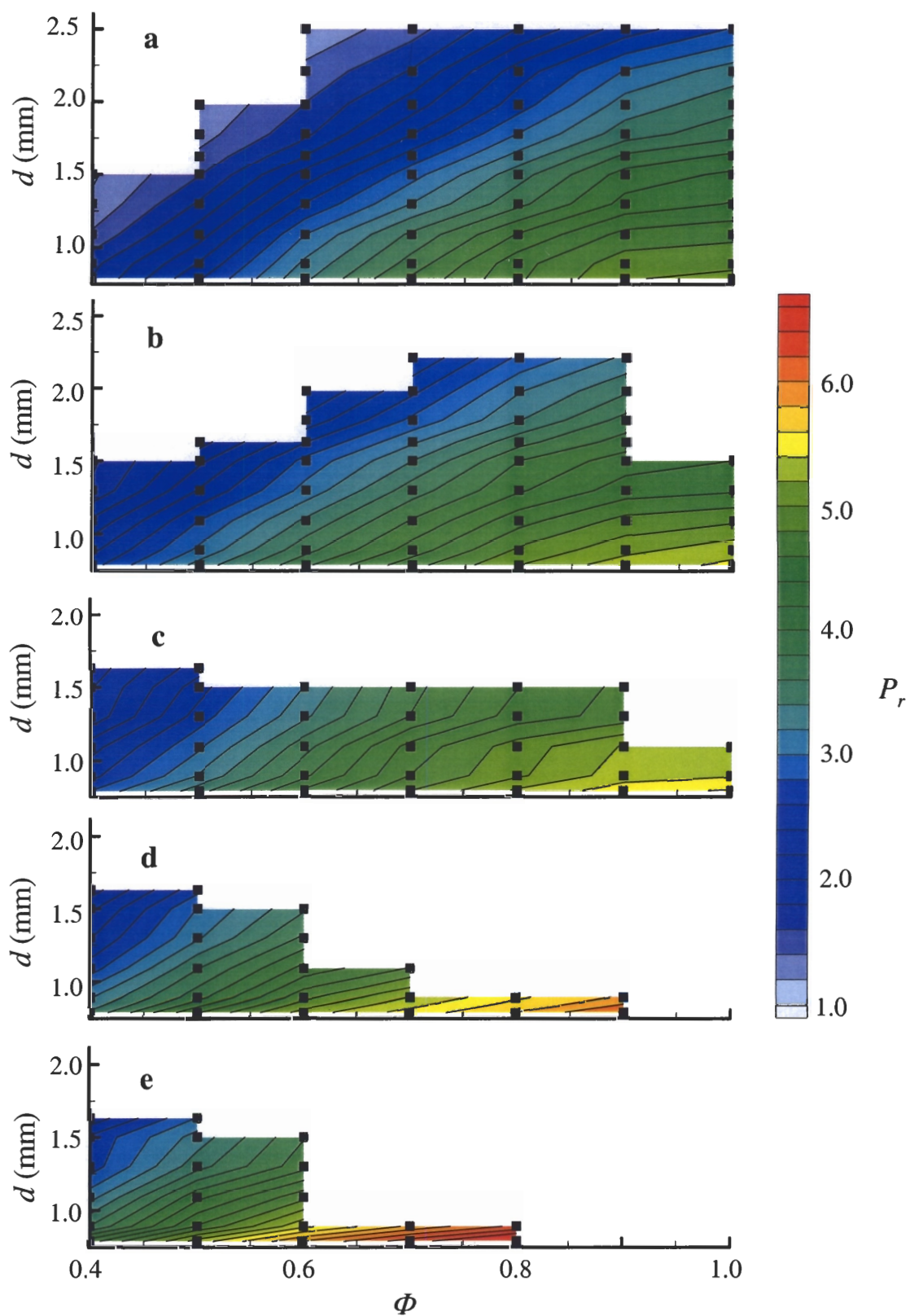


Figure 44. Contour plots of peak combustor pressure varying  $\Phi$  and  $d$  for hydrogen with  $Q = 10$  (a), 30 (b), 50 (c), 75 (d), and 100 (e) cc/s (data points represented by ■).



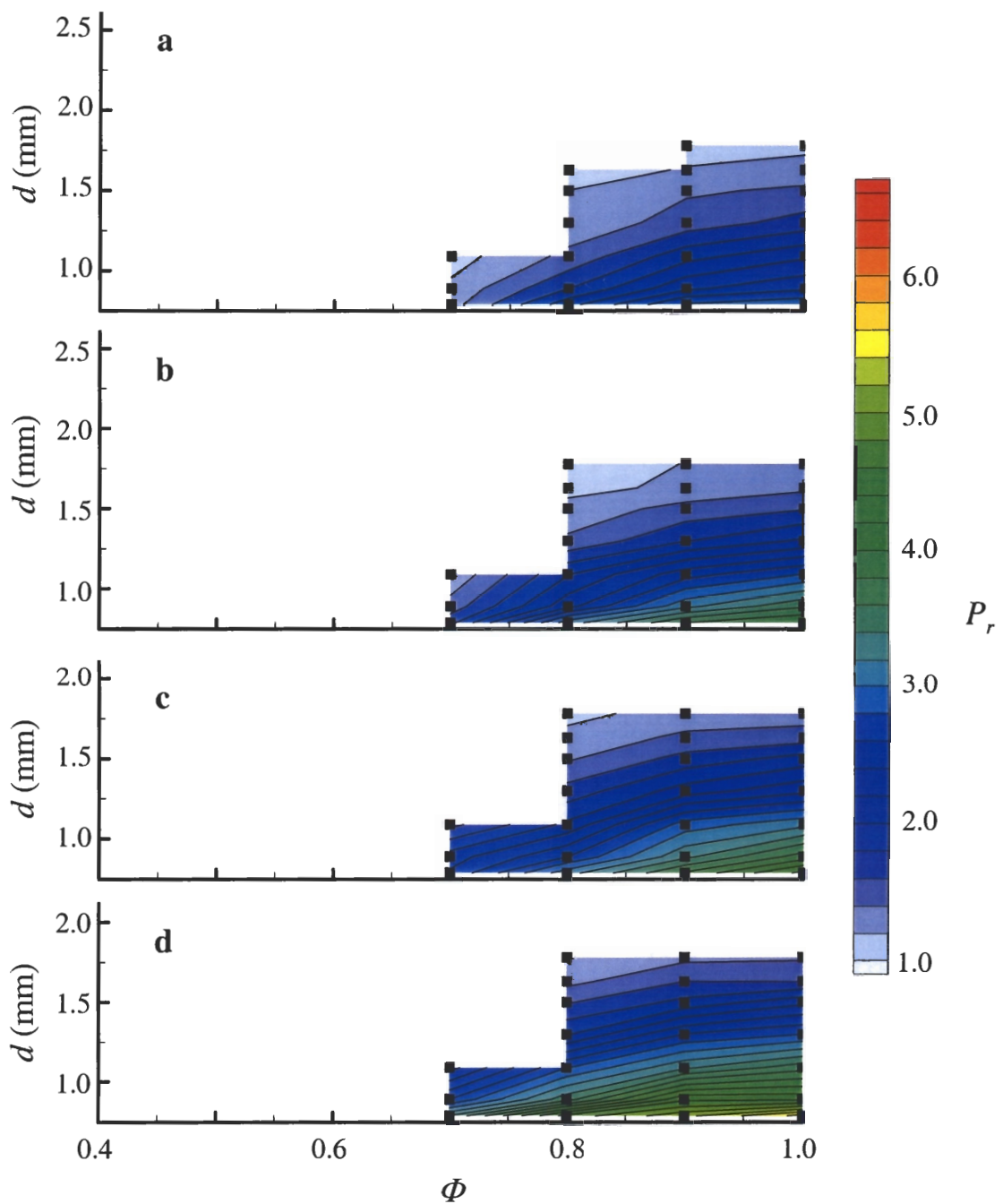


Figure 45. Contour plots of peak combustor pressure varying  $\Phi$  and  $d$  for propane with  $Q = 10$  (a), 30 (b), 50 (c), and 75 (d) cc/s (data points represented by ■).

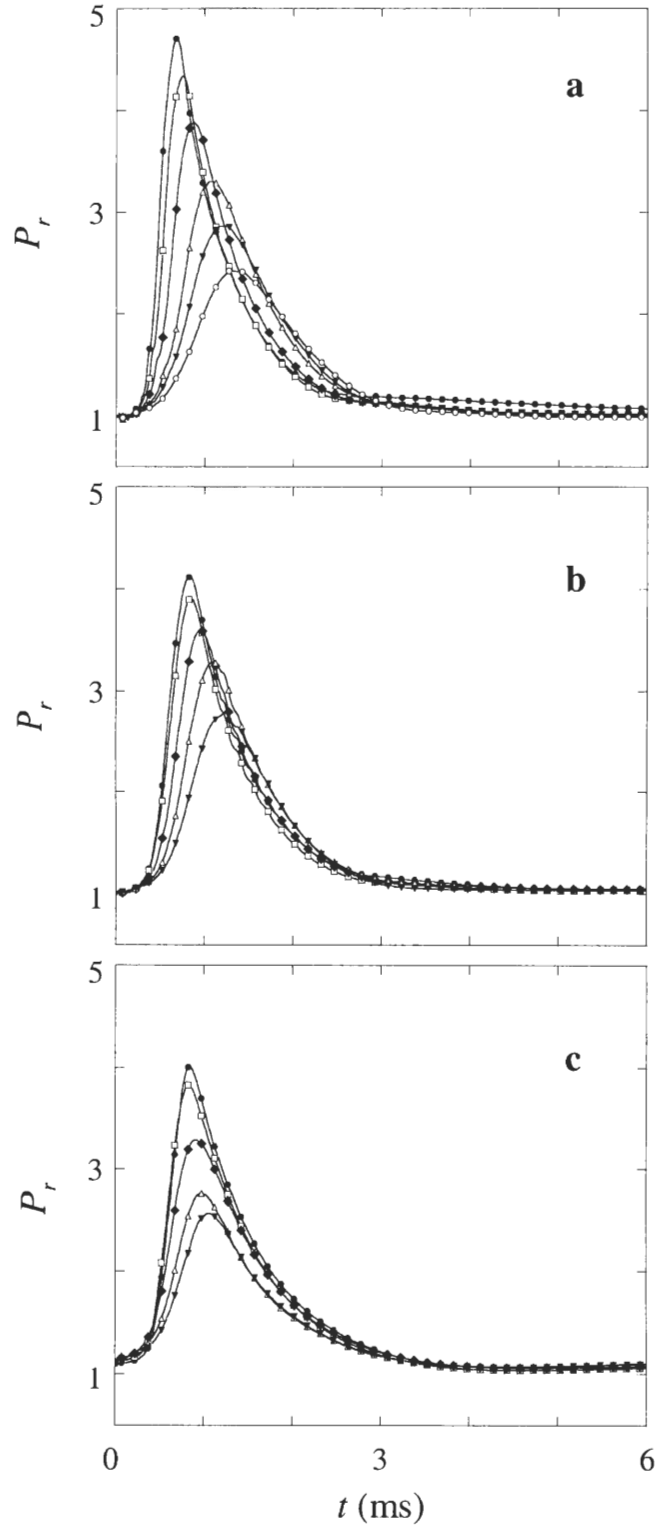


Figure 46. Phase averaged-combustor pressure for hydrogen with  $d = 1.30$  mm for  $\Phi = 1.0$  and  $Q = 10$  cc/s (a),  $\Phi = 0.8$  and  $Q = 30$  cc/s (b), and  $\Phi = 0.5$  and  $Q = 100$  cc/s (c) for  $f/f_{ideal} = 0.1$  ( $\bullet$ ),  $0.4$  ( $\square$ ),  $0.7$  ( $\blacklozenge$ ),  $1.0$  ( $\Delta$ ),  $1.2$  ( $\blacktriangledown$ ), and  $1.5$  ( $\circ$ ).

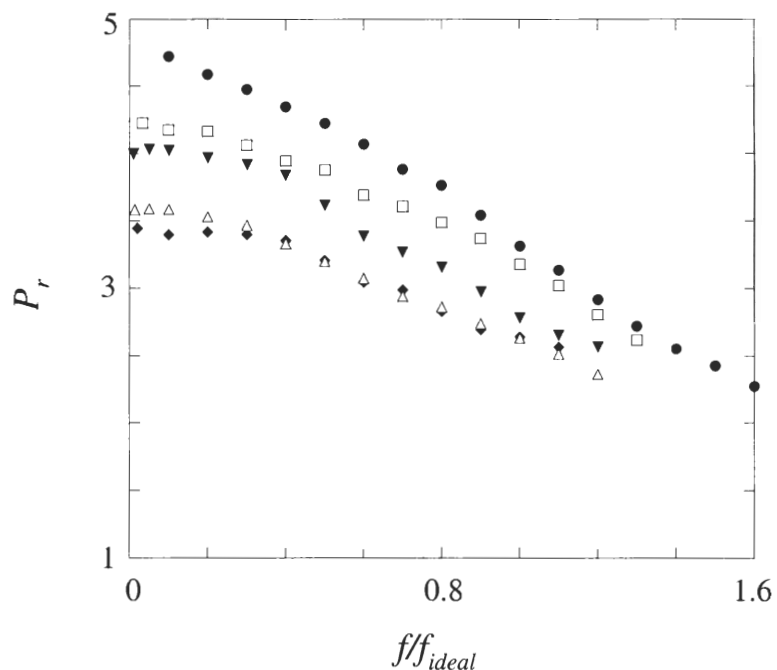


Figure 47. Peak combustor pressures for hydrogen with  $d = 1.09$  mm varying  $f/f_{ideal}$  for  $Q = 10$  cc/s and  $\Phi = 1.0$  ( $\bullet$ ),  $Q = 30$  cc/s and  $\Phi = 0.8$  ( $\square$ ),  $Q = 50$  cc/s and  $\Phi = 0.6$  ( $\blacklozenge$ ),  $Q = 75$  cc/s and  $\Phi = 0.5$  ( $\triangle$ ), and  $Q = 100$  cc/s and  $\Phi = 0.5$  ( $\blacktriangledown$ )

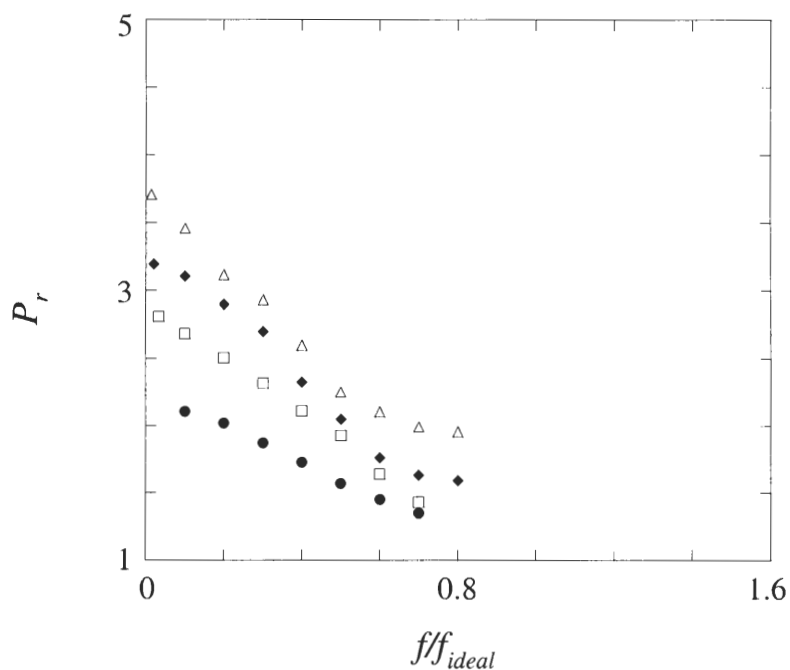


Figure 48. Peak combustor pressures for propane with  $\Phi = 1.0$  and  $d = 1.09$  mm varying  $f/f_{ideal}$  for  $Q = 10$  cc/s ( $\bullet$ ),  $30$  cc/s ( $\square$ ),  $50$  cc/s ( $\blacklozenge$ ), and  $75$  cc/s ( $\triangle$ ).

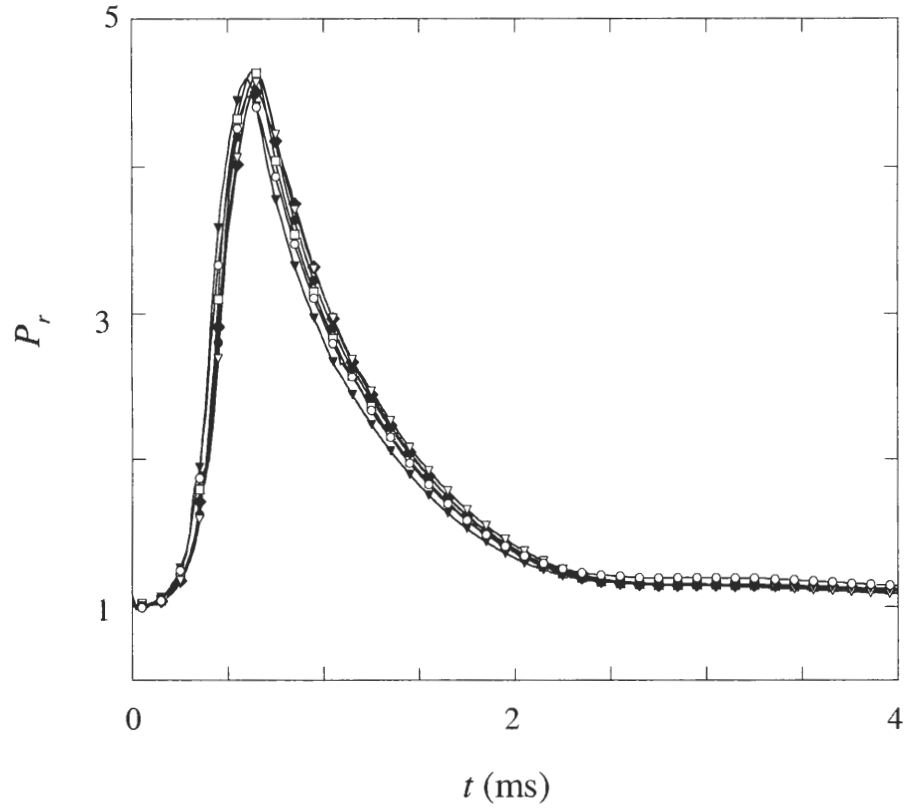


Figure 49. Phase-averaged combustor pressure for hydrogen ( $d = 1.09$  mm,  $\Phi = 1.0$ ) for  $E = 2$  ( $\bullet$ ), 5 ( $\square$ ), 10 ( $\blacklozenge$ ), 20 ( $\triangle$ ), 40 ( $\blacktriangledown$ ) mJ from CDI system and automotive system ( $\circ$ ,  $50 < E < 100$  mJ) .

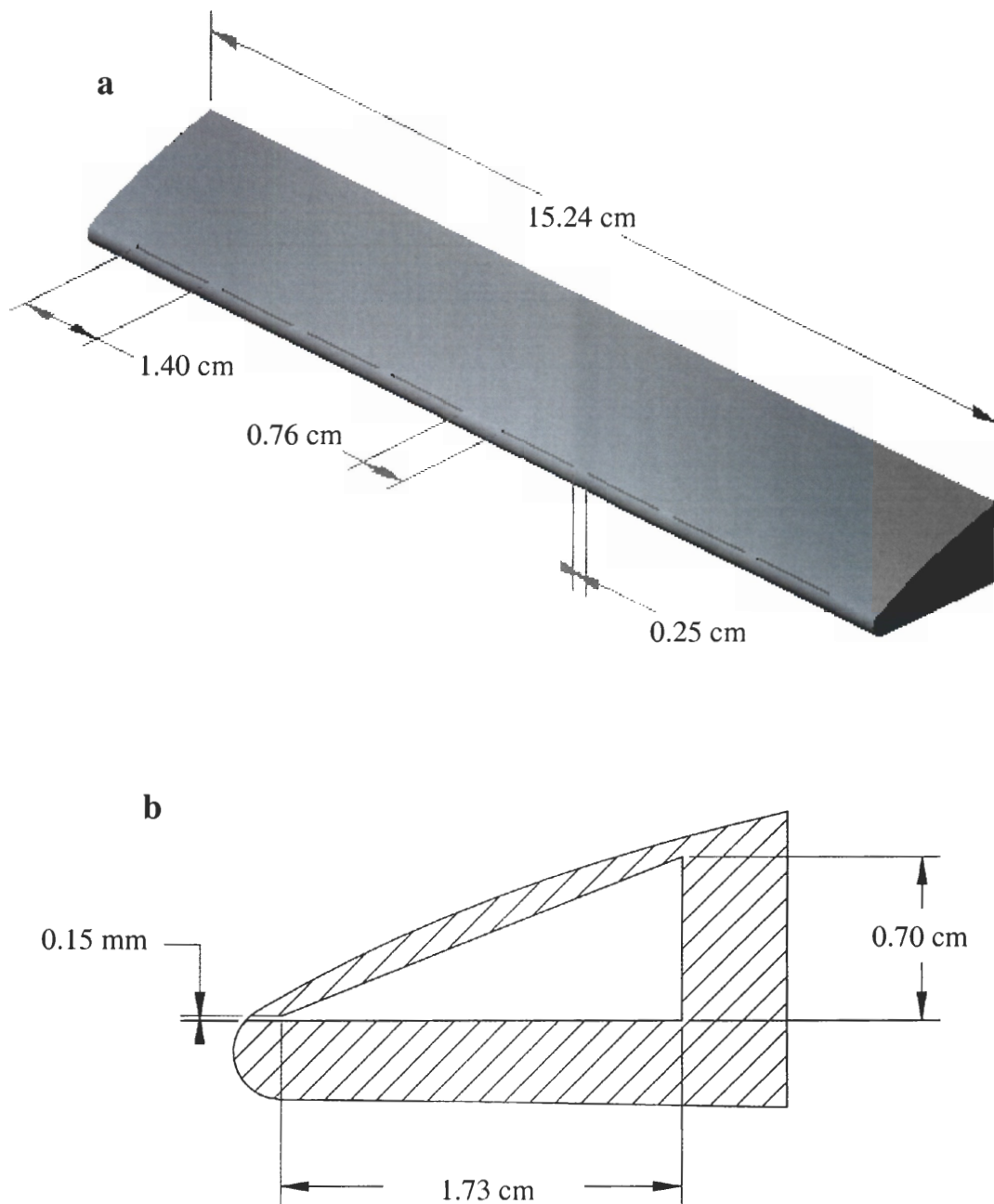


Figure 50. Isometric view of leading edge of airfoil with integrated bank of 8 combustion-driven jet actuators (a) with cross-sectional view along midline of combustor (b).

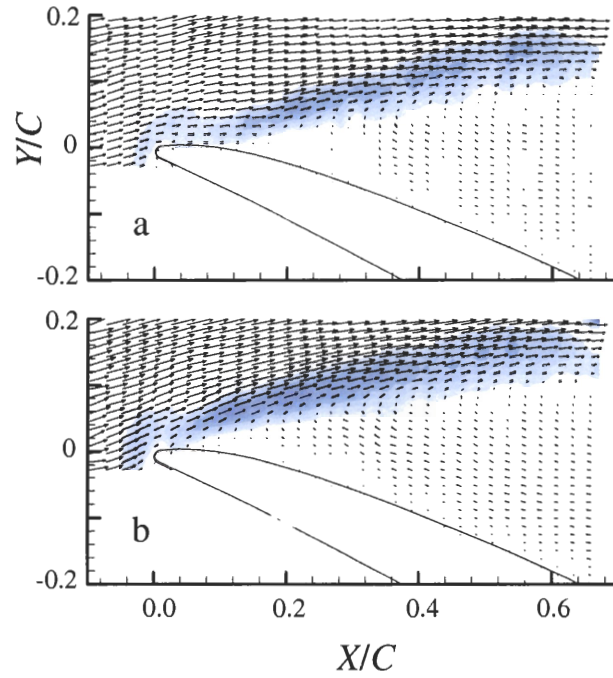


Figure 51. PIV vector fields and vorticity contours for baseline case ( $\alpha = 24.1^\circ$ ,  $U_\infty = 12.5$  m/s,  $Re_c = 1.80 \times 10^5$ ) with actuator fully off (a) and steady flow with no ignition (b).

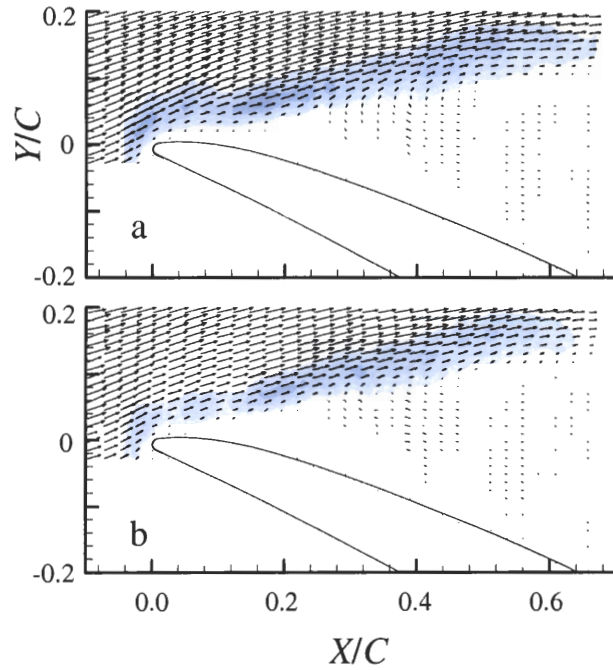


Figure 52. PIV vector fields and vorticity contours for baseline case ( $\alpha = 24.1^\circ$ ,  $U_\infty = 25.0$  m/s,  $Re_c = 3.60 \times 10^5$ ) with actuator fully off (a) and steady flow with no ignition (b).

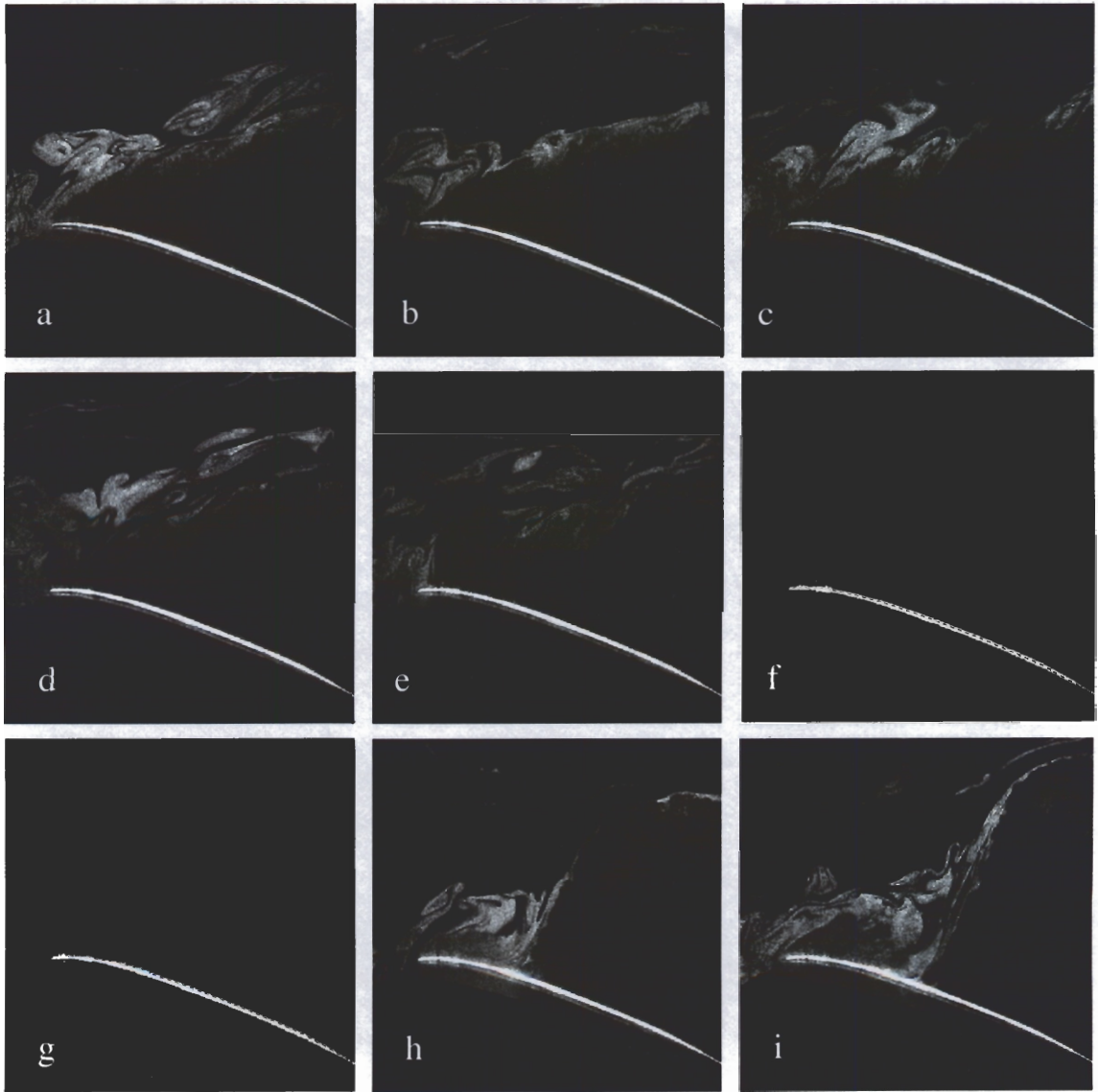


Figure 53. Smoke flow visualization images for transient case ( $f = 3$  Hz) with  $\alpha = 24.1^\circ$  and  $U_\infty = 12.5$  m/s for  $t = 0$  (a), 1 (b), 2 (c), 3 (d), 5 (e), 8 (f), 12 (g), 15 (h), and 20 ms (i).

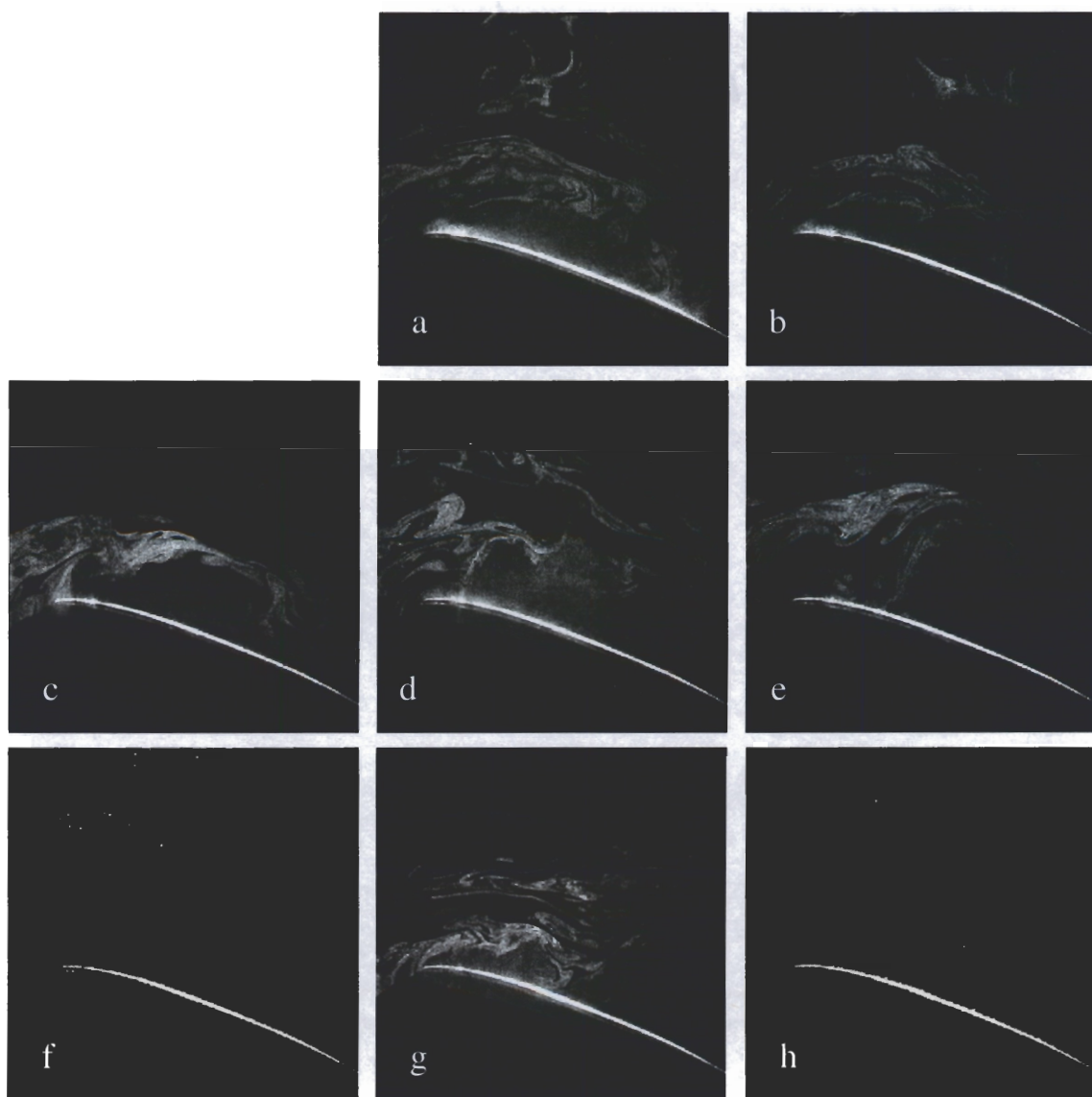


Figure 54. Smoke flow visualization images for dynamic case ( $f = 45$  Hz) with  $\alpha = 24.1^\circ$  and  $U_\infty = 12.5$  m/s for  $t = 1$  (a), 2 (b), 3 (c), 6 (d), 9 (e), 12 (f), 15 (g), and 20 ms (h).



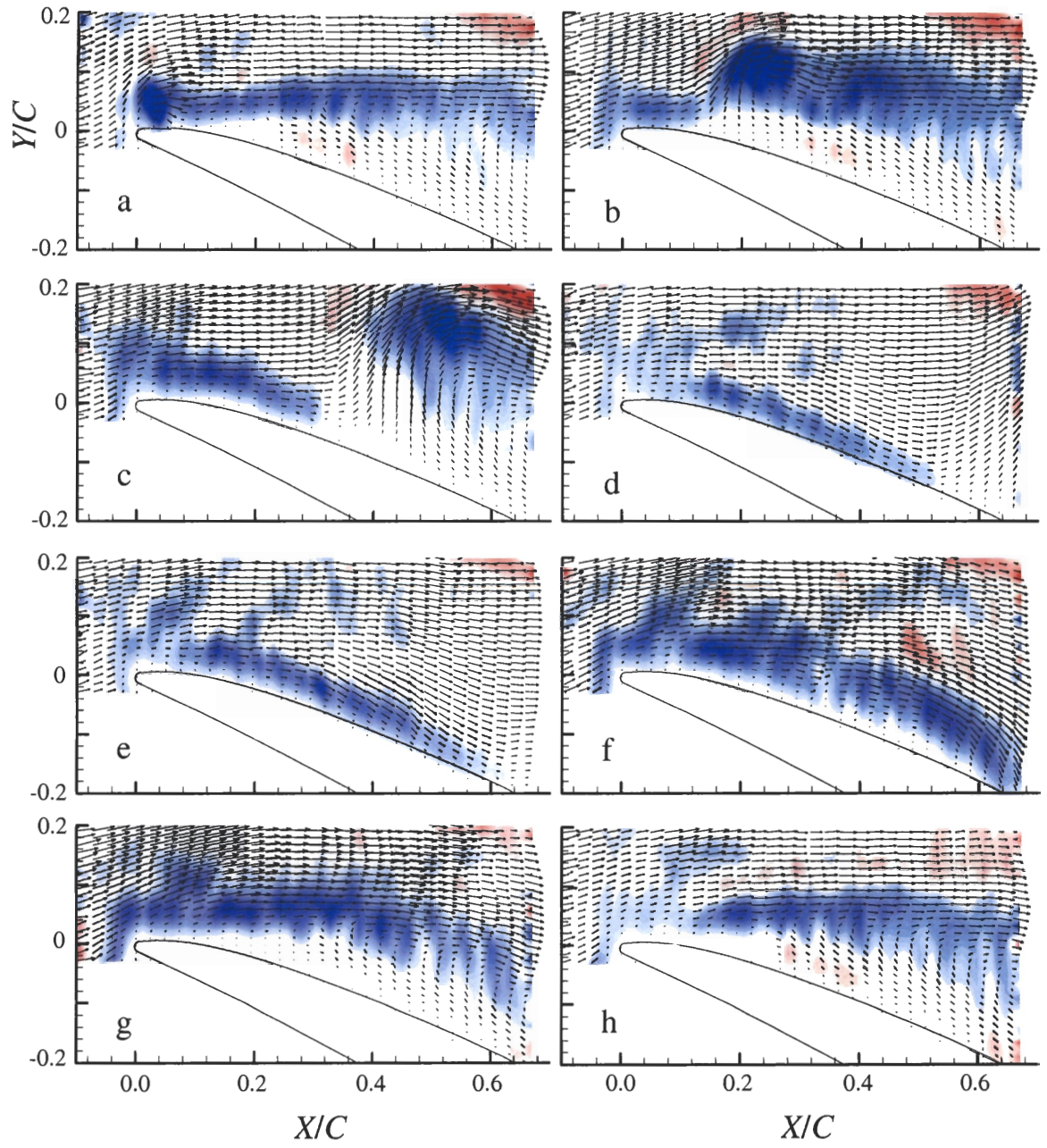


Figure 55. PIV velocity vector fields and vorticity contours for  $\alpha = 24.1^\circ$  and  $U_\infty = 25.0$  m/s with  $f = 15$  Hz ( $St = 0.137$ ) for  $t/\tau = 0.045$  (a), 0.090 (b), 0.135 (c), 0.180 (d), 0.225 (e), 0.300 (f), 0.450 (g), and 0.600 (h).

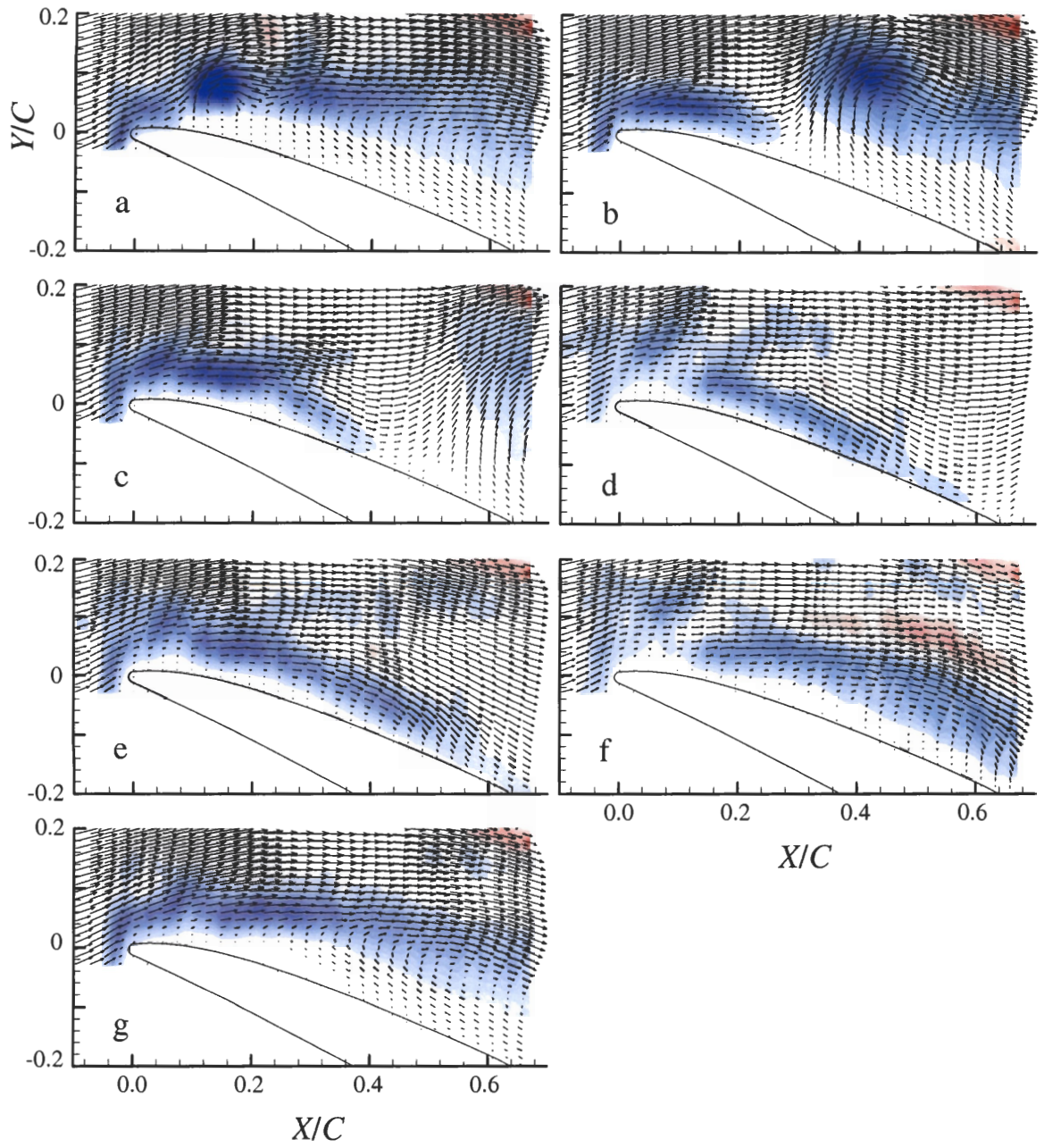


Figure 56. PIV velocity vector fields and vorticity contours for  $\alpha = 24.1^\circ$  and  $U_\infty = 25.0$  m/s with  $f = 30$  Hz ( $St = 0.274$ ) for  $t/\tau = 0.090$  (a),  $0.180$  (b),  $0.270$  (c),  $0.360$  (d),  $0.450$  (e),  $0.600$  (f), and  $0.900$  (g).



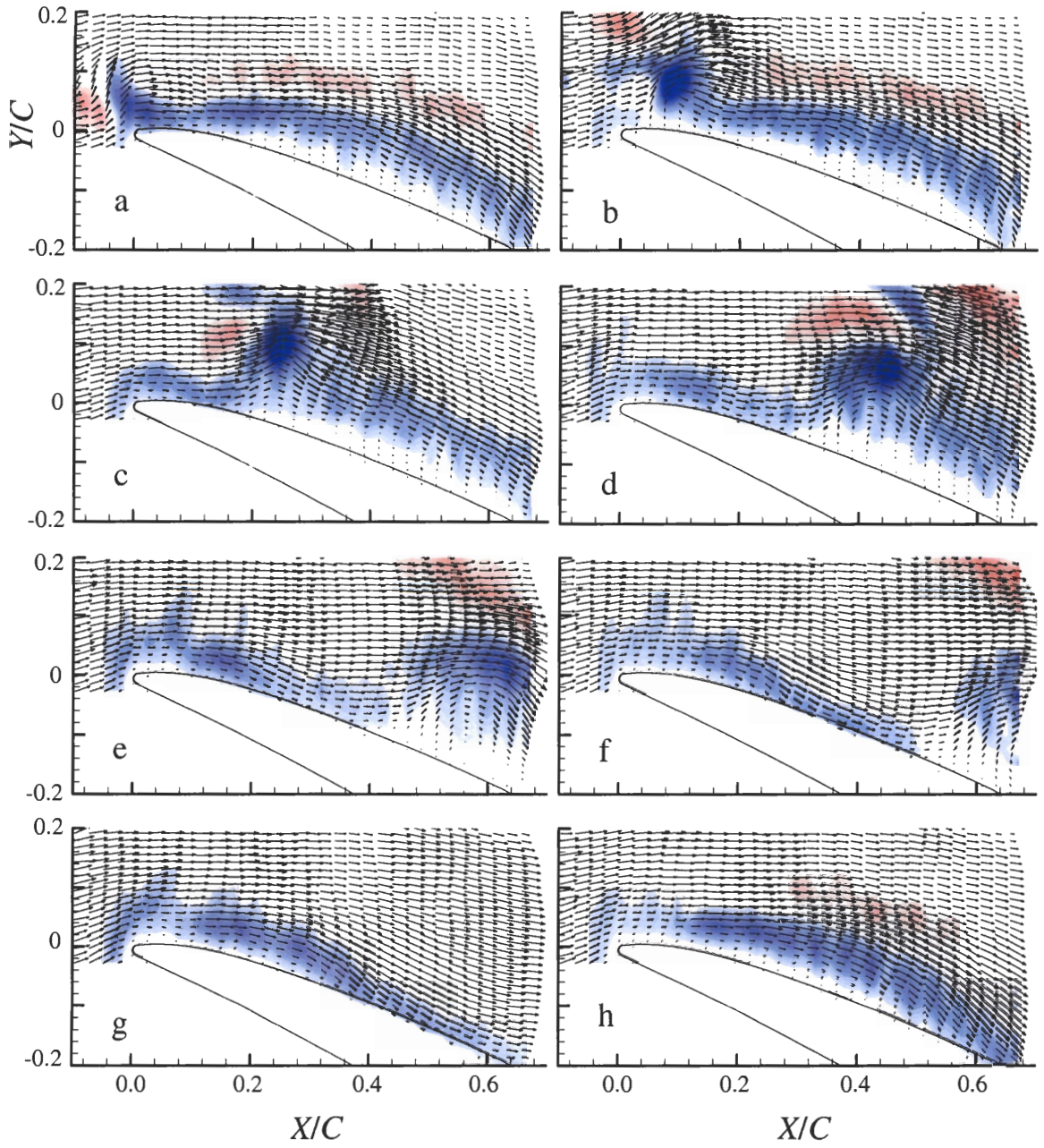


Figure 57. PIV velocity vector fields and vorticity contours for  $\alpha = 24.1^\circ$  and  $U_\infty = 12.5$  m/s with  $f = 30$  Hz ( $St = 0.549$ ) for  $t/\tau = 0.030$  (a), 0.090 (b), 0.180 (c), 0.270 (d), 0.360 (e), 0.450 (f), 0.600 (g), and 0.900 (h).

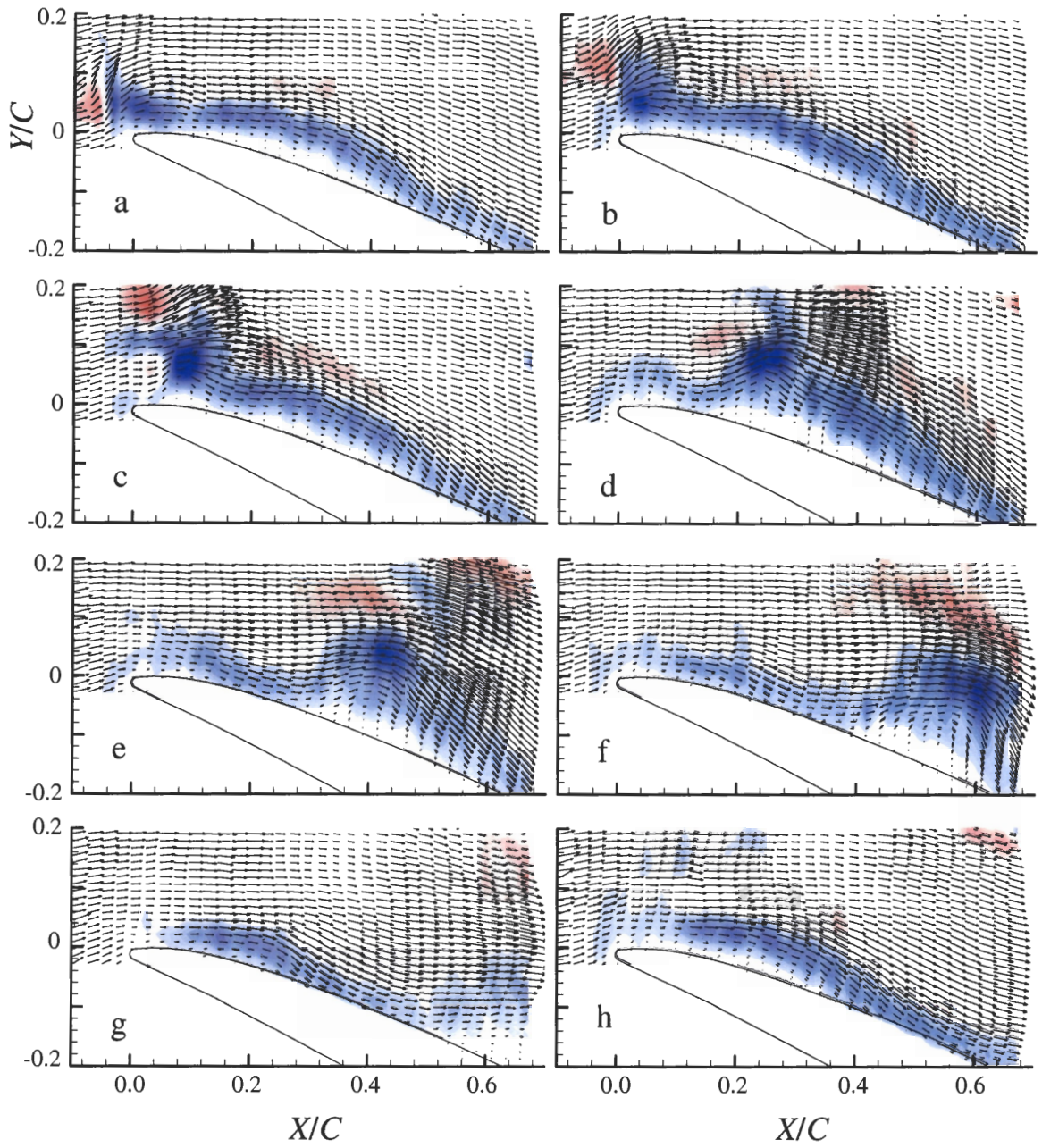


Figure 58. PIV velocity vector fields and vorticity contours for  $\alpha = 24.1^\circ$  and  $U_\infty = 12.5$  m/s with  $f = 45$  Hz ( $St = 0.823$ ) for  $t/\tau = 0.045$  (a), 0.090 (b), 0.135 (c), 0.270 (d), 0.405 (e), 0.540 (f), 0.675 (g), and 0.900 (h).

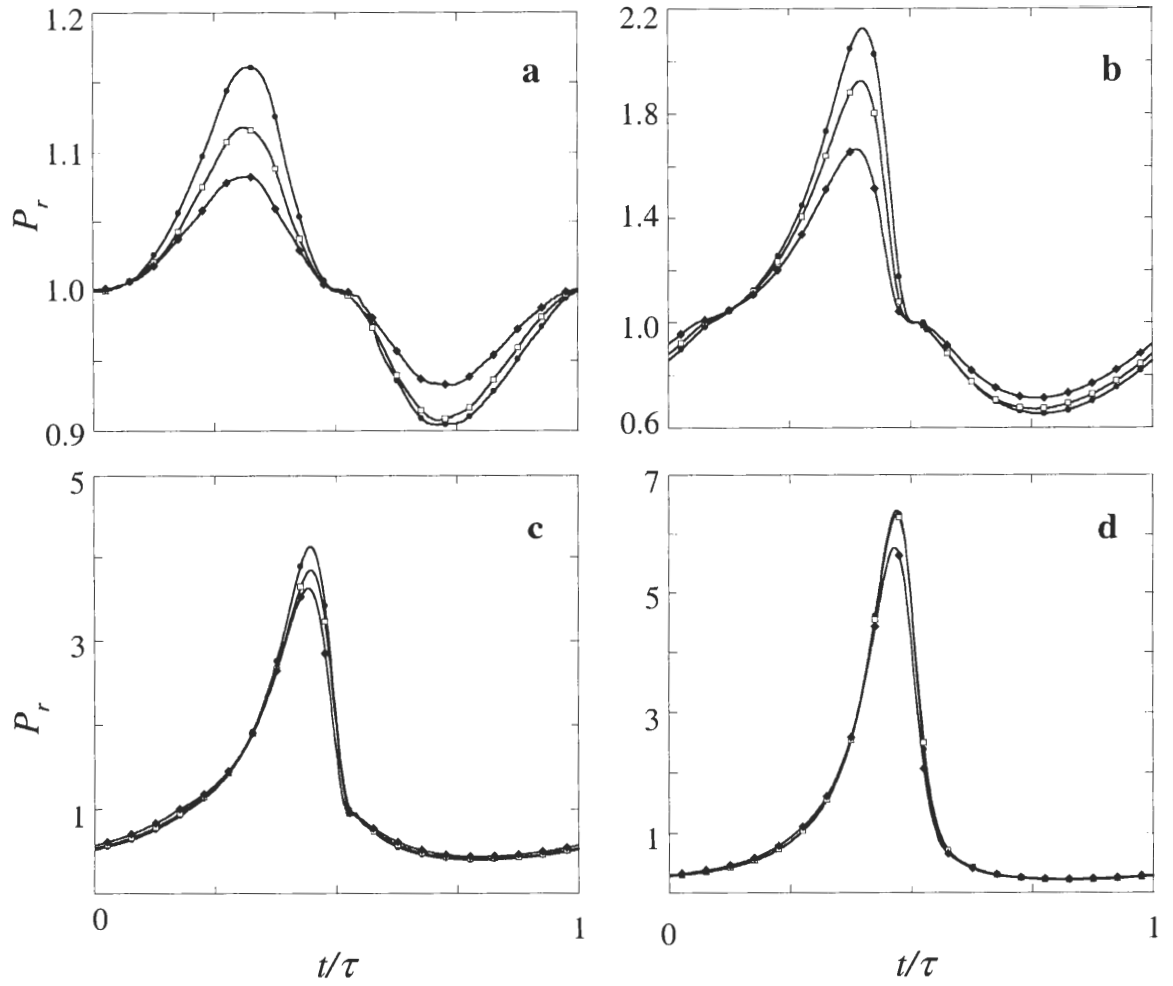


Figure 59. Phase-averaged cylinder pressures over cycle for compressible synthetic jet with  $L_o/d = 2065$  and  $r = 27.1$  varying orifice geometry for  $l/d = 0.5$  ( $\bullet$ ),  $2.0$  ( $\square$ ), and  $2.0$  with  $45^\circ$  chamfer on both sides of orifice ( $\blacklozenge$ ) with  $f = 10$  (a),  $25$  (b),  $50$  (c), and  $100$  (d) Hz.

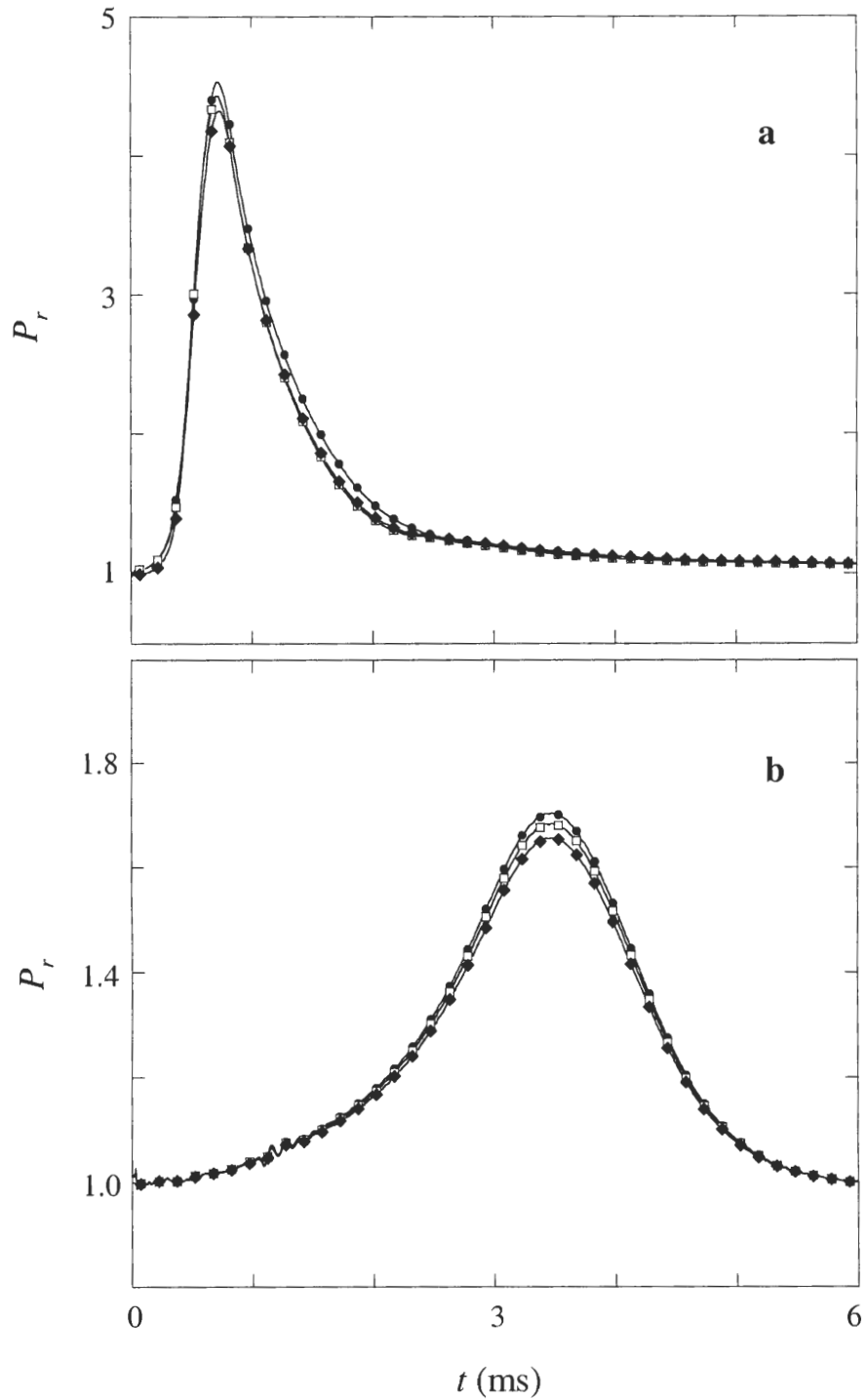


Figure 60. Phase-averaged combustor pressures for combustion driven jet actuator for stoichiometric hydrogen (a) and propane (b) mixtures with  $Q = 10$  cc/s and  $d = 1.30$  mm varying orifice geometry for  $l/d = 0.75$  ( $\bullet$ ),  $2.0$  ( $\square$ ), and  $2.0$  with  $45^\circ$  chamfer on orifice ( $\blacklozenge$ ). Note that pressure scales are different for (a) and (b).

## REFERENCES

- Adler, U., editor, *Automotive Electric/Electronic Systems*, Society of Automotive Engineers: Warrendale, PA, 1995.
- Amitay, M., Smith, B.L., and Glezer, A., "Aerodynamic flow control using synthetic jet technology," AIAA Paper 98-0208, 1998.
- Amitay, M., Kibens, V., Parekh, D.E., and Glezer, A., "Flow reattachment dynamics over a thick airfoil controlled by synthetic jet actuators," AIAA Paper 99-1001, 1999.
- Belles, F.E., and Simon, D.M., "Variation of the pressure limits of flame propagation with tube diameter for propane-air mixtures," National Advisory Committee for Aeronautics (NACA) Research Memorandum E51J09, 1951.
- Coe, D.J., Allen M.G., Trautman, M., and Glezer, A., "Micromachined jets for manipulation of macro flows," *Technical Digest: Solid State Sensor and Actuator Workshop*, pp.243-247, 1994.
- Crook, A., and Wood, N.J., "Measurements and visualizations of synthetic jets," AIAA Paper 2001-0145, January 2001.
- Davis, S.A., and Glezer, A., "Mixing control of fuel jets using synthetic jet technology: velocity field measurements," AIAA Paper 99-0447, January 1999.
- Drell, I.L., and Belles, F.E., "Survey of hydrogen combustion properties," National Advisory Committee for Aeronautics (NACA) Report 1383, 1958.
- Epstein, A.H., et al, "Power MEMS and microengines," *1997 International Conference on Solid-State Sensors and Actuators*, Vol. 2, pp.753-756, 1997.
- Faulkner, J.C., Scarborough, D.E., and Jagoda, J.I., "A study of ignition and flame propagation in a small, high surface-to-volume ratio combustor," AIAA Paper 2000-0591, 2000.
- Frendi, A., and Sibulkin, M., "Dependence of minimum ignition energy on ignition parameters," *Combustion Science and Technology*, Vol. 73, pp. 395-413, 1990.
- Fu, K., et al, "Microscale combustion research for applications to MEMS rotary IC engine," *Proceedings of ASME 35<sup>th</sup> National Heat Transfer Conference*, pp.613-618, 2000.
- Gallas, Q., et al, "Lumped element modeling of piezoelectric-driven synthetic jet actuators," AIAA Paper 2002-0125, January 2002.



Gharib, M., Rambod, E., and Shariff, K., "A universal time scale for vortex ring formation," *Journal of Fluid Mechanics*, Vol. 360, pp.297-318, 1998.

Gillaranz, J.L., Traub, L.W., and Rediniotis, O.K., "Characterization of a compact, high-power synthetic jet actuator for flow separation control," AIAA Paper 2002-0127, January 2002.

Honohan, A.M., Amitay, M., and Glezer, A., "Aerodynamic control using synthetic jets," AIAA Paper 2000-2401, June 2000.

Huang, L.S., Bryant, T.D., and Maestrello, L., "The effect of acoustic forcing on trailing edge separation and near wake development of an airfoil," AIAA 88-3531-CP, 1988.

Huang, L.S., Bryant, T.D., and Maestrello, L., "Separation control over an airfoil at high angles of attack by sound emanating from the surface," AIAA Paper 87-1261, 1987.

Jiang, K.C., Prewett, P.D., Ward, M.C.L., Tian, Y., and Yang, H., "Design of a micro Wankel rotary engine for MEMS fabrication," *Proceedings of SPIE – The International Society for Optical Engineering*, Vol. 4407, pp.54-60, 2001.

Korematsu, K., Saika, T., and Gabe, M., "A fundamental study of quenching distance measured by the flanged electrode method (selection of ignition energy and diameter of flanged disk)," *Bulletin of JSME*, Vol. 29, No. 253, pp.2167-2171, 1986.

Kral, L.D., Donovan, J.F., Cain, A.B., and Cary, A.W., "Numerical simulation of synthetic jet actuators," AIAA Paper 97-1824, June 1997.

Law, C.K., "A compilation of experimental data on laminar burning velocities," *Reduced Kinetic Mechanisms for Applications in Combustion Systems*, edited by N. Peters and B. Rogg, Springer-Verlag: New York, pp.15-26, 1993.

Lee, D.H., Choi, K.H., and Kwon, S., "Measurement and modeling of combustion in a microcombustor," AIAA Paper 2001-3077, June 2001.

Lee, D.H., Park, D.E., Yoon, J.B., Kwon, S., and Yoon, E., "Fabrication and test of a MEMS combustor and reciprocating device," *Journal of Micromechanics and Microengineering*, Vol.12, pp.26-34, 2002.

Lewis, B., and Von Elbe, G., *Combustion, Flames and Explosions of Gases*, 3<sup>rd</sup> Ed., Academic Press: Orlando, 1987.

Lin, R.-S., Hariharan, N., and Brogan, T., "Analysis of fluidic vortex valves for airflow control in combustors," AIAA Paper 2002-2946, June 2002.

McManus, K.R., Ducharme, A., Goldey, C., and Magill, J., "Pulsed jet actuators for suppressing flow separation," AIAA Paper 96-0442, January 1996.



- Mehra, A., Zhang, X., Ayon, A.A., Waitz, I.A., Schmidt, M.A., and Spadaccini, C.M., "A six-wafer combustion system for a silicon micro gas turbine engine," *Journal of Microelectromechanical Systems*, Vol. 9, No. 4, pp. 517-527, 2000.
- Mittal, R., Rampungoon, P., and Udaykumar, H.S., "Interaction of a synthetic jet with a flat plate boundary layer," AIAA Paper 2001-2773, June 2001.
- Muller, M.O., et al, "Thrust performance of micromachined synthetic jets," AIAA Paper 2000-2404, June 2000.
- Neuberger, D. and Wygnanski, I., "The use of a vibrating ribbon to delay separation on two dimensional airfoils," *Proceedings of Air Force Academy Workshop on Unsteady Separated Flow*, edited by F.J. Seiler, Research Labs. Rept. TR-88-0004, US Air Force Academy, 1987.
- Putnam, A.A., Belles, F.E., and Kentfield, J.A.C., "Pulse Combustion," *Progress in Energy and Combustion Science*, Vol. 12, pp. 43-79, 1986.
- Rediniotis, O.K., Ko, J., Yue, X., and Kurdila, A.J., "Synthetic jets, their reduced order modeling and applications to flow control," AIAA Paper 99-1000, January 1995.
- Rizzetta, D.P., Visbal, M.R., and Stanek, M.J., "Numerical investigation of synthetic-jet flowfields," *AIAA Journal*, Vol. 37, No. 8, pp. 919-927, 1999.
- Seifert, A., Bachar, T., Koss, D., Shepshelovich, M., and Wygnanski, I., "Oscillatory blowing: a tool to delay boundary-layer separation," *AIAA Journal*, Vol. 31, No. 11, pp. 2052-2060, 1993.
- Seifert, A., Darabi, A., and Wygnanski, I., "Delay of airfoil stall by periodic excitation," *Journal of Aircraft*, Vol. 33, No. 4, pp. 691-698, 1996.
- Sigurdson, L.W., and Roshko, A., "Controlled unsteady excitation of a reattaching flow," AIAA paper 85-00552, 1985.
- Smith, B.L. and Glezer, A., "The formation and evolution of synthetic jets," *Physics of Fluids*, Vol. 10, No. 9, pp. 2281-2297, 1998.
- Smith, B.L., *Synthetic Jets and Their Interactions with Adjacent Jets*, PhD Thesis, Georgia Institute of Technology, 1999.
- Smith, B.L., and Glezer, A., "Jet vectoring using synthetic jets," *Journal of Fluid Mechanics*, Vol. 458, pp.1-34, 2002.
- Smith, D.R., Amitay, M., Kibens, V., Parekh, D.E., and Glezer, A., "Modification of lifting body aerodynamics using synthetic jet actuators," AIAA Paper 98-2029, 1998.

Spearing, S.M., and Chen, K.S., "Micro-gas turbine engine materials and structures," *Ceramic Engineering and Science Proceedings*, Vol. 18, No. 4, pp. 11-18, 1997.

Swett, C.C. Jr., "Spark ignition of flowing gases II – effect of electrode parameters on energy required to ignite a propane-air mixture," National Advisory Committee for Aeronautics (NACA) Research Memorandum E51J12, 1951.

Tam, C.K.W., and Tanna, H.K., "Shock associated noise of supersonic jets from convergent-divergent nozzles," *Journal of Sound and Vibration*, Vol. 81, No. 3, pp. 337-358, 1982.

Turns, Stephen R., *An Introduction to Combustion: Concepts and Applications*, McGraw-Hill, Inc.: New York, 1996.

Ujiie, Y., "Spark ignition properties of combustible mixtures under high-turbulence-intensity conditions," *JSME International Journal*, Series B, Vol. 37, No. 3, pp. 611-617, 1994.

Waitz, I.A., Gauba, G., and Tzeng, Y.-S., "Combustors for micro-gas turbine engines," *Proceedings of the ASME Aerospace Division*, Vol. 52, pp. 777-788, 1996.

Wang, H., and Menon, S., "Fuel-air mixing enhancement by synthetic microjets," *AIAA Journal*, Vol. 39, No. 12, pp. 2308-2319, 2001.

Williams, D.R., Acharya, M., Bernhardt, J., and Yang, P.M., "The mechanism of flow control on a cylinder with the unsteady bleed technique," AIAA Paper 91-0039, 1991.

Willmes, G.F., and Burton, R.L., "Low-power helium pulsed arcjet," *Journal of Propulsion and Power*, Vol. 15, No. 3, pp. 440-446, 1999.